

**ADVANCING SUPER RESOLUTION MICROSCOPY FOR  
QUANTITATIVE IN-VIVO IMAGING OF CHROMATIN  
NANODOMAINS**

by

**Clayton Seitz**

**A Dissertation**

*Submitted to the Faculty of Purdue University*

*In Partial Fulfillment of the Requirements for the degree of*

**Doctor of Philosophy**



Department of Physics

Indianapolis, Indiana

December 2024

**THE PURDUE UNIVERSITY GRADUATE SCHOOL  
STATEMENT OF COMMITTEE APPROVAL**

**Dr. Gautam Vemuri, Chair**

Department of Physics

**Dr. Jing Liu**

Department of Physics

**Dr. Ruihua Cheng**

Department of Physics

**Dr. Stephen Wassall**

Department of Physics

**Dr. Horia Petrache**

Department of Physics

**Approved by:**

TBD

I dedicate this thesis to Alexandra, who has steadily encouraged my pursuit of a doctoral degree. I am forever indebted for your patience, understanding, and proofreading.

*What we observe is not nature itself, but nature exposed to our method of questioning*

Werner Heisenberg

*To deal with a 14-dimensional space, visualize a 3-dimensional space and say “fourteen” to yourself very loudly. Everyone does it*

Geoffrey Hinton

*Information is the resolution of uncertainty*

Claude Shannon

## TABLE OF CONTENTS

LIST OF TABLES . . . . .	7
LIST OF FIGURES . . . . .	8
LIST OF SYMBOLS . . . . .	11
ABSTRACT . . . . .	13
1 Single molecule localization microscopy . . . . .	14
1.1 Introduction . . . . .	14
1.1.1 Breaking the diffraction barrier . . . . .	14
1.1.2 Biological discovery with fluorescence nanoscopy . . . . .	16
1.2 The Image Likelihood . . . . .	17
1.2.1 Cramer-Rao lower bound . . . . .	19
1.2.2 Maximization of density, minimization of error . . . . .	20
2 Quantum enhanced localization with a single photon avalanche diode array . . . . .	23
2.1 Introduction . . . . .	23
2.1.1 A brief introduction to quantum optics . . . . .	23
2.1.2 Photon statistics . . . . .	24
2.2 Quantum enhanced localization microscopy . . . . .	25
2.2.1 Basic Scheme . . . . .	28
2.2.2 Results . . . . .	31
2.2.3 Discussion . . . . .	33
3 Uncertainty-aware localization microscopy by variational diffusion . . . . .	37
3.1 Introduction . . . . .	37
3.1.1 The curse of dimensionality . . . . .	37
3.1.2 The Bayesian calculation . . . . .	38
3.1.3 Variational inference . . . . .	39
3.1.4 A note on variational inference for functions . . . . .	40

3.1.5	Blending Bayesian inference with deep models for microscopy . . . . .	41
3.2	Results . . . . .	42
3.2.1	Approach . . . . .	42
3.2.2	Variational diffusion . . . . .	43
3.2.3	Experiments . . . . .	46
3.3	Conclusion . . . . .	48
3.4	Broader impact . . . . .	48
3.5	Appendix . . . . .	49
3.5.1	Sampling . . . . .	49
3.5.2	Derivation of the variational bound . . . . .	49
3.5.3	Neural network architectures . . . . .	51
4	Fluorescence nanoscopy in the study of chromatin organization . . . . .	54
4.1	Background on chromatin imaging . . . . .	54
4.1.1	Chromatin-associated-protein based labeling strategies . . . . .	55
4.1.2	Sequence specific labeling strategies . . . . .	55
4.1.3	Instrumentation for chromatin imaging . . . . .	56
4.2	The structure of chromatin nanodomains . . . . .	58
4.3	Polymer models and chromatin dynamics . . . . .	62
4.3.1	Trajectory linking . . . . .	63
4.3.2	Chromatin polymer models . . . . .	64
4.4	BRD4 regulates the structure of chromatin nanodomains . . . . .	68
4.4.1	Results . . . . .	70
	Colocalization of BRD4 mutants with nucleosome nanodomains . . .	70
	Chromatin structure and dynamics . . . . .	70
	Heteropolymer model . . . . .	71
4.4.2	Discussion . . . . .	75
4.4.3	Materials and Methods . . . . .	76
	Cell lines, cell culture conditions, and transfection . . . . .	76
	Super-resolution imaging of nucleosome nanodomains in living cells .	76

Colocalization of BRD4 mutants with nucleosome nanodomains . . . . .	77
Single molecule tracking . . . . .	77
Immunofluorescence . . . . .	77
Immunoblotting . . . . .	78
REFERENCES . . . . .	79

## LIST OF TABLES

4.1 Rouse polymer parameters . . . . .	65
4.2 Multivalent binder model parameters . . . . .	74

## LIST OF FIGURES

1.1	<b>Stochastic optical reconstruction microscopy (STORM).</b> (left) Single molecules are resolved by separating their fluorescent emission in time, using fluorophores with multiple photophysical states (right) Example super-resolution image of H2B protein in a living Hela cell nucleus at 37C, 5 percent CO <sub>2</sub> . Image reconstructed from 10 <sup>3</sup> 10ms frames. Scalebar 5um. . . . .	15
1.2	<b>Noise calibration for a CMOS camera used for maximum-likelihood localization.</b> (left)) CMOS offset for zero incident photons (middle) CMOS variance for zero incident photons (upper right) Cumulative mass function for the convolution distribution and its Poisson approximation for rate parameter $\mu_k = 500$ counts (lower right) Komogonov distance measured as a function of rate parameter $\mu_k$ . . . . .	18
1.3	<b>Resolution in nanoscopy depends on sampling density.</b> (left) Example kernel density estimate of H2B-HaloTag in a living HeLa cell nucleus (right) Fourier ring correlation (FRC) for different sampling ratios relative to an approximate total 400k localizations . . . . .	20
2.1	<b>Comparison of quantum dot images between CMOS and SPAD cameras.</b> (left) SPAD image of Qdot655 coated on a glass coverslip using a 100X/1.4NA oil-immersion objective (Nikon) and a 10ms exposure time. (right) CMOS image of Qdot655 using a 60X/1.4NA oil-immersion objective (Olympus) and a 10ms exposure time. Both use continuous-wave 640nm excitation . . . . .	25
2.2	<b>Experimental setup for widefield photon counting.</b> A 532nm pulsed laser is directed through a spatial filter, galvo mirror, and passed through filtering and focusing optics to a 100X oil-immersion objective. Emission light of a 50um grid is projected onto the SPAD512 camera (inset) . . . . .	26
2.3	<b>Single photon counting with a SPAD array</b> (a) Conventional widefield microscopy with integrated SPAD array (b) Single photon imaging scheme using 1us exposures containing a picosecond laser pulse (c) Sum of photon counts over a 5x5 region of interest (ROI), taken with $N_{\text{frames}} = 5 \times 10^5$ . . . . .	27
2.4	<b>Posteriors on the number of fluorescent emitters <math>N</math> and localization for <math>N^* = 1</math> (left) and <math>N^* = 2</math> (right) quantum dots.</b> Scalebars 360nm . . . . .	29
2.5	<b>Single and multi-emitter localization error on sums of photon counts.</b> (left) Localization uncertainty for simulated data for different values of $N$ , plotted with respect to the Cramer-Rao lower bound, shown in dashed gray. (right) Multi-emitter localization by MCMC sampling for $N = 3$ , colors indicate a cluster of samples i.e., a single localization. All data was generated with a background rate $\langle n_{\text{background}} \rangle = \lambda N_{\text{frames}} / d^2$ per pixel. Scalebar 360nm . . . . .	31
2.6	<b>Scaling of <math>g^{(2)}(0)</math> under zero background conditions.</b> (left) Scaling of $g^{(2)}(0)$ for small $N$ . (right) Scaling of $g^{(2)}(0)$ for large $N$ . . . . .	32

2.7	<b>Posterior distributions of the fluorophore number.</b> Samples from the Poisson-Binomial convolution distribution using $\zeta = 0.01$ for various values of $\lambda$ and $N = 1, 3, 5$ were simulated. The variable $\zeta$ was integrated out by Monte Carlo integration, sampling 1000 $\zeta$ values from the posterior distribution (see main text for details) . . . . .	35
2.8	<b>Posterior distributions of the fluorophore number.</b> Samples from the Poisson-Binomial convolution distribution using $\zeta = 0.01$ for various values of $\lambda$ and $N = 7, 9, 11$ were simulated. The variable $\zeta$ was integrated out by Monte Carlo integration, sampling 1000 $\zeta$ values from the posterior distribution (see main text for details) . . . . .	36
3.1	<b>Diffusion model with Markovian transitions and reversed arrows</b> . . . . .	44
3.2	<b>Super resolution by variational diffusion.</b> Example diffusion process of the latent high resolution image $\mathbf{y}$ conditioned on the low resolution image $\mathbf{x}$ . The terminal $\mathbf{y}_0$ represents a sample from $p(\mathbf{y} \mathbf{x})$ . . . . .	44
3.3	<b>Non cherry-picked estimation of marginal variances.</b> A low-resolution image $\mathbf{x}$ (left column) is transformed by $\phi$ to produce a KDE estimate $\hat{\mathbf{y}}$ (middle column) and a DDPM $\psi$ computes a map of marginal variances (right column) . . . . .	47
3.4	<b>Localization errors of the trained model <math>\phi</math>.</b> The Cramer-Rao lower bound is shown in red, computing by taking the diagonal elements of $I^{-1}(\theta)$ . . . . .	51
3.5	<b>Architecture of the augmentation model <math>\phi</math>.</b> A $20 \times 20$ single-channel movie is processed by eight convolutional blocks followed by a 4x upsampling module utilizing linear interpolation and a refinement module with six convolutional blocks. . . . .	52
3.6	<b>Architecture of the denoising diffusion model.</b> A U-Net style architecture with channel multipliers of [1,2,4,8,16] downsamples and then upsamples the input image $\mathbf{y}_t$ to estimate $\mathbf{y}_{t-1}$ . . . . .	53
4.1	<b>Photoswitching of JF646 bound to H2B-HaloTag.</b> (a) Peak intensity fluctuations of a putatively isolated JF646 molecule excited at 640nm and imaged with 10ms exposure time in the presence of 100mM MEA buffer. Fit of a Poisson HMM is shown in cyan (b) ON and OFF state lifetime distributions found by pooling data from 16 JF646 spots in a single HeLa cell nucleus. Single component exponential fits shown as solid lines. . . . .	59
4.2	<b>Besag's L-function under complete spatial randomness.</b> Point pattern simulations for complete spatial randomness ( $\sigma = 0$ ) for various intensities of the point process. Simulation envelopes are shown in pink, which represent the significance band of the estimated $L(r) - r$ . . . . .	60
4.3	<b>Besag's L-function for a Thomas process.</b> Point pattern simulations for the Thomas process ( $\sigma = 50\text{nm}$ ) for various intensities of the point process. Simulation envelopes are shown in pink, which represent the significance band of the estimated $L(r) - r$ . . . . .	61

4.4	<b>Snapshots of the Rouse polymer.</b> Four perspectives of the Rouse polymer generated with $N = 2000$ beads connected with harmonic bonds with equilibrium length 200nm. Polymer is initialized with all harmonic bonds at equilibrium . . . . .	65
4.5	<b>Subdiffusive dynamics of a Rouse polymer.</b> Mean squared displacement (MSD) of 2k beads shown in black, average MSD shown in red. . . . .	66
4.6	<b>Subdiffusive dynamics of the Rouse polymer.</b> (left) Histogram of the diffusion coefficient of individual beads. (right) Histogram of the anomalous exponent. Fitting of individual bead MSDs performed by linear regression in log-space using the first 5000 time points . . . . .	67
4.7	<b>Bromodomain protein 4 (BRD4) structure prediction.</b> (a) AlphaFold predicted structure of BRD4 long isoform (blue) with bromodomain 1 (BD1) aa58-163, bromodomain 2 (BD2) aa349-456, and N-terminus phosphorylation sites (NPS) aa462-506 highlighted in green. (b) Heat map of expected position error in AlphaFold prediction . . . . .	69
4.8	<b>BRD4 mutants colocalize with nucleosome nanodomains.</b> (a) Schematic of the BRD4 protein sequence and mutations shown in red. (b) Anti-FLAG western blot of bulk expression of BRD4 mutants. (c) Combined immunofluorescence of FLAG-tagged BRD4 mutants with JF646-tagged H2B-Halo. (d) Histograms of nearest neighbor distances of H2B puncta to FLAG puncta over $N=10$ cells for each mutant. Red dashed lines are drawn at the mean, statistical significance determined by Welch t-test for each mutant relative to wild-type (WT) * $p<0.05$ , *** $p<0.001$ . . . . .	71
4.9	<b>Strong multivalent chromatin binders reduce diffusion of nucleosome nanodomains.</b> (a) Heteropolymer model of chromatin consisting of A-type, B-type, and C-type particles. (b) Interaction potentials $U_{BC}(r_{ij})$ of multivalent chromatin binders with B-type chromatin beads. (c,d) Example free heteropolymer and heteropolymer with a number density of C-type particles of $\rho = 500/\mu\text{m}^3$ in a 10um periodic box. (e) Scaled diffusion coefficient $D$ for various chromatin binding energies of C-type particles, averaged over ten independent simulations, with burn-in discarded. . . . .	72
4.10	<b>Expression of constitutively phosphorylated BRD4 compacts nucleosome nanodomains.</b> (a,b) Direct stochastic optical reconstruction microscopy (dSTORM) imaging strategy of single nucleosomes and an examples super-resolution image. (c) Two-color image of super-resolved H2B-JF646 with diffraction-limited GFP-tagged BRD4. (d) Besags L-function for various BRD4 mutants. All scale-bars 3um. . . . .	73
4.11	<b>BRD4 mutants reduce single nucleosome dynamics in living cells.</b> (a,b) Sparse labeling of single nucleosomes in a living Hela cell (scalebar 5um). (c) Average mean squared displacement (MSD) of single nucleosomes for wild-type and mutated BRD4, error bars represent the standard error of the mean. (d) Kernel density estimates of the MSD distribution at representative lag times. . . . .	74

## LIST OF SYMBOLS

$\mathbf{x}$	An image at base resolution
$\mathbf{y}$	An image at higher resolution
$\delta$	Pixel lateral width
$k$	Pixel index
$\theta$	A parameter
$u, v$	Cartesian coordinates in two-dimensions
$g_k$	Pixel-wise gain
$o_k$	Pixel-wise offset
$w_k$	Pixel-wise readout noise standard deviation
$\mu_k$	Pixel-wise expected value
$s_k$	Pixel-wise measured signal
$\xi_k$	Pixel-wise measured readout noise
$O$	Point spread function
$\text{erf}$	Error function
$\sigma_{\mathbf{x}}$	Gaussian PSF width
$\sigma_{\mathbf{y}}$	Kernel width for kernel density estimate
$\epsilon$	An image of pure Gaussian noise
$\beta$	Diffusion model noise variance
SNR	Diffusion model signal to noise ratio
$\psi$	Diffusion model parameters
$\phi$	Augmentation network parameters
$\mathcal{L}$	An objective function
$D_{KL}$	KL-divergence
$p$	A discrete or continuous probability distribution
$\mathbb{E}_p$	Expectation with respect to a distribution $p$
$I$	Fisher information matrix
$\lambda$	Expected number of background counts per frame
$d$	Lateral dimension of a region of interest

$\zeta$	Photon detection probability
$\tau$	Delay time
$g^{(2)}(\tau)$	Second order coherence function
$B$	Expected number of signal-background coincidences per frame
$G^{(2)}(m)$	Measured number of signal-signal coincidences at lag time $m$
$N_{\text{frames}}$	Number of frames
$N$	Number of active fluorescent emitters
$N^*$	Maximum a posteriori estimate of number of active emitters
$n$	Number of photon counts in a frame
$\ell$	Log-likelihood
$\hat{a}$	Ladder operator
$\hat{E}$	Electric field operator
$\rho$	Density matrix or number density for molecular dynamics
$L(r)$	Besag's L-function
$K(r)$	Ripley's K-function
$G(r)$	Nearest neighbor distribution function
$\lambda$	(Point Pattern Analysis) Intensity of a point process
$\gamma$	Friction tensor
$\xi$	A delta-correlated Gaussian noise
$k_B$	Boltzmann's constant
$T$	Temperature
$U$	Potential energy
$D$	Diffusion coefficient
$\epsilon$	(Molecular Dynamics) Energy
$r_0$	Harmonic bond equilibrium length
$R_0$	Binder potential equilibrium length
$\alpha$	Anomalous diffusion exponent

## ABSTRACT

Single molecule localization microscopy (SMLM) techniques, such as direct stochastic optical reconstruction microscopy (dSTORM), can be used to produce a pointillist representation of fluorescently-labeled biological structures at diffraction-unlimited precision. This class of techniques permits localization of fluorescent molecules in the cell with nanometer precision and thus is commonly referred to as *nanoscopy*. Conventional nanoscopy approaches leverage the deactivation of standard fluorescent tags, followed by spontaneous or photoinduced reactivation, to resolve fluorophores at distances below the diffraction limit. While powerful, this approach has limited throughput and requires localization in sparse scences. This dissertation introduces fluorescence nanoscopy and covers its innovation and application as discussed in the following papers:

*Quantum enhanced localization microscopy with a single photon avalanche diode array* [1] leverages recent advancements in single photon avalanche diode array technology to count fluorescent emitters, enabling rigorous multi-emitter fitting in fluorescence microscopy.

*Uncertainty-aware localization microscopy by variational diffusion* [2] describes a novel algorithm that leverages a diffusion model in order to model a posterior distribution on high resolution localization microscopy images, given low resolution inputs.

*BRD4 phosphorylation regulates structure of chromatin nanodomains* [3] describes the role of the BRD4 phosphoswitch in the maintenance of chromatin nanodomains via super resolution microscopy and molecular dynamics simulation. We build on the notion that chromatin binding activity of BRD4 is regulated by phosphorylation through demonstration that BRD4 phosphorylation regulates chromatin packing and mobility in mammalian nuclei.

## 1. Single molecule localization microscopy

### 1.1 Introduction

#### 1.1.1 Breaking the diffraction barrier

In the quest to understand cellular function, biologists aim to directly observe the processes enabling cells to maintain homeostasis and respond dynamically to internal and environmental cues at the molecular level. However, the inherent limitations imposed by diffraction have historically constrained the resolution achievable with conventional light microscopy. The diffraction limit, first described by Ernst Abbe in the 19th century, dictates that the resolution of a microscope is fundamentally limited by the wavelength of light used for imaging. Objects closer than approximately half the wavelength of light cannot be distinguished as separate entities. For visible light, this translates to a resolution limit of about 200-250 nanometers, which is insufficient for resolving many subcellular structures and molecular complexes.

Super-resolution (SR) microscopy techniques have emerged as a pathway to observing subcellular structures and dynamics with enhanced resolution, surpassing the classical Abbe diffraction limit. Fluorescence microscopy techniques continually push the resolution boundary towards nanometer scales, facilitating imaging of cellular structures with a level of detail previously achievable only with electron microscopy. Concurrently, SR techniques retain optical microscopy advantages in biological experiments, including sample preservation, imaging flexibility, and target specificity. SR enables extraction of quantitative information on spatial distributions and often absolute numbers of proteins, nucleic acids, or other macromolecules within subcellular compartments.

A host of SR methods have been developed in recent years, which fundamentally differ in how fluorescently labeled samples are excited and how the emitted photons are detected. Here, I focus on a particular technique referred to as single-molecule localization microscopy or nanoscopy. This class of diffraction-unlimited SR methods leverage fluorescence intermittency to resolve fluorophores which would otherwise be unresolvable at the detector (Figure 1.1). Nanoscopy approaches, such as direct-STORM (dSTORM), have become quite popular because they can be implemented at low cost on conventional, camera-based, wide-field

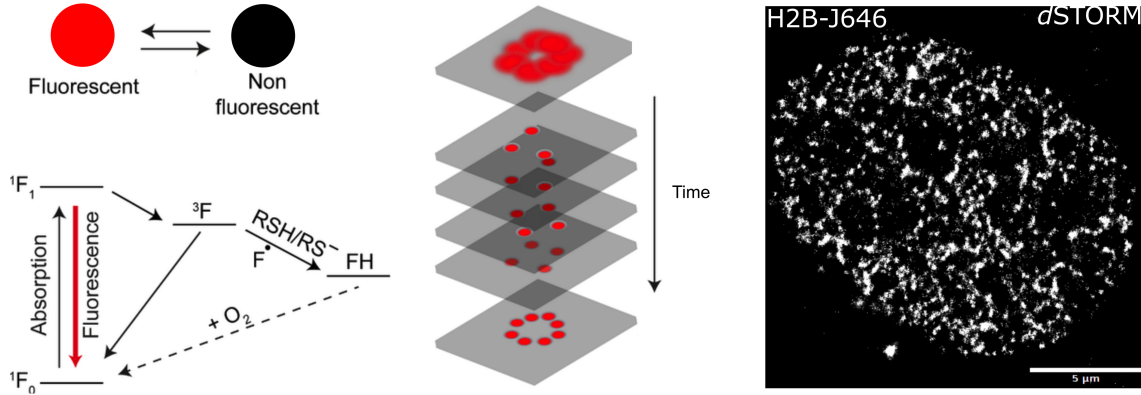


**Figure 1.1. Stochastic optical reconstruction microscopy (STORM).** (left) Single molecules are resolved by separating their fluorescent emission in time, using fluorophores with multiple photophysical states (right) Example super-resolution image of H2B protein in a living Hela cell nucleus at 37C, 5 percent CO<sub>2</sub>. Image reconstructed from 10<sup>3</sup> 10ms frames. Scalebar 5um.

setups, shifting the complexity to biological sample preparation and image post processing. Common strategies for the temporal separation of molecules involve transient intramolecular rearrangements to switch from dark to fluorescent states or the exploitation of non-emitting molecular radicals. For example, in dSTORM, rhodamine derivatives can undergo intersystem crossing to a triplet state, which can be reduced by thiols to form a dark radical species. The dark state can then be quenched by oxidative processes, driving the fluorophore back to its ground state.

In nanoscopy applications, we seek the position and intensity of isolated fluorophores as well as to estimate the accuracy and precision of these parameters. Accuracy is a measure of the systematic error or bias, and precision is a measure of the statistical error of an estimator. Both of these metrics are crucial in nanoscopy, as they determine the maximum achievable resolution of the method. Importantly, a super resolution image in nanoscopy is simply a kernel density estimate (KDE) of the located fluorescent emitters, using an isotropic Gaussian kernel. The width of one such placed Gaussian kernel,  $\sigma$  is given by the precision of the fluorophore position localization. The value of  $\sigma$  will depend on the various experimental

factors such as signal to noise ratio (SNR) or the on and off state lifetimes of the blinking fluorophore.

### 1.1.2 Biological discovery with fluorescence nanoscopy

Using fluorescence nanoscopy, scientists can now explore the nanoscale organization of cells and their components, leading to groundbreaking discoveries and new insights into cellular processes. In immunology, nanoscopy has been employed to study the spatiotemporal dynamics of T cell antigen receptor (TCR) complexes and linker for activation of T cells (Lat), an important adaptor molecule in the TCR signaling pathway [5]. Others used nanoscopy to demonstrate that clustering patterns of the tyrosine kinase Lck were controlled by the conformational states of Lck, with the open, active conformation inducing clustering and the closed, inactive conformation preventing clustering [6]. Nanoscopy has also proven invaluable in virology. In this field, researchers have utilized nanoscopy techniques to visualize Human immunodeficiency virus type 1 (HIV-1) assembly and budding at the plasma membrane of living host CD4+ T cells by tracking the viral membrane Gag proteins and its derivatives from the host cell plasma membrane [7]. This has led to a deeper understanding of the molecular mechanisms underlying viral infections and has provided insights into the structure of viral capsids and replication mechanisms.

The ability to study cellular structures at the nanoscale has also advanced our understanding of molecular machines and complexes within cells. For instance, detailed imaging of the nuclear pore complex, a crucial structure for nucleocytoplasmic transport, has revealed the precise arrangement of its constituent proteins [8]. This has enhanced our knowledge of how the nuclear pore complex regulates the passage of molecules between the nucleus and cytoplasm, a process essential for cellular function. In epigenetics, nanoscopy has facilitated the investigation of fundamental nature of chromatin structure at the nanoscale [9]. The effects of histone modifications or the assembly of transcriptional complexes can also be directly visualized and quantitatively measured with spatial resolution [9]–[11].

As nanoscopy continues to evolve, future advancements are likely to enhance both the resolution and speed of imaging, allowing researchers to capture dynamic processes within

living cells in real time. New techniques and improvements in instrumentation will expand the capabilities of nanoscopy, enabling even more detailed studies of cellular functions and interactions. Towards this aim, I will now derive a fundamental statistical description of fluorophore detection in nanoscopy. This description is necessarily simplified - background rates of light detection may vary across the field of view, and the fluorophore emission rate of chemically identical fluorophores can vary owing to effects such as uneven illumination profile, dipole orientation or different optical path lengths.

## 1.2 The Image Likelihood

It is common to describe the optical impulse response of a microscope as a two-dimensional isotropic Gaussian [12]. This is an approximation to the more rigorous diffraction models given by [13], [14]. Over a continuous domain, the impulse response reads

$$O(u, v) = \frac{1}{2\pi\sigma^2} e^{-\frac{(u-\theta_u)^2+(v-\theta_v)^2}{2\sigma^2}}$$

The above expression can be loosely interpreted as a probability distribution over locations where a photon can be detected. For discrete detectors, such as a camera, we bin this expression by integrating over pixels. The number of photon arrivals will follow Poisson statistics [15], [17], with expected value

$$\mu_k = i_0 \left( \int_{u_k-\delta/2}^{u_k+\delta/2} O(u; \theta_u) du \right) \left( \int_{v_k-\delta/2}^{v_k+\delta/2} O(v; \theta_v) dv \right)$$

The scalar quantity  $i_0$  represents the amplitude of the signal, which is proportional the quantum efficiency of a pixel  $\eta$ , the duration of exposure,  $\Delta$ , and the number of photons emitter by a fluorescent molecule  $N_0$ . With no loss of generality,  $\Delta = \eta = 1$  and there is a single free parameter  $N_0$ . Terms above in parentheses are simply integrals of Gaussian functions and can be evaluated analytically. I define them as  $\Gamma_u, \Gamma_v$ , respectively. For example,

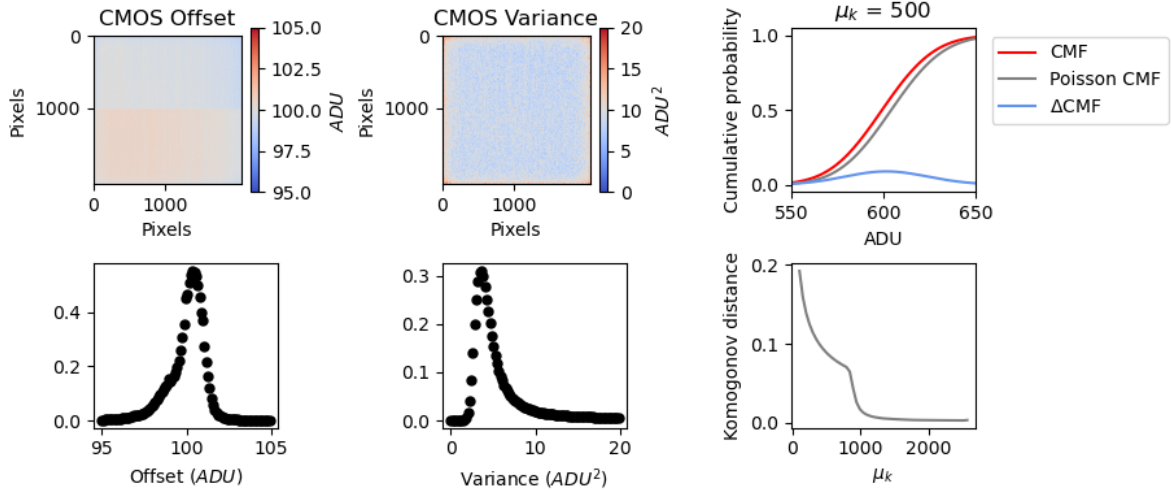


**Figure 1.2. Noise calibration for a CMOS camera used for maximum-likelihood localization.** (left)) CMOS offset for zero incident photons (middle) CMOS variance for zero incident photons (upper right) Cumulative mass function for the convolution distribution and its Poisson approximation for rate parameter  $\mu_k = 500$  counts (lower right) Komogonov distance measured as a function of rate parameter  $\mu_k$

$$\begin{aligned}\Gamma_u &:= \int_0^{u_k + \delta/2 - \theta_u} O(u) du - \int_0^{u_k - \delta/2 - \theta_u} O(u) du \\ &= \frac{1}{2} \left( \operatorname{erf} \left( \frac{u_k + \frac{\delta}{2} - \theta_u}{\sqrt{2}\sigma_x} \right) - \operatorname{erf} \left( \frac{u_k - \frac{\delta}{2} - \theta_u}{\sqrt{2}\sigma_x} \right) \right)\end{aligned}$$

where we have used the common definition  $\operatorname{erf}(z) = \frac{2}{\sqrt{\pi}} \int_0^z e^{-t^2} dt$ . Recall the central objective of localization microscopy is to infer a set of molecular coordinates  $\theta = (\theta_u, \theta_v)$  from measured low resolution images  $\mathbf{x}$ . In general, the likelihood on a particular pixel  $p(\mathbf{x}_k | \theta)$  is taken to be a convolution of Poisson and Gaussian distributions, due to shot noise  $p(s_k) = \text{Poisson}(\mu_k)$  and sensor readout noise  $p(\xi_k) = \mathcal{N}(o_k, w_k^2)$ . Characterization of the readout noise characteristics  $o_k, w_k$  of the imaging sensor is a critical step in parameterizing localization algorithms used in nanoscopy (Figure 1.2). Then one defines the likelihood as a convolution distribution:

$$p(\mathbf{x}_k|\theta) = A \sum_{q=0}^{\infty} \frac{1}{q!} e^{-\mu_k} \mu_k^q \frac{1}{\sqrt{2\pi w_k}} e^{-\frac{(\mathbf{x}_k - g_k q - o_k)^2}{2w_k^2}} \approx \text{Poisson}(\mu'_k) \quad (1.1)$$

where  $A$  is some normalization constant. For the sake of generality, we include a per-pixel gain factor  $g_k$ [ADU/photon], which is often unity. Sampling from  $p(\mathbf{x}_k|\theta)$  is trivial; however, for computation of a lower bound on uncertainty in  $\theta$ , the summation in (1.1) can be difficult to work with. Therefore, we choose to use a Poisson approximation for simplification, valid under a range of experimental conditions [15]. The quality of this approximation will depend on the signal level, with higher signal levels or higher exposure times leading to a reduced Komogorov distance between the convolution distribution and a Poisson approximation (Figure 1.2). After subtraction of the offset  $o_k$  of the pixel array, we have  $\mu'_k = \mu_k + w_k^2$ .

Under the Poisson approximation in the likelihood, the model negative log-likelihood is

$$\ell(\mathbf{x}|\theta) = -\log \prod_k \frac{e^{-(\mu'_k)} (\mu'_k)^{n_k}}{n_k!} = \sum_k \log n_k! + \mu'_k - n_k \log(\mu'_k) \quad (1.2)$$

where  $n_k$  is the number of arbitrary digital units (ADU) measured. Localization then proceeds by optimization of  $\ell(\mathbf{x}|\theta)$  to obtain the maximum likelihood estimate (MLE) of the coordinates.

### 1.2.1 Cramer-Rao lower bound

Reliable inference of  $\theta$  from  $\mathbf{x}$  in general requires performance metrics for model selection. Here, I use the Fisher information as an information theoretic criteria to assess the discrepancy between theoretical minimum precision with respect to the root mean squared error (RMSE) of our predictions of  $\theta$  i.e., localization uncertainty [16]. The Poisson log-likelihood  $\ell(\mathbf{x}|\theta)$  is convenient for computing the Fisher information matrix [17] and thus the Cramer-Rao lower bound, which bounds the variance of a statistical estimator of  $\theta$ , from below:  $\text{var}(\hat{\theta}) \geq I^{-1}(\theta)$ . The Fisher information is given by the expression

$$I_{ij}(\theta) = \mathbb{E}_{\theta} \left( \frac{\partial \ell}{\partial \theta_i} \frac{\partial \ell}{\partial \theta_j} \right) \quad (1.3)$$

For an arbitrary parameter, we find that, for a Poisson log-likelihood  $\ell$

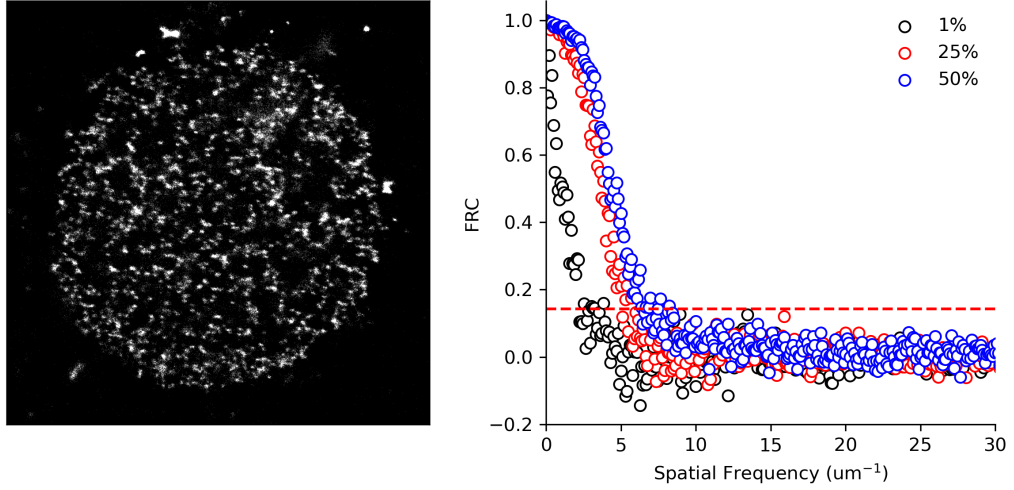


**Figure 1.3. Resolution in nanoscopy depends on sampling density.** (left) Example kernel density estimate of H2B-HaloTag in a living HeLa cell nucleus (right) Fourier ring correlation (FRC) for different sampling ratios relative to an approximate total 400k localizations

$$\begin{aligned}\frac{\partial \ell}{\partial \theta_i} &= \frac{\partial}{\partial \theta_i} \sum_k \log n_k! + \omega'_k - n_k \log(\omega'_k) \\ &= \sum_k \frac{\partial \omega'_k}{\partial \theta_i} \left( \frac{\omega'_k - n_k}{\omega'_k} \right)\end{aligned}$$

Using this result, we can compute the Fisher information matrix  $I(\theta)$

$$I_{ij}(\theta) = \mathbb{E}_{\theta} \left( \sum_k \frac{\partial \omega'_k}{\partial \theta_i} \frac{\partial \omega'_k}{\partial \theta_j} \left( \frac{\omega'_k - n_k}{\omega'_k} \right)^2 \right) = \sum_k \frac{1}{\omega'_k} \frac{\partial \omega'_k}{\partial \theta_i} \frac{\partial \omega'_k}{\partial \theta_j}$$

A fundamental lower bound on the localization uncertainty in our estimates of  $\theta$  then is found from its inverse:  $\text{CRLB} = I^{-1}(\theta)$ .

### 1.2.2 Maximization of density, minimization of error

The distribution of a particular biomolecule in the cell can be described as a probability density over a two-dimensional space, casting super-resolution as a density estimation

problem. Intuitively, the spatial resolution of SMLM images then increases as we draw more samples from this density - a concept which is made mathematically precise by the so-called Fourier ring correlation (FRC) [18]. Using FRC, one can define image resolution as the spatial frequency at which a correlation function in the frequency domain drops below a threshold, typically taken to be 1/7 (Figure 1.3). This correlation function is defined as the following correlation function for two concentric rings in the frequency domain:

$$\text{FRC}(q) := \frac{\sum_{\vec{q} \in \text{circle}} \tilde{f}_1(\vec{q}) \tilde{f}_2(\vec{q})^*}{\sqrt{\sum_{\vec{q} \in \text{circle}} |f_1(\vec{q})|^2} \sqrt{\sum_{\vec{q} \in \text{circle}} |f_2(\vec{q})|^2}}$$

According to this theory, reducing localization uncertainty while increasing the number of samples, results in an increase in image resolution. However, typical nanoscopies favor fewer samples and lower localization uncertainty as few tools to deal with localization in dense scenes are available. Indeed, localization uncertainties in sparse conditions are often tens of nanometers; however managing the increase in localization uncertainty at high labeling density remains a major bottleneck to localization microscopy. Static uncertainty due to molecular crowding can be partially ameliorated by using pairwise or higher-order temporal correlations within a pixel neighborhood, known as stochastic optical fluctuation imaging or SOFI [19]. Other approaches such as stimulated emission and depletion (STED) imaging bring control over the photophysical state of a chosen subset of the sample, yet the need for laser scanning prevents widespread application in live-cell studies. The spatial resolution and relative simplicity of SMLM techniques remains unmatched, inciting an effort to increase the resolution of SMLM techniques and explore avenues towards time resolved localization microscopy.

In the next two chapters, I approach localization in dense scenes as an inference problem in a high dimensional parameter space. In Chapter 2, I design a generative modeling framework for kernel density estimation in localization microscopy, using variational diffusion. This approach not only accelerates super-resolution imaging but also provides a way to estimate uncertainty in the results. In Chapter 3, I leverage single photon avalanche diode (SPAD) arrays to accurately count active fluorescent emitters while performing multi-emitter localization. SPAD cameras, with their high temporal resolution and single photon sensi-

tivity, enable precise localization in non-sparse scenes. These two methods, one focusing on sophisticated computational models and the other on cutting-edge hardware, offer complementary solutions to the high-dimensional inference problem in super-resolution microscopy. Using them separately or in tandem, we can achieve more accurate and reliable imaging of biological structures at the nanoscale. Finally, in Chapter 4, I apply a more conventional form of localization microscopy to the study of chromatin organization in living mammalian cells.

## 2. Quantum enhanced localization with a single photon avalanche diode array

### 2.1 Introduction

#### 2.1.1 A brief introduction to quantum optics

Experimental techniques have surfaced which take advantage of the quantum nature of light to enhance imaging methods. The advent of very fast and sensitive detectors allows us to measure electromagnetic fields at a timescale where quantum effects can be seen. We often speak of methods such as photon counting or photon statistics, and it is prudent to briefly define the photon and how it be measured with this technology.

Field quantization generally begins by writing a Fourier expansion of solutions to Maxwell's equations and identifying the canonical position and momentum variables. This procedure is out of the scope of this thesis. Instead, I start by stating the major result of quantization, in which each *mode* of the field is quantized as a quantum harmonic oscillator. As such, the Hamiltonian for one particular mode has energy eigenvalues  $E_k = \hbar\omega_k(\hat{n} + \frac{1}{2})$  for mode  $k$  with frequency  $\omega_k$ . The operator  $\hat{n} = \hat{a}^\dagger\hat{a}$  is the number operator such that  $\hat{n}|\psi\rangle = n|\psi\rangle$  where  $n$  is the number of energy quanta. The value of the eigenvalue  $n$  represents the number of energy quanta present in the field, each quanta being called a photon. Since there are potentially infinitely many modes, the wavefunction is  $|\psi\rangle = |n_1, n_2, \dots\rangle$  where  $n_1$  is the number of photons in the first mode,  $n_2$  is the number of photons in the second mode, and so on. The number operator for the  $k$ -th mode gives  $\hat{n}_k|\psi\rangle = n_k|\psi\rangle$ .

We also define  $\hat{a}_k$  and  $\hat{a}_k^\dagger$  as the respective annihilation and creation operators for the  $k$ -th mode. These operators satisfy the commutation relations  $[\hat{a}_k, \hat{a}_{k'}^\dagger] = \delta_{kk'}$  and  $[\hat{a}_k, \hat{a}_{k'}] = [\hat{a}_k^\dagger, \hat{a}_k^\dagger] = 0$ . The action of the annihilation and creation operators on the joint number states is:

$$\hat{a}_k|n_1, n_2, \dots\rangle = n_k|n_1, n_2, \dots\rangle \quad \hat{a}_k^\dagger|n_1, n_2, \dots\rangle = (n+1)|n_1, n_2, \dots\rangle$$

### 2.1.2 Photon statistics

Using this formalism, we can define any  $|\psi\rangle$  that we like in this framework. However, there are certain interesting states which have special properties, such as the coherent state. Coherent states are a special class of states that resemble classical oscillations of the EM field. A coherent state  $|\alpha\rangle$  is defined as the eigenstate of the annihilation operator  $\hat{a}$ :

$$\hat{a} |\alpha\rangle = \alpha |\alpha\rangle$$

where  $\alpha$  is a complex number. The coherent state for a single mode field are given by:

$$|\alpha\rangle = e^{-\frac{|\alpha|^2}{2}} \sum_{m=0}^{\infty} \frac{\alpha^m}{m!} |m\rangle$$

It turns out that if we measure a number of photons in this state, we would find that the number of photons has Poisson statistics. To see this, we calculate the probability  $p(m)$  of finding  $m$  photons in a coherent state  $|\alpha\rangle$ :

$$P(m) = |\langle m| |\alpha\rangle|^2 = |e^{-\frac{|\alpha|^2}{2}} \frac{\alpha^m}{m!}|^2 = e^{-|\alpha|^2} \frac{|\alpha|^{2m}}{m!}$$

This is simply the Poisson distribution with mean  $\langle \hat{n} \rangle = |\alpha|^2$ . The variance of the photon number distribution in a coherent state is also  $|\alpha|^2$ , characteristic of Poisson statistics, where the mean and variance are equal.

In contrast, single photon states e.g.,  $|1\rangle$  do not necessarily follow Poisson statistics. This state could be prepared by an isolated single photon source such as a fluorescent dye molecule, quantum dot, or nitrogen vacancy, which can produce only a single photon at a time. This phenomenon is referred to as *fluorescence antibunching* where photons tend to be detected as isolated events rather than in bursts or bunches. Note that for such a single photon source the single-mode field can be in state  $|1\rangle$  but not state  $|2\rangle$  at any given time. If more single photon sources are present or multi-level relaxations occur, states beyond  $|1\rangle$  are possible. This has led to the introduction of binomial states of the quantized field [20]. This fact is leveraged in the following sections, to count the number of single photon sources in a region of interest using a widefield photon counting camera.

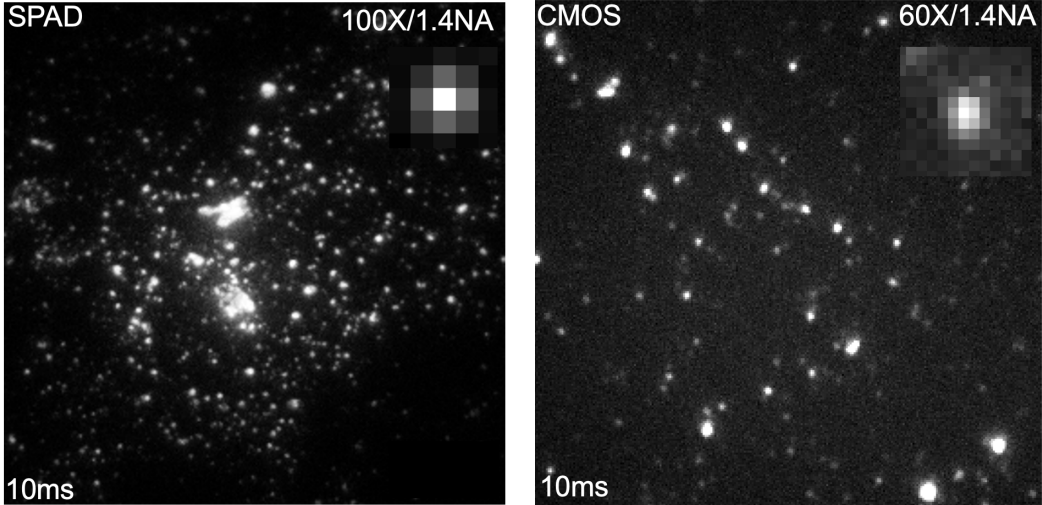


**Figure 2.1. Comparison of quantum dot images between CMOS and SPAD cameras.** (left) SPAD image of Qdot655 coated on a glass coverslip using a 100X/1.4NA oil-immersion objective (Nikon) and a 10ms exposure time. (right) CMOS image of Qdot655 using a 60X/1.4NA oil-immersion objective (Olympus) and a 10ms exposure time. Both use continuous-wave 640nm excitation

## 2.2 Quantum enhanced localization microscopy

Far-field optical microscopy is fundamentally limited by diffraction, with the maximum attainable resolution being limited to approximately half the wavelength of light. Several schemes to beat the diffraction limit have been developed in recent years. Many of these schemes utilize the concept of precise localization of isolated fluorescent emitters which blink over a time series of frames [21], [22]. An inherent problem with such methods is the requirement that fluorescent emitters be isolated, slowing down the acquisition of super-resolved images. To address this, we leverage the fact that many fluorophores are intrinsically single photon sources and exhibit fluorescence antibunching. This property can constrain the number of active fluorescent emitters in a region of interest (ROI) and can potentially enable localization in non-sparse scenes [23], [24].

Molecular counting with fluorescence antibunching has a fairly simple motivation: coincidence of photons at multiple detector elements during high speed imaging provides evidence

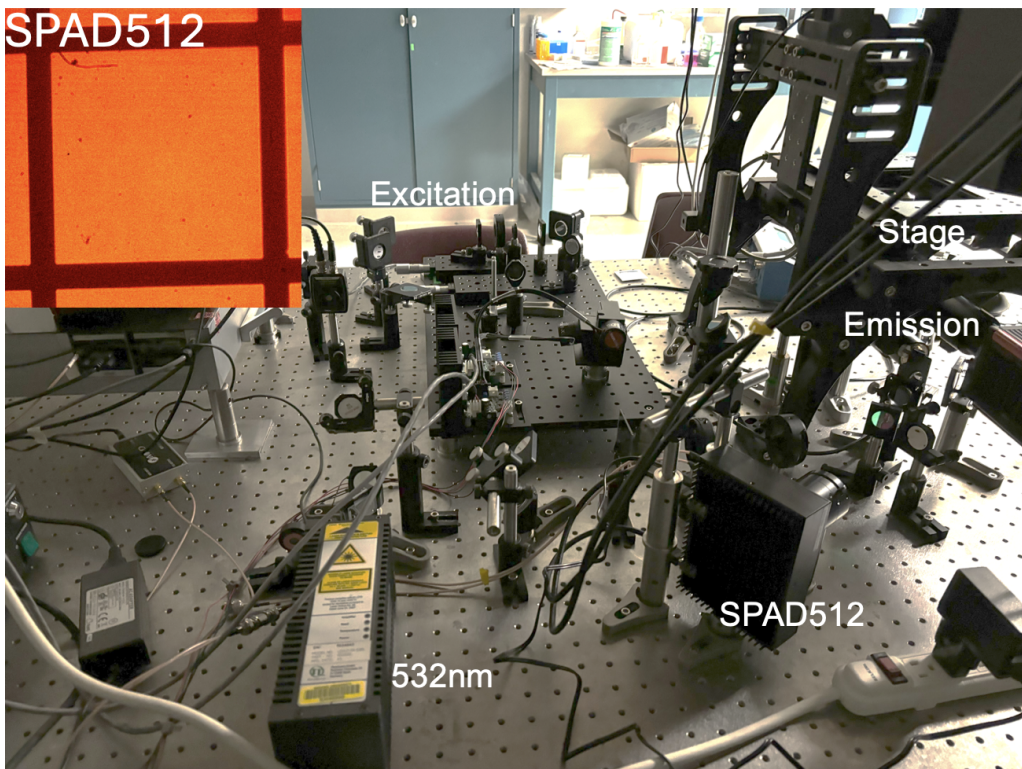


**Figure 2.2. Experimental setup for widefield photon counting.** A 532nm pulsed laser is directed through a spatial filter, galvo mirror, and passed through filtering and focusing optics to a 100X oil-immersion objective. Emission light of a 50um grid is projected onto the SPAD512 camera (inset)

for the number of single photon sources present in the imaged region. Combining the ideas of conventional super-resolution approaches with photon statistics may prove to be a powerful set of methods for bioimaging. SPAD cameras achieve orders of magnitude higher temporal resolutions than standard CMOS cameras, single photon sensitivity, and dark count rates less than 25cps (Figure 2.1). Furthermore, the reduced readout noise and large fill-factor of recently commercialized SPAD arrays suggests their use for single molecule localization with reduced localization uncertainty.

In this study, we present a method for widefield single photon counting in order to rigorously count fluorophores in the sample and subsequently constrain single molecule localization. We investigate the theoretical properties of the zero-lag second-order coherence

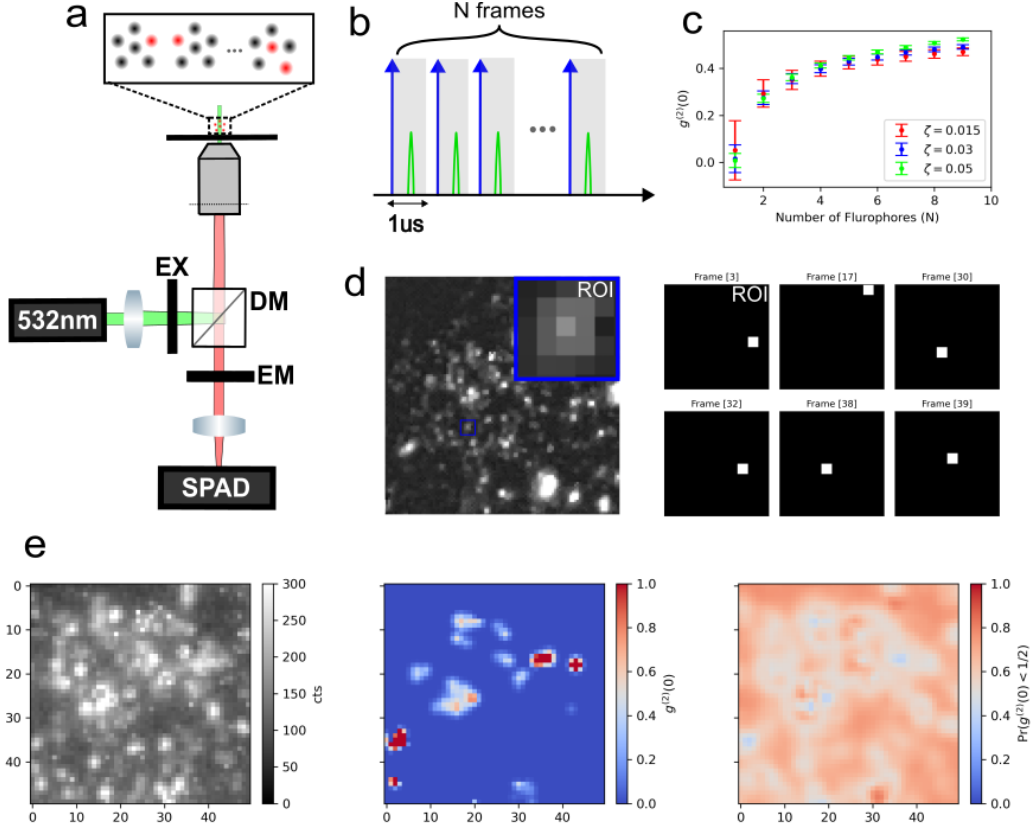


**Figure 2.3. Single photon counting with a SPAD array** (a) Conventional widefield microscopy with integrated SPAD array (b) Single photon imaging scheme using 1us exposures containing a picosecond laser pulse (c) Sum of photon counts over a 5x5 region of interest (ROI), taken with  $N_{\text{frames}} = 5 \times 10^5$

function  $g^{(2)}(0)$  for widefield photon counting and its spatial properties (Figure 2.3). Using Bayesian analysis, we derive a posterior distribution on the number of active fluorescent emitters in a region of interest. We then combined this with single molecule localization algorithms and demonstrate resolution of multiple emitters using a multi-emitter fitting algorithm and report localization errors with respect to the Cramer-Rao bound.

### 2.2.1 Basic Scheme

We consider a simplified description of widefield photon counting for a single photon source in the object plane labeled by a continuous-valued coordinate  $\theta = (\theta_u, \theta_v)$ . The spatial profile  $O$  of the field in image space is again presumed to have a Gaussian shape [12]–[14].

$$O(u, v) = \frac{1}{2\pi\sigma^2} e^{-\frac{(u-\theta_u)^2+(v-\theta_v)^2}{2\sigma^2}} \quad (2.1)$$

A similar theoretical exposition follows to Section 1.2; however, slight modifications are made to the theory to relate it to the quantum theory. Since our SPAD detectors at the image plane must also be discrete, the total field at a detector element  $k$  centered in image space at  $s_k = (u_k, v_k)$  is then given by integrating over pixels of width  $\delta = 1$ . Using the definitions of  $\Gamma_x, \Gamma_y$  from Section 1.2, we define

$$\zeta_k := \langle n_k \rangle = \Gamma_x(u_k, \theta_u)\Gamma_y(v_k, \theta_v)\zeta \quad (2.2)$$

where  $\langle n_k \rangle$  is the expected number of photons detected at pixel  $k$ . We now consider the case of pulsed excitation where the interval between pulses much longer than the fluorescence lifetime. Upon excitation of an isolated fluorescent emitter, a photon is detected at a particular detector element  $k$  with probability  $\zeta_k$ . Similarly, the probability of detection in a region of interest collecting all photons emitted is  $\zeta$ . Here, we are primarily concerned with the latter quantity, and its application in counting fluorescent emitters.

By temporarily ignoring the spatial profile described by (1), we derive a likelihood on the number of fluorophores in a small ROI with a lateral dimension  $d = 5$  pixels. For  $N$  fluorophores emitting photons which can be detected within a ROI of the SPAD array, the number of signal photons measured  $n_{\text{signal}}$  following a single excitation pulse will have Binomial statistics  $n_{\text{signal}} \sim \text{Binom}(N, \zeta)$ . Photon pile-up at a single detector element can be safely neglected in this model due to its relatively low likelihood. We then model the background signal within the region of interest as a coherent state, which we have shown followd Poissonian statistics  $n_{\text{background}} \sim \text{Poisson}(\lambda)$  for an expected number  $\lambda$  of background

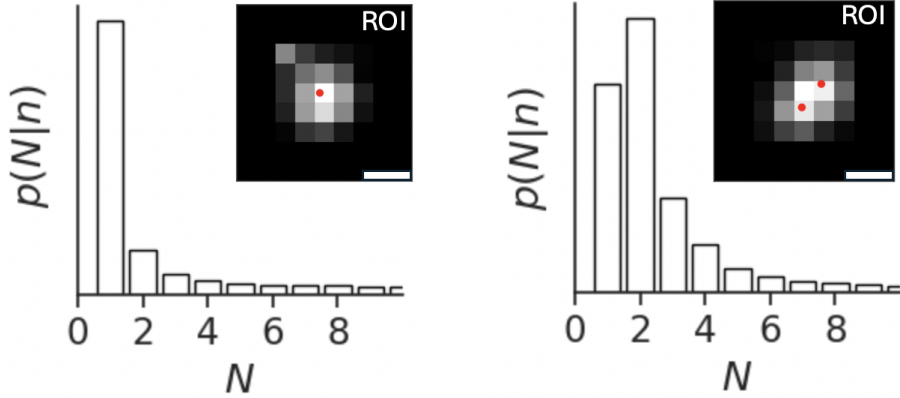


**Figure 2.4.** Posteriors on the number of fluorescent emitters  $N$  and localization for  $N^* = 1$  (left) and  $N^* = 2$  (right) quantum dots. Scalebars 360nm

counts in the ROI per frame. The total number of counts  $n = n_{\text{signal}} + n_{\text{background}}$  detected in the region of interest following a single pulse is then distributed by the likelihood

$$p(m | N, \zeta, \lambda) = \sum_{i=0}^{\infty} \binom{N}{i} \zeta^i (1 - \zeta)^{N-i} \frac{\lambda^{m-i}}{(m-i)!} e^{-\lambda} \quad (2.3)$$

The expression in (2) represents a convolution of Poisson and Binomial probability mass functions. This result is the primary means of inference of the number of active emitters  $N$  in a ROI.

In order to begin to perform localization in non-sparse ROIs, we write a posterior distribution on the Binomial parameters used in the likelihood (2) using Bayes rule. When  $\lambda$  is known, we have

$$p(N, \zeta | x) \propto p(x | N, \zeta) p(\zeta) \quad (2.4)$$

We use a Gaussian prior on  $\zeta$  i.e.,  $p(\zeta) = \mathcal{N}(\mu_\zeta, \sigma_\zeta)$  with  $\mu_\zeta = 0.01$  and  $\sigma_\zeta = 0.005$ . Prior uncertainty in the value of  $\zeta$  stems from fluorophores with potentially heterogeneous photophysical properties as well as varying laser power throughout the excited region. This posterior can be integrated over  $\zeta$  to produce a posterior distribution on the fluorophore number  $N$  i.e.,  $p(N = N' | n) \propto \int_0^1 \prod_{j=1}^{N_{\text{frames}}} p(n_j | N', \zeta) p(\zeta) d\zeta$  which can be estimated using

Monte Carlo methods. Monte Carlo integration is employed to integrate out  $\zeta$ . This involves sampling many  $\zeta$  values from the Gaussian prior. For each sampled  $\zeta$ , the Poisson-Binomial likelihood  $p(n|\zeta_i)$  is computed. These likelihood values are then weighted by the prior probabilities  $p(\zeta)$ . The final result is obtained by averaging these weighted likelihoods over all sampled  $\zeta$ , which approximates the integral:

$$\int p(x|\zeta)p(\zeta) d\zeta \approx \frac{1}{M} \sum_{i=1}^N p(x|\zeta_i)p(\zeta_i)$$

where  $M$  is the number of samples from the prior. This method provides a powerful way to handle the integration of complex or high-dimensional functions, especially when analytical solutions are intractable.

The final posterior is then estimated by minibatching the data into batches of  $10^3$  frames and averaging the posterior  $p(N|n)$  over minibatches. The fluorophore number  $N$  within each ROI is then estimated by the maximum a posteriori (MAP) estimate  $N^*$  given by this distribution.

For localization, we notice that (2) is well approximated by a Poisson distribution for a large frame number, making the localization procedure similar to conventional maximum likelihood methods discussed in Chapter 1. Therefore, we have the following log-likelihood

$$\ell(n|\theta) = -\log \prod_k \frac{e^{-(\mu_k)} (\mu_k)^{n_k}}{n_k!} \quad (2.5)$$

$$= \sum_k \log n_k! + \mu_k - n_k \log (\mu_k) \quad (2.6)$$

where, in the multi-emitter regime the expected photon count at a pixel is  $\mu_k = \sum_{m=1}^{N^*} \mu_{k,m}$  and  $\mu_{k,m} = \zeta N_{\text{frames}} \Gamma_x(u_k, \theta_{u,m}) \Gamma_y(v_k, \theta_{v,m}) + \lambda N_{\text{frames}}/d^2$ . In the multi-emitter regime, optimization of the likelihood can be more challenging, and sampling is a more suitable choice (see Results).

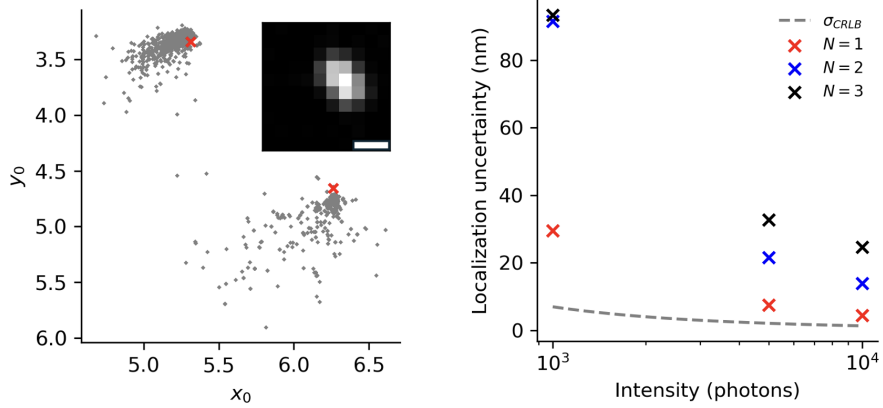


**Figure 2.5. Single and multi-emitter localization error on sums of photon counts.** (left) Localization uncertainty for simulated data for different values of  $N$ , plotted with respect to the Cramer-Rao lower bound, shown in dashed gray. (right) Multi-emitter localization by MCMC sampling for  $N = 3$ , colors indicate a cluster of samples i.e., a single localization. All data was generated with a background rate  $\langle n_{\text{background}} \rangle = \lambda N_{\text{frames}} / d^2$  per pixel. Scalebar 360nm

## 2.2.2 Results

Quantum dots coated on a glass coverslip were excited using a picosecond 532nm pulsed laser triggered at 500kHz. Emission light was collected using an oil-immersion 100 $\times$  objective with numerical aperture (NA) 1.4 (Nikon). The emission signal was then filtered to exclude the laser line (Semrock) and projected onto the SPAD512 sensor (Pi Imaging Technologies) using a tube lens. A simplified diagram of the complete system is depicted in (Figure 2.3 a). Each acquisition consists of  $N = 5 \times 10^5$  frames, synchronized with each laser pulse, using a 1us exposure per frame (Figure 2.3 b,d). Example posteriors and multi-emitter fitting on experimental quantum dot data are found in (Figure 2.4). To confirm the presence of single photon sources in the sample, we investigated properties of the zero-lag second order coherence function  $g^{(2)}(0)$ . The following empirical estimate of  $g^{(2)}(0)$  is used [24]

$$g^{(2)}(0) = \frac{G^{(2)}(0) - B}{\langle G^{(2)}(m \neq 0) \rangle - B} \quad (2.7)$$

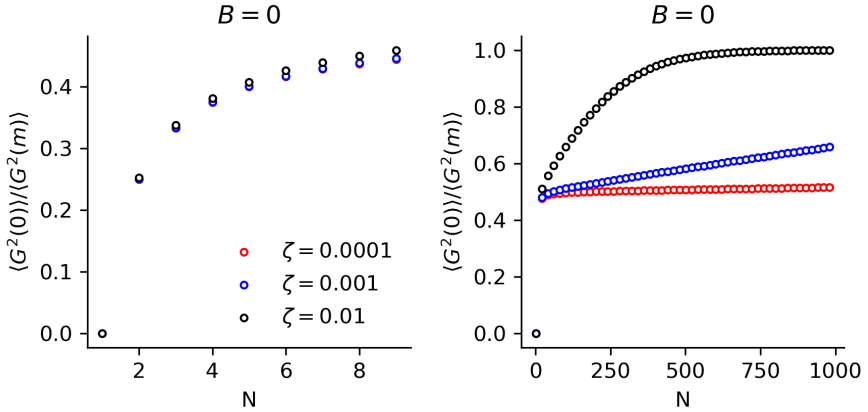


**Figure 2.6. Scaling of  $g^{(2)}(0)$  under zero background conditions.** (left) Scaling of  $g^{(2)}(0)$  for small  $N$ . (right) Scaling of  $g^{(2)}(0)$  for large  $N$

where  $B = N_{\text{frames}}\lambda\zeta$  is the expected number of background-signal coincidences in the region of interest. The quantity  $G^{(2)}(m)$  represents the number of signal-signal coincidences in the region of interest at a lag time  $m$ . The quantity  $\langle G^{(2)}(m \neq 0) \rangle$  is the average number of coincidences in pairs of frames at nonzero lag  $m \in [1, 100]$ , in units of frames. As expected, simulation from the likelihood (2) shows saturation of  $g^{(2)}(0)$  with increasing values of  $N$  (Figure 2.3c). Averaging  $G^{(2)}(0)$  over many realizations (sequences of  $N_{\text{frames}}$ ), gives the expected value  $\langle G^{(2)}(0) \rangle$

$$\langle G^{(2)}(0) \rangle = N_{\text{frames}}(1 - (1 - \zeta)^n - n\zeta(1 - \zeta)^{n-1}) \quad (2.8)$$

Since  $G^{(2)}(m)$  is already averaged over  $m$ ,  $\langle G^{(2)}(m) \rangle$  is effectively a constant over realizations, and must be

$$\langle G^{(2)}(m) \rangle = N_{\text{frames}}(1 - ((1 - \zeta)^n))^2 \quad (2.9)$$

Ignoring the effect of background signal  $\langle g^{(2)}(0) \rangle = \langle G^{(2)}(0) \rangle / \langle G^{(2)}(m) \rangle$ , which rapidly approaches 1/2 as a function of  $N$ , and then saturates and very slowly approaches its maximum value of 1 (Figure 2.6). This is consistent with the idea that for very large number of active fluorescent emitters, the statistics should become Poisson. Moreover, bright clusters of

quantum dots exhibit elevated  $g^{(2)}(0)$  values as can be seen in maps of the  $g^{(2)}(0)$  computing using a sliding window over the array (Figure 2.3 e).

For localization by optimization of (4), we use Goodman and Weare’s Markov Chain Monte Carlo (MCMC) algorithm [25] to sample from the posterior on fluorophore locations. In all simulations we assume a uniform prior on coordinates over the ROI and  $\zeta$  is known and identical over fluorophores. Fluorophore locations can then be estimated from the posterior samples by K-means clustering of the  $(\theta_u, \theta_v)$  coordinates of the first particle and identification of cluster centers. To validate our estimator, we compare its RMSE to the single emitter Cramer-Rao lower bound (Figure 2.5).

We find that for thousands of expected signal photon counts, localization uncertainty lies in an acceptable range for localization microscopy (Figure 2.5). The  $\zeta$  value is treated as unknown but homogeneous across fluorophores in the ROI.

### 2.2.3 Discussion

Fluorescence intermittency can affect the observed photon-number fluctuations and could be expected to affect the value of  $g^{(2)}(0)$  or the posterior on the number of active fluorescent emitters. However, the signal photon number per frame will follow Binomial statistics even in the presence of blinking, the only consequence of which is an effective reduction of the detection probability  $\zeta$ . If the effect of censoring photons by blinking and lowering the quantum yield can be accounted for, the technique used here may be compatible with common super-resolution techniques such as stochastic optical reconstruction microscopy (STORM).

The acquisition times necessary to obtain sufficient photon counts for computing the necessary statistics can potentially be very short. Most fluorophores have relaxation times in the nanosecond range and thus photons can be collected at a rate of at tens of millions of excitation pulses per second. These rates are currently difficult to obtain, however, due to limitations in detector throughput. The SPAD camera used in this study has a minimum exposure time in the microsecond range. Furthermore, the data volume can quickly become intractable due to the need for several thousands of frames for a millisecond-scale exposure time. This is currently a complication for techniques like STORM and advancements in

the automation for data acquisitions are necessary. The speed of MCMC based localization remains a limitation for post-processing, and optimization of the processing time for localization is left for future work.

In conclusion, we propose a single molecule imaging technique that allows for simultaneous counting of localization of fluorescent molecules by modeling the quantum properties of fluorescence emission. The technique does not require a nonclassical light source and is designed to supplement standard single molecule localization microscopy techniques. The proposed method can be implemented with a standard widefield fluorescence microscope.

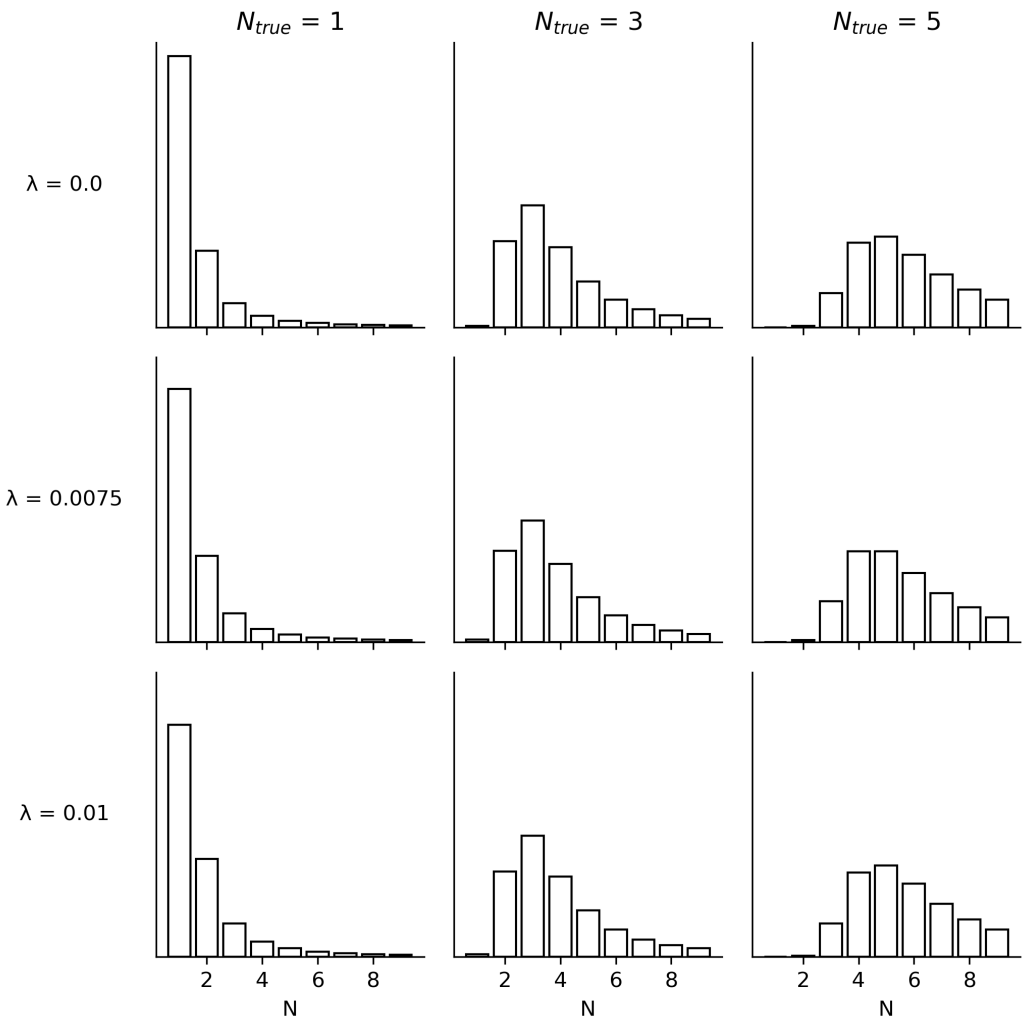


**Figure 2.7. Posterior distributions of the fluorophore number.** Samples from the Poisson-Binomial convolution distribution using  $\zeta = 0.01$  for various values of  $\lambda$  and  $N = 1, 3, 5$  were simulated. The variable  $\zeta$  was integrated out by Monte Carlo integration, sampling 1000  $\zeta$  values from the posterior distribution (see main text for details)

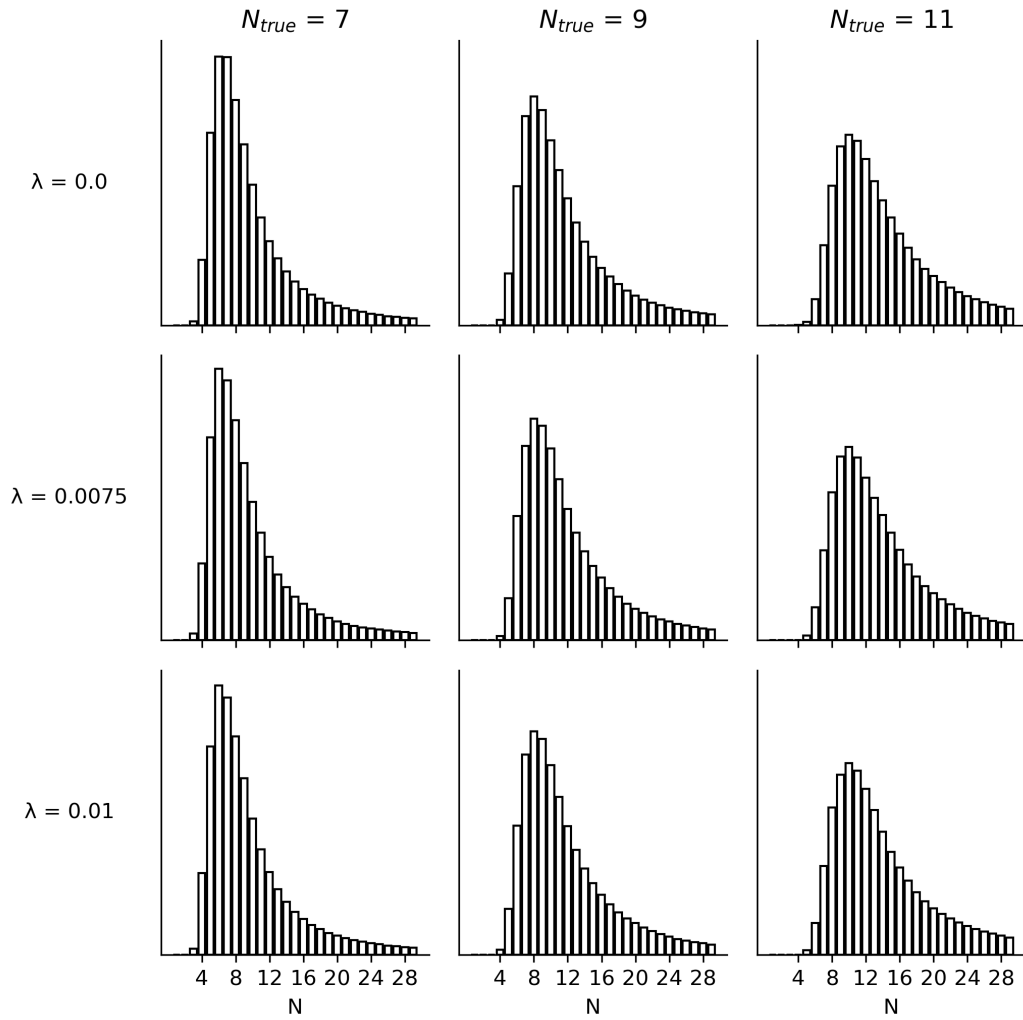


**Figure 2.8. Posterior distributions of the fluorophore number.** Samples from the Poisson-Binomial convolution distribution using  $\zeta = 0.01$  for various values of  $\lambda$  and  $N = 7, 9, 11$  were simulated. The variable  $\zeta$  was integrated out by Monte Carlo integration, sampling 1000  $\zeta$  values from the posterior distribution (see main text for details)

### 3. Uncertainty-aware localization microscopy by variational diffusion

#### 3.1 Introduction

##### 3.1.1 The curse of dimensionality

Dimensionality refers to the number of variables or features in a dataset. In conventional fluorescence nanoscopy, an image generated by (1.1) containing  $M$  fluorophores has  $2M$  parameters. Similarly, the image itself is a high dimensional variable where the number of pixels is the number of dimensions. As the number of dimensions in the parameter space increases, it becomes increasingly difficult to infer the parameters from the data. The curse of dimensionality is a term coined to describe various phenomena that arise when working with high-dimensional data, making statistical analysis and machine learning more challenging. Mathematically, the curse of dimensionality can be described through the following issues.

As dimensionality increases, the volume of the space grows exponentially. For instance, the volume of a hypercube with side length  $l$  in  $d$ -dimensional space is given by  $l^d$ . This rapid increase in volume means that data points become sparser, making it difficult to estimate densities and find meaningful patterns. Furthermore, in high-dimensional spaces, the concept of distance becomes less informative. The difference between the minimum and maximum distance between data points tends to shrink as dimensionality increases, which can make clustering and nearest-neighbor algorithms less effective. With a large number of dimensions, models can easily become overly complex, capturing noise instead of the underlying signal. This leads to overfitting, where the model performs well on training data but poorly on unseen data.

Deep models have captured the attention of many researchers, as they can perform inference tasks in high dimensional spaces without an excessive computational burden. These models are not entirely immune to the curse of dimensionality or the complexity of data distributions, however, and overfitting is still an important problem. Simultaneously, many deep models are deterministic neural networks, which give a single output given an input. This is in sharp contrast to classical statistical inference methodologies such as Bayesian inference, which model a distribution on their outputs, allowing one to express uncertain-

ties during inference. Bayesian methods such as Markov Chain Monte Carlo (MCMC) or variational inference lack the scaling of deep learning but maintain a scientific value [26].

### 3.1.2 The Bayesian calculation

Bayesian inference provides a rigorous framework for updating beliefs about the world in light of new data. It leverages the principles of probability theory to combine prior knowledge with empirical evidence, resulting in updated, posterior beliefs. In parametric modeling, we assume that the data  $x$  are generated from a distribution with a set of parameters  $y$ . Parametric models simplify the problem by assuming a specific form for the underlying distribution of the data, characterized by a finite set of parameters. This approach allows us to use mathematical functions to describe complex systems and make inferences about the parameters based on observed data.

At the heart of Bayesian inference is Bayes' rule, which allows us to update our beliefs based on new evidence. Bayes' rule is derived from the definition of conditional probability. The conditional probability of  $y$  given  $x$  is defined as  $p(y|x) = \frac{p(x,y)}{p(y)}$  provided that  $p(y) > 0$ . Similarly, the conditional probability of  $x$  given  $y$  is  $p(x|y) = \frac{p(x,y)}{p(x)}$ . Rearranging these equations and solving for  $p(y|x)$  gives us Bayes' rule:

$$p(y|x) = \frac{p(x|y)p(y)}{p(x)}.$$

Here,  $p(y|x)$  is the called the posterior distribution, representing our updated beliefs about the parameters after observing the data.  $p(x|y)$  is the likelihood, the probability of the observed data given the parameters.  $p(y)$  is the prior distribution, representing our beliefs about the parameters before observing the data.  $p(x)$  is the marginal likelihood or evidence, which normalizes the posterior distribution and ensures it sums to one.

One of the main challenges in Bayesian inference is the computation of the posterior distribution. The denominator in Bayes' rule,  $p(x)$ , involves an integral over all possible values of the parameters:

$$p(x) = \int p(x|y)p(y) dy.$$

In many practical applications, this integral is intractable due to the high dimensionality of the parameter space. To address this challenge, various approximation methods have been developed. One such method is Markov Chain Monte Carlo (MCMC), which generates samples from the posterior distribution by constructing a Markov chain that has the desired distribution as its equilibrium distribution. MCMC methods, such as the Metropolis-Hastings algorithm and the Gibbs sampler, allow us to approximate the posterior distribution even when the exact integral is computationally infeasible. MCMC algorithms were originally developed in the 1940s by physicists at Los Alamos. These physicists, including Ulam and Von Neumann, who were interested in modeling the probabilistic behavior of physical systems. They could not do this analytically, but they wondered if they could use simulation. Ulam and Metropolis overcame this problem by constructing a Markov chain for which the desired distribution was the stationary distribution of the Markov chain. They then only needed to simulate the Markov chain until equilibrium was achieved. This became the famous Metropolis algorithm, and its impact was enormous. Afterwards, MCMC was introduced to statistics and generalized with the Metropolis algorithm and its variants as well as the Gibbs sampler [27]

### 3.1.3 Variational inference

Another approach to approximating the posterior distribution is variational inference. This method involves approximating the true posterior distribution  $q(y|x)$  with a simpler, parameterized distribution  $p_\psi(y)$  by minimizing the Kullback-Leibler (KL) divergence between them. The KL divergence  $D_{KL}(q(y|x)||p_\psi(y))$  measures how one probability distribution diverges from a second probability distribution. To minimize the KL divergence, we first express it as

$$D_{KL}(q(y|x)||p_\psi(y)) = \mathbb{E}_{q(y|x)} \left[ \log \frac{q(y|x)}{p_\psi(y)} \right]$$

This can be rewritten using Bayes' rule as

$$\begin{aligned}
D_{KL}(q(y|x)||p_\psi(y|x)) &= \mathbb{E}_{q(y|x)} \left[ \log \frac{q(y|x)}{p_\psi(y|x)} \right] \\
&= \mathbb{E}_{q(y|x)} \left[ \log \frac{q(y|x)p_\psi(x)}{p_\psi(x,y)} \right] \\
&= \mathbb{E}_{q(y|x)} \left[ \log \frac{q(y|x)}{p_\psi(x,y)} \right] + \mathbb{E}_{q(y|x)} [\log p_\psi(x)]
\end{aligned}$$

Defining  $\mathcal{L} = -\mathbb{E}_{q(y|x)} \left[ \log \frac{q(y|x)}{p_\psi(x,y)} \right] = \mathbb{E}_{q(y|x)} \left[ \log \frac{p_\psi(x,y)}{q(y|x)} \right]$ , we can write,

$$\mathbb{E}_{q(y|x)} [\log p_\psi(x)] = D_{KL}(q(y|x)||p_\psi(y|x)) + \mathcal{L} \geq \mathcal{L}$$

which is often called a variational objective. Given that  $\log p_\psi(x)$  is constant, minimizing  $D_{KL}(q(y|x)||p_\psi(y|x))$  is equivalent to maximizing  $\mathcal{L}$ . For practical reasons, we often instead solve a minimization problem with respect to  $\psi$

$$\mathbb{E}_{q(y|x)} [-\log p_\psi(x)] \leq -\mathcal{L} = \mathbb{E}_{q(y|x)} \left[ -\log \frac{p_\psi(x,y)}{q(y|x)} \right]$$

This approach provides a practical way to perform Bayesian inference, especially in high-dimensional settings. It is worth noting that this derivation often begins with  $D_{KL}(p_\psi(y|x)||q(y|x))$  such that the expectation is taken with respect to the model distribution, since the true distribution is unknown. However, for the following application, the target distribution is known and thus the objective is prudently formulated in this way.

### 3.1.4 A note on variational inference for functions

For some applications, we would like to perform inference when the mapping between latents and observed data is deterministic. For example, there might be a deterministic mapping  $f$  between high resolution images and low-resolution ones, and we want to infer the high resolution image from the low resolution image. In that case, we find

$$\begin{aligned}
\mathbb{E}_{q(y|x)}[-\log p_\psi(x)] &\leq \mathbb{E}_{q(y|x)}\left[-\log \frac{p_\psi(x,y)}{q(y|x)}\right] \\
&= \mathbb{E}_{q(y|x)}\left[-\log \frac{p_\psi(y)}{q(y|x)}\right] + \mathbb{E}_{q(y|x)}[-\log p_\psi(x|y)] \\
&= \mathbb{E}_{q(y|x)}\left[-\log \frac{p_\psi(y)}{q(y|x)}\right] + \mathbb{E}_{q(y|x)}[-\log \delta(x - f(y))]
\end{aligned}$$

The second term is to be safely neglected, as it is undefined and provides no meaningful information during optimization.

### 3.1.5 Blending Bayesian inference with deep models for microscopy

Deep models have attracted tremendous attention from researchers in the natural sciences, with several foundational applications arising in microscopy [28], [29]. Recently, the application of deep image translation in nanoscopy has received considerable interest. Recently, the use of deep models to perform localization has been proposed as an alternative to traditional localization algorithms, in order to increase imaging speed and labeling density. In previous applications of deep models to localization microscopy, super-resolution images have been recovered from a sparse set of localizations with conditional generative adversarial networks [30] or localization itself can be performed using traditional convolutional networks [31], [32]. Here, we perform localization indirectly by predicting kernel density (KD) estimates of a population of fluorescent molecules using a deep model.

Kernel density estimation in nanoscopy is necessarily performed using a single low-resolution image, and thus common measures of model performance are based on localization errors computed over ensembles of simulated images. Unfortunately, this choice precludes computation of uncertainty at test time under a fixed model. Bayesian probability theory is therefore an attractive alternative, which offers us mathematically grounded tools to reason about uncertainty.

We model a posterior on high-resolution KD estimates conditioned on a low-resolution image. Our approach is based on a type of score based generative model [33], referred to as a denoising diffusion probabilistic model (DDPM) in the literature [33], [34]. We find that this

technique is complementary to relevant existing approaches to uncertainty estimation, which would primarily address epistemic sources of uncertainty, using techniques such as ensembling [35] or Monte Carlo dropout [36]. The approach is inspired by recent variational perspectives on diffusion [37]–[40]. Such techniques provide a mechanism for scalable variational inference, which can be trained using a variational bound written in terms of the signal-to-noise ratio of the diffused data, and a simple noise estimation loss. Indeed, recent efforts have shown that the variational bound can be reparameterized to give several more conventional diffusion losses [38]–[40].

In the remainder of this chapter, we introduce KD estimation as an alternative to direct localization using low-resolution images, followed by demonstration of our variational diffusion model for measuring uncertainty estimation at scale.

## 3.2 Results

We now consider datasets  $(\mathbf{x}_i, \mathbf{y}_{0,i}, \hat{\mathbf{y}}_i)_{i=1}^N$  of observed images  $\mathbf{x}_i$  true KD images  $\mathbf{y}_{0,i}$ , and augmented low-resolution inputs  $\hat{\mathbf{y}}_i = \phi(\mathbf{x}_i)$ , where  $\phi$  is a CNN.

### 3.2.1 Approach

Direct optimization of the image likelihood from observations  $\mathbf{x}$  alone is challenging when fluorescent emitters are dense within the field of view and fluorescent signals significantly overlap. However, convolutional neural networks (CNNs) have recently proven to be powerful tools fluorescence microscopy to extract parameters describing fluorescent emitters such as color, emitter orientation,  $z$ -coordinate, and background signal [41]–[43]. For localization tasks, CNNs typically employ upsampling layers to reconstruct Bernoulli probabilities of emitter occupancy [32] or KD estimates with higher resolution than experimental measurements [31]. We choose to use KD estimates in our model, denoted by  $\mathbf{y}$ , which are latent in the low-resolution data  $\mathbf{x}$ . KDEs are the most common data structure used in SMLM, and can be easily generated from molecular coordinates, alongside observations  $\mathbf{x}$ .

Kernel density estimates produced by the traditional deep architectures for localization microscopy produce strong results, but lack uncertainty quantification. Unfortunately, the

posterior can be difficult to compute at test time, since molecules cannot be easily resolved and therefore its dimensionality is ill-defined. The central goal of this paper is to instead model a conditional distribution on the latent  $\mathbf{y}$ :  $p(\mathbf{y}|\mathbf{x})$ , where  $\mathbf{y}$  is of known dimensionality. We choose to model  $p(\mathbf{y}|\mathbf{x})$  with a diffusion model, given that the distribution  $p(\mathbf{y}|\mathbf{x})$  is expensive to compute.

Sampling from diffusion models can be computationally expensive, given that generation amounts to solving a complex stochastic differential equation, effectively mapping a simple base distribution to the complex data distribution. The solution of such equations requires numerical integration with very small step sizes, resulting in thousands of neural network evaluations [44], [45]. For conditional generation tasks in high-risk applications, generation complexity is further exacerbated by the need for the highest level of detail in generated samples. Therefore, we propose that sampling is preceded by an augmentation network  $\phi$ , which in essence generates an initial estimate to guide the diffusion process. Reasoning for this choice in our application is two-fold:

**Synthesis Speed.** By training the augmentation network  $\phi$  to obtain an approximate estimate of the KDE, we can reduce the number of iterations, since the diffusion model only needs to model the remaining mismatch, resulting in a less complex model from which sampling becomes easier. Speed is critical in SMLM applications, which can produce thousands of images in a single experiment.

**Sample Fidelity.** Since diffusion will often be initialized in low-density regions of the data distribution, inaccurate score estimation in these regions will negatively affect the sampling process. Moreover, mixing can be difficult because of the need of traversing low density regions to transition between modes of the distribution [46].

### 3.2.2 Variational diffusion

Diffusion models [33], [34] are a class of generative models originally inspired by nonequilibrium statistical physics, which slowly destroy structure in a data distribution via a fixed

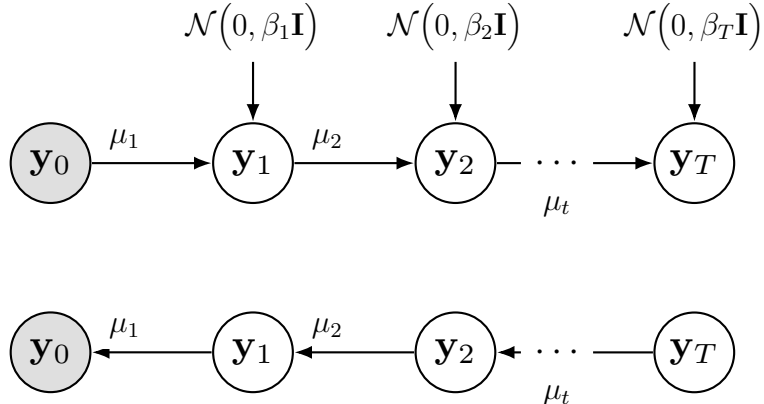


**Figure 3.1.** Diffusion model with Markovian transitions and reversed arrows

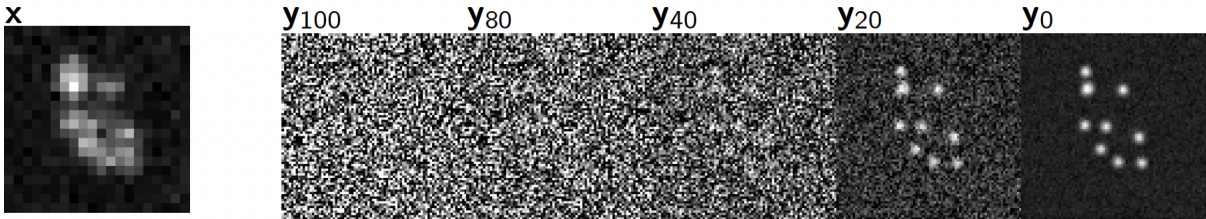


**Figure 3.2. Super resolution by variational diffusion.** Example diffusion process of the latent high resolution image  $\mathbf{y}$  conditioned on the low resolution image  $\mathbf{x}$ . The terminal  $\mathbf{y}_0$  represents a sample from  $p(\mathbf{y}|\mathbf{x})$ .

Markov chain referred to as the *forward process*. In the present context, we leverage the variational interpretation of this model class [39], [40] to approximate the posterior  $p(\mathbf{y}|\mathbf{x})$ .

**Diffusion Model.** We use a forward process which gradually adds Gaussian noise to the latent  $\mathbf{y}_0$  in discrete time, according to a variance schedule  $\beta_t$ :

$$q(\mathbf{y}_T|\mathbf{y}_0) = \prod_{t=1}^T q(\mathbf{y}_t|\mathbf{y}_{t-1}) \quad q(\mathbf{y}_t|\mathbf{y}_{t-1}) = \mathcal{N}\left(\sqrt{1-\beta_t}\mathbf{y}_{t-1}, \beta_t I\right) \quad (3.1)$$

An important property of the forward process is that it admits sampling  $\mathbf{y}_t$  at an arbitrary timestep  $t$  in closed form [34]. Using the notation  $\alpha_t := 1 - \beta_t$  and  $\gamma_t := \prod_{s=1}^t \alpha_s$ , we have  $q(\mathbf{y}_t|\mathbf{y}_0) = \mathcal{N}\left(\sqrt{\gamma_t}\mathbf{y}_0, (1 - \gamma_t)I\right)$  or  $\mathbf{y}_t = \sqrt{\gamma_t}\mathbf{y}_0 + \sqrt{1 - \gamma_t}\epsilon$  for  $\epsilon \sim \mathcal{N}(0, I)$ . The signal to noise ratio (SNR) as defined in [40], at a time step  $t$  reads  $\text{SNR}_t = \gamma_t/(1 - \gamma_t)$ .

The usual procedure is then to learn a parametric representation of the *reverse process*, and therefore generate samples of the latent  $\mathbf{y}_0$  from  $p(\mathbf{y}_0|\mathbf{x})$ . Formally,  $p_\psi(\mathbf{y}_0|\mathbf{x}) = \int p_\psi(\mathbf{y}_{0:T}|\mathbf{x})d\mathbf{y}_{1:T}$  where  $\mathbf{y}_t$  is a latent representation with the same dimensionality of the data and  $p_\psi(\mathbf{y}_{0:T}|\mathbf{x})$  is a Markov process, starting from a noise sample  $p_\psi(\mathbf{y}_T) = \mathcal{N}(0, I)$ . Writing this Markov process gives

$$p_\psi(\mathbf{y}_{0:T}|\mathbf{x}) = p_\psi(\mathbf{y}_T) \prod_{t=1}^T p_\psi(\mathbf{y}_{t-1}|\mathbf{y}_t, \mathbf{x}) \quad p_\psi(\mathbf{y}_{t-1}|\mathbf{y}_t, \mathbf{x}) = \mathcal{N}(\mu_\psi(\mathbf{y}_t, \gamma_t), \beta_t I) \quad (3.2)$$

where we reuse the variance schedule of the forward process [34]. From (5) it can be seen that the learnable parameter in the reverse process is the expectation of the transition  $\mu_\psi$  where  $\psi$  is a neural network.

Learning the reverse process can be approached by either regressing noise  $\epsilon$  from the forward process, or the true latent  $\mathbf{y}_0$ , as there is a deterministic relationship between them. We adopt the former for consistency with other work, and define  $\psi$  as a neural denoising function which regresses the noise  $\epsilon$  from a noisy  $\mathbf{y}_t$ . A relation between the noise estimate  $\epsilon_\psi$  and  $\mu_\psi$  is given in the Appendix, which gives an intuition for sampling. The proposed sampling scheme is depicted in (Figure 3.2).

**Variational Objective.** Following [39], we interpret the reverse process as a hierarchical generative model that samples a sequence of latents  $\mathbf{y}_t$ , with time running backward. Training of the model is achieved through the variational bound

$$-\log p(\mathbf{y}_0) \leq -\mathbb{E}_{q(\mathbf{y}_{1:T}|\mathbf{y}_0)} \log \left( \frac{p_\psi(\mathbf{y}_{1:T}, \mathbf{y}_0)}{q(\mathbf{y}_{1:T}|\mathbf{y}_0)} \right) \quad (3.3)$$

$$= D_{KL}(q(\mathbf{y}_T|\mathbf{y}_0)||p(\mathbf{y}_T)) + \mathbb{E}_{q(\mathbf{y}_1|\mathbf{y}_0)} \log p(\mathbf{y}_0|\mathbf{y}_1) + \mathcal{L}_\psi \quad (3.4)$$

where we have omitted conditioning on the low-resolution  $\mathbf{x}$  to simplify the notation. Note that, this is similar to a hierarchical VAE, but in a diffusion model  $q(\mathbf{y}_{1:T}|\mathbf{y}_0)$  is fixed by the forward process rather than learned. The so-called diffusion loss  $\mathcal{L}_\psi$  is shown in the Appendix, and is the term of interest as the first two terms do not contribute meaningfully to the loss [34]. Furthermore, it has become standard to use simplified forms of  $\mathcal{L}_\psi$ , such as

a noise estimation loss, as this has shown superior performance. Importantly,  $\mathcal{L}_\psi$  is simply a reweighted variant of a family of diffusion objectives [39], [40]. We use the following Monte Carlo estimate of  $\mathcal{L}_\psi$ , which demonstrates that the variational bound can be written in terms of the common noise-estimation loss

$$\mathcal{L}_\psi = \mathbb{E}_{\epsilon \sim \mathcal{N}(0, I), t \sim U(1, T)} \left[ \left( \frac{\text{SNR}_{t-1}}{\text{SNR}_t} - 1 \right) \|\epsilon - \epsilon_\psi\|_2^2 \right] \quad (3.5)$$

A full derivation of this objective is outlined in the Appendix. Note that  $\text{SNR}_t$  is monotonically decreasing with  $t$ , and thus  $\frac{\text{SNR}_{t-1}}{\text{SNR}_t} = \frac{\gamma_{t-1}}{\gamma_t} \frac{1-\gamma_t}{1-\gamma_{t-1}} \geq 1$ , ensuring  $\mathcal{L}_\psi \geq 0$ . In this paper, we choose to use a uniformly weighted loss and leave the exploration of the weighted loss to future work.

### 3.2.3 Experiments

All training data consists of low-resolution  $20 \times 20$  images, setting  $\sigma_x = 0.92$  in units of low-resolution pixels, for consistency with common experimental conditions with a 60x magnification objective lens and numerical aperture (NA) of 1.4. We multiply  $\omega_k$  by a constant  $i_0 = 200$  for experiments for consistency with typical fluorophore emission rates. All KDEs have dimension  $80 \times 80$ , are scaled between  $[0, 1]$ , and are generated using  $\sigma_y = 3.0$  pixels in the upsampled image (Figure 3.3). For a typical CMOS camera, this results in KDE pixels with lateral dimension of  $\approx 27\text{nm}$ . Initial coordinates  $\theta$  were drawn uniformly over a two-dimensional disc with a radius of 7 low-resolution pixels.

**Localization RMSE.** In order to verify the initial predictions made by the augmentation model  $\phi$ , we simulated a dataset  $(\mathbf{x}_i, \mathbf{y}_{0,i}, \hat{\mathbf{y}}_i)_{i=1}^N$  with  $N = 1000$ . Objects in the KDE  $\hat{\mathbf{y}}_i$  are detected using the Laplacian of Gaussian (LoG) detection algorithm [4], which permits more direct comparison of model predictions to the Cramer-Rao lower bound on localization error, compared to other image similarity measures (Figure 3.4). Localization is carried out from scale-space maxima directly in LoG, as opposed to fitting a model function to KDEs. A particular LoG localization in the KDE is paired to the nearest ground truth localization and is unpaired if a localization is not within 5 KDE pixels of any ground truth localization. In addition to localization error, we measure a precision  $P = \text{TP}/(\text{TP} + \text{FP}) = 1.0$  and recall

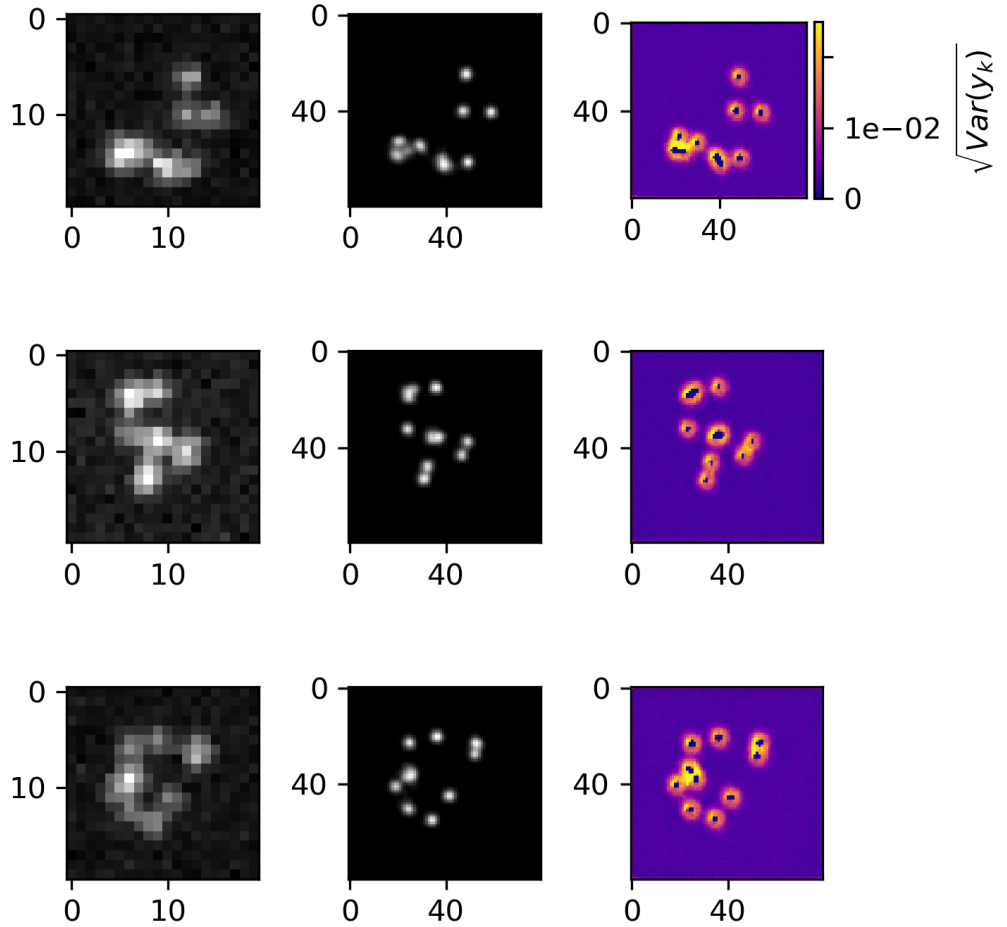


**Figure 3.3. Non cherry-picked estimation of marginal variances.** A low-resolution image  $\mathbf{x}$  (left column) is transformed by  $\phi$  to produce a KDE estimate  $\hat{\mathbf{y}}$  (middle column) and a DDPM  $\psi$  computes a map of marginal variances (right column)

$R = TP / (TP + FN) = 0.85$ , where TP denotes true positive localizations, FP denotes false positive localizations, and FN denotes false negative localizations.

**Variational Diffusion.** We set  $T = 100$  for all experiments and treat forward process variances  $\beta_t$  as hyperparameters, with a linear schedule from  $\beta_0 = 10^{-4}$  to  $\beta_T = 10^{-2}$ . These constants were chosen to be small relative to ground truth KDEs, which are scaled to  $[-1, 1]$ , ensuring that forward process distribution  $\mathbf{y}_T \sim q(\mathbf{y}_T | \mathbf{y}_0)$  approximately matches the reverse process  $\mathbf{y}_T \sim \mathcal{N}(0, I)$  at  $t = T$ . Example KD estimates from low-resolution images and the marginal variances obtained from sampling  $N = 100$  samples from  $p_\psi(\mathbf{y}_0 | \mathbf{x})$  are shown in (Figure 4).

### 3.3 Conclusion

We proposed a variational diffusion model for uncertainty-aware localization microscopy. Our approach builds on recent advancements in conditional diffusion models, to model the posterior distribution on high-resolution KD estimates from low-resolution inputs. This tractable posterior distribution is constructed by first augmenting low resolution inputs to a KD estimate using the DeepSTORM architecture with minor modifications [31]. Conditioning a diffusion model on this initial estimate permits sampling with relatively fewer samples than most existing diffusion models in similar applications, thereby making computation of marginal variances possible. Our approach made three core contributions: (i) we derived a relationship between the posterior on kernel density estimates with the posterior on molecular locations, and (ii) we demonstrated that a diffusion model can model a distribution on KDEs with qualitatively similar marginal variances expected from predictions made using MCMC. By using a recently discovered relationship of the variational lower bound to a traditional noise-estimation objective, we can confidently approximate the true posterior.

### 3.4 Broader impact

The development of a method for uncertainty estimation in super-resolution imaging, as proposed here, holds implications beyond its immediate application in SMLM. By leveraging diffusion models for uncertainty estimation, this approach not only enhances the reliability

of super-resolution image reconstructions but also extends its utility to a diverse array of domains. The incorporation of a guided diffusion process facilitates efficient reconstruction while maintaining interpretation of the underlying uncertainty. Importantly, the principles underlying this method resonate across various fields, suggesting its potential applicability in domains beyond microscopy. For instance, the extension of similar techniques to general image processing tasks highlights the potential to address uncertainty in a wide range of applications in bioimaging or medical imaging. Moreover, the utilization of diffusion models for uncertainty estimation aligns with a broader trend in leveraging probabilistic frameworks for enhancing deep learning applications, with implications extending to fields such as natural language processing, computer vision, and autonomous systems. By bridging these interdisciplinary boundaries, this method not only addresses a critical need in localization microscopy but also contributes to the advancement of uncertainty-aware deep learning methodologies.

## 3.5 Appendix

### 3.5.1 Sampling

Sampling from the reverse process  $p_\psi(\mathbf{y}_{t-1}|\mathbf{y}_t, \mathbf{x})$  is achieved by estimation of the noise  $\epsilon_\psi$  from  $\mathbf{y}_t$  by the denoising model  $\psi$ , and therefore estimation of  $\mathbf{y}_0$

$$\hat{\mathbf{y}}_0 = \frac{1}{\sqrt{\gamma_t}}(\mathbf{y}_t - \sqrt{1 - \gamma_t}\epsilon_\psi) \quad (3.6)$$

followed by sampling from the forward process  $\mathbf{y}_{t-1} \sim q(\mathbf{y}_{t-1}|\hat{\mathbf{y}}_0) = \mathcal{N}(\sqrt{\gamma_{t-1}}, (1 - \gamma_{t-1})I)$ .

### 3.5.2 Derivation of the variational bound

We now derive the so-called diffusion loss  $\mathcal{L}_\psi$ , written in (8) in the main text. Similar derivations can be found in [38], [39], and we include it here only for completeness

$$\begin{aligned}
-\log p(\mathbf{y}_0) &\leq -\mathbb{E}_{q(\mathbf{y}_{1:T}|\mathbf{y}_0)} \log \frac{p(\mathbf{y}_{0:T})}{q(\mathbf{y}_{1:T}|\mathbf{y}_0)} \\
&= -\mathbb{E}_{q(\mathbf{y}_{1:T}|\mathbf{y}_0)} \log \frac{p(\mathbf{y}_T)p(\mathbf{y}_0|\mathbf{y}_1)\prod_{t=2}^T p(\mathbf{y}_{t-1}|\mathbf{y}_t)}{q(\mathbf{y}_T|\mathbf{y}_0)\prod_{t=2}^T q(\mathbf{y}_{t-1}|\mathbf{y}_t, \mathbf{y}_0)} \\
&= -\mathbb{E}_{q(\mathbf{y}_{1:T}|\mathbf{y}_0)} \left[ p(\mathbf{y}_0|\mathbf{y}_1) + \log \frac{p(\mathbf{y}_T)}{q(\mathbf{y}_T|\mathbf{y}_0)} + \sum_{t=2}^T \log \frac{p(\mathbf{y}_{t-1}|\mathbf{y}_t)}{q(\mathbf{y}_{t-1}|\mathbf{y}_t, \mathbf{y}_0)} \right] \\
&= -\mathbb{E}_{q(\mathbf{y}_{1:T}|\mathbf{y}_0)} [p(\mathbf{y}_0|\mathbf{y}_1)] + D_{KL}(q(\mathbf{y}_T|\mathbf{y}_0)||p(\mathbf{y}_T)) \\
&\quad + \sum_{t=2}^T \mathbb{E}_{q(\mathbf{y}_t|\mathbf{y}_0)} D_{KL}(q(\mathbf{y}_{t-1}|\mathbf{y}_t, \mathbf{y}_0)||p(\mathbf{y}_{t-1}|\mathbf{y}_t))
\end{aligned}$$

As before, we omit conditioning on  $\mathbf{x}$  to simplify the notation. The first term is typically ignored, as it does not contribute meaningfully to the loss [38]. Furthermore, the second term is approximately zero by construction. Therefore we are left with the last term, called the diffusion loss  $\mathcal{L}_\psi$ . The KL-divergence of  $q$  and  $p$  is between two Gaussians with identical variances  $\sigma^2 = \frac{(1-\gamma_{t-1})(1-\alpha_t)}{1-\gamma_t}$ , and expectations

$$\mu = \frac{\sqrt{\gamma_{t-1}}(1-\alpha_t)}{1-\gamma_t} \mathbf{y}_0 + \frac{\sqrt{\alpha_t}(1-\gamma_{t-1})}{1-\gamma_t} \mathbf{y}_t \quad \mu_\psi = \frac{\sqrt{\gamma_{t-1}}(1-\alpha_t)}{1-\gamma_t} \hat{\mathbf{y}}_0 + \frac{\sqrt{\alpha_t}(1-\gamma_{t-1})}{1-\gamma_t} \mathbf{y}_t$$

for a fixed noise schedule [44]. Therefore, we have

$$\begin{aligned}
D_{KL}(q(\mathbf{y}_{t-1}|\mathbf{y}_t, \mathbf{y}_0)||p(\mathbf{y}_{t-1}|\mathbf{y}_t)) &= \frac{1}{2\sigma^2} \|\mu - \mu_\psi\|_2^2 \\
&= \frac{1}{2} \frac{\gamma_{t-1}(1-\alpha_t)}{(1-\gamma_{t-1})(1-\gamma_t)} \|\mathbf{y}_0 - \hat{\mathbf{y}}_0\|_2^2 \\
&= \frac{1}{2} \frac{\gamma_{t-1}((1-\gamma_t) - \alpha_t(1-\gamma_{t-1}))}{(1-\gamma_{t-1})(1-\gamma_t)} \|\mathbf{y}_0 - \hat{\mathbf{y}}_0\|_2^2 \\
&= \frac{1}{2} \frac{\gamma_{t-1}((1-\gamma_t) - \frac{\gamma_t}{\gamma_{t-1}}(1-\gamma_{t-1}))}{(1-\gamma_{t-1})(1-\gamma_t)} \|\mathbf{y}_0 - \hat{\mathbf{y}}_0\|_2^2 \\
&= \frac{1}{2} \left( \frac{\gamma_{t-1}}{1-\gamma_{t-1}} - \frac{\gamma_t}{1-\gamma_t} \right) \|\mathbf{y}_0 - \hat{\mathbf{y}}_0\|_2^2 \\
&= \frac{1}{2} (\text{SNR}_{t-1} - \text{SNR}_t) \|\mathbf{y}_0 - \hat{\mathbf{y}}_0\|_2^2
\end{aligned}$$

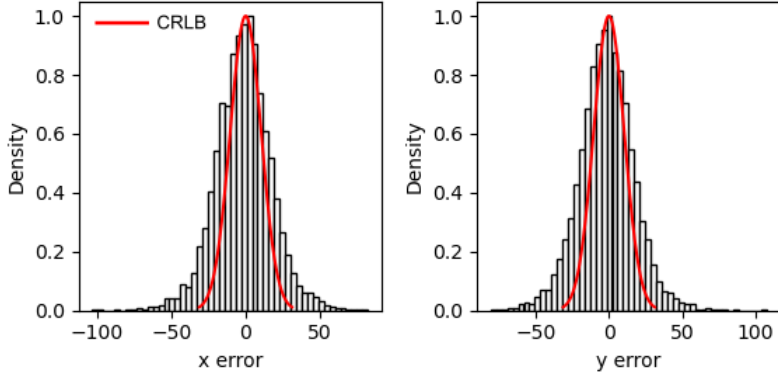


**Figure 3.4. Localization errors of the trained model  $\phi$ .** The Cramer-Rao lower bound is shown in red, computing by taking the diagonal elements of  $I^{-1}(\theta)$ .

Reparameterizing the loss in terms of the noise, using  $\|\mathbf{y}_0 - \hat{\mathbf{y}}_0\|_2^2 = \frac{1-\gamma_t}{\gamma_t} \|\epsilon_0 - \epsilon_\psi\|_2^2$  [38], we arrive at

$$\mathcal{L}_\psi = \frac{1}{2} \sum_{t=2}^T \mathbb{E}_{q(\mathbf{y}_t|\mathbf{y}_0)} \left( \frac{\text{SNR}_{t-1}}{\text{SNR}_t} - 1 \right) \|\epsilon - \epsilon_\psi\|_2^2$$

Using a Monte Carlo estimate of  $\mathcal{L}_\psi$  [40] which optimizes random terms of the summation to avoid calculating all terms simultaneously, we arrive at the objective written in the main text (8)

$$\mathcal{L}_\psi = \mathbb{E}_{\epsilon \sim \mathcal{N}(0, I), t \sim U(1, T)} \left[ \left( \frac{\text{SNR}_{t-1}}{\text{SNR}_t} - 1 \right) \|\epsilon - \epsilon_\psi\|_2^2 \right]$$

### 3.5.3 Neural network architectures

**DeepSTORM CNN  $\phi$ .** The DeepSTORM CNN (Figure 3.5), for 3D localization, can be viewed as a deep kernel density estimator, reconstructing kernel density estimates  $\mathbf{y}$  from low-resolution inputs  $\mathbf{x}$ . We utilize a simplified form of the original architecture [31] for 2D localization, which we denote  $\phi$  in this paper, which consists of three main modules: a multi-scale context aggregation module, an upsampling module, and a prediction module. For

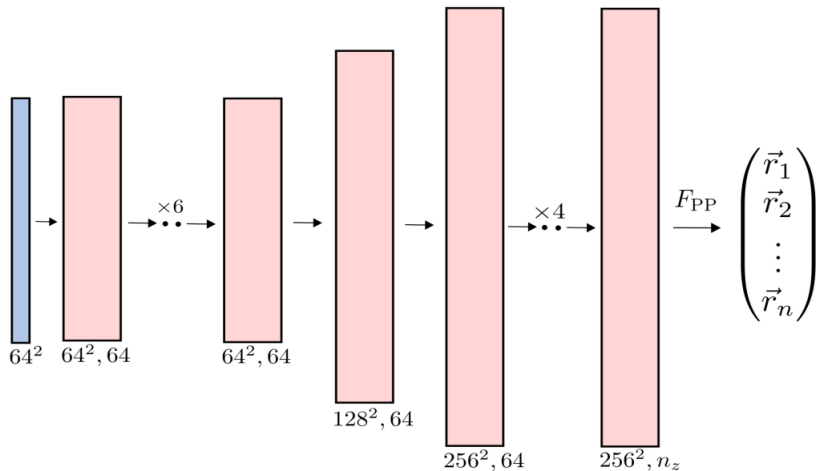


**Figure 3.5. Architecture of the augmentation model  $\phi$ .** A  $20 \times 20$  single-channel movie is processed by eight convolutional blocks followed by a 4x upsampling module utilizing linear interpolation and a refinement module with six convolutional blocks.

context aggregation, the architecture utilizes dilated convolutions to increase the receptive field of each layer. The upsampling module is then composed of two consecutive 2x resize-convolutions, computed by nearest-neighbor interpolation, to increase the lateral resolution by a factor of 4. Additional details regarding this architecture can be found in the original paper [31]. The terminal prediction module contains three additional convolutional blocks for refinement of the upsampled image, followed by an element-wise HardTanh. The architecture is trained using the objective  $\mathcal{L}_\phi = \frac{1}{N} \sum_{n=1}^N (\mathbf{y}_{0,n} - \hat{\mathbf{y}}_n)^2$ .

**DDPM  $\psi$ .** To represent the reverse process, we used a DDPM architecture (Figure 3.6) originally proposed in [44]. We chose the U-Net backbone to have channel multipliers  $[1, 2, 4, 8, 8]$  in the downsampling and upsampling paths of the architecture. In this architecture, parameters are shared across time, which is specified to the network using the Transformer sinusoidal position embedding, and uses self-attention at the  $16 \times 16$  feature map resolution. To condition the model on the input  $\hat{\mathbf{y}}$ , we concatenate the  $\hat{\mathbf{y}}$  estimated by DeepSTORM along the channel dimension, which are scaled to  $[0, 1]$ , with  $\mathbf{y}_T \sim \mathcal{N}(0, I)$ .

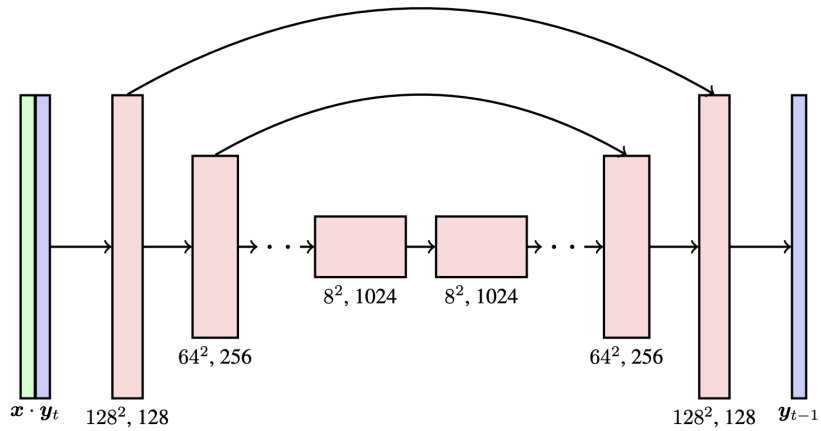


**Figure 3.6. Architecture of the denoising diffusion model.** A U-Net style architecture with channel multipliers of [1,2,4,8,16] downsamples and then upsamples the input image  $\mathbf{y}_t$  to estimate  $\mathbf{y}_{t-1}$

Others have experimented with more sophisticated methods of conditioning, but found that the simple concatenation yielded similar generation quality [44].

## 4. Fluorescence nanoscopy in the study of chromatin organization

### 4.1 Background on chromatin imaging

Chromatin is a complex and dynamic structure that packages eukaryotic DNA with histones. The higher-order structure of chromatin is highly non-random and plays an important role in regulation of genomic functions such as gene expression, DNA synthesis, and DNA repair. Chromatin structure and architecture are strictly controlled and constantly remodeled as cells differentiate, divide, and respond to genomic insults [47]–[51].

While DNA linearly encodes genetic information, serving as a template for RNA and protein production, the temporal and spatial organization of chromatin plays a fundamental role in determining intranuclear activities and gene stability [52], [53]. For example, local structural fluctuations in nucleosomes on microsecond to second timescales transiently expose buried DNA sites, thus providing temporary access to interaction sites [54]. Similarly, chromatin fibers are subject to rapid conformational dynamics [55]. This intrinsic motion of chromatin is closely linked to the underlying polymeric structure and directly affects molecular interactions at the local level by dictating the accessibility of DNA for various epigenetic effectors, chromatin regulators, and transcription factors (TFs). Indeed, the nanoscale spatiotemporal profile of chromatin may modulate the interaction of DNA with regulatory molecules, impacting the global patterns of gene expression [11], [56]–[58]. The dynamics of chromatin are best described by anomalous (particularly sub-diffusive) diffusion models [59], [60].

Most of what we know about local chromatin motion in chromatin remodeling has been derived from ensemble measurements, which provide a picture of biochemical access to chromatin over large populations of cells. Recently, advances using localization microscopy approaches have enabled the direct observation of the dynamics of individual molecules and the structure of chromatin domains in a single cell nucleus. These techniques, when paired with functional bioassays, permit the use of spatiotemporal localizations to make functional conclusions about genomic activities.

#### 4.1.1 Chromatin-associated-protein based labeling strategies

Core histones (H2A, H2B, H3, and H4), the fundamental units of chromatin tightly wrapped by DNA molecules, are common targets for imaging. In fixed cells, chromatin-associated proteins can be visualized through immunostaining with antibodies [9], [58], [61]. In live cells, histones can be directly fused with fluorescent proteins (FPs) [62]–[64].

Photo-activatable fluorescent proteins have been developed, allowing real-time control and quantitative characterization of protein clustering. Such strategies can be combined with other technical advancements such as single-molecule tracking and super-resolution imaging [10], [65], [66]. Alternatively, histone labeling in live cells can utilize prevalent self-label tags [67], [68], such as Halo Tag, Snap Tag, CLIP tag, and TMP Tag, which offer advantages like small size, brightness, photostability, monomerization, and adjustable fluorescent dye concentration, demonstrating superior performance in single-molecule imaging [10], [69], [70]. Other genomic elements can also be fluorescently labeled to assess structure and dynamics, including telomeres [71], centromeres [71], [72], H-NS or HU in *E. coli* [73], heterochromatin proteins [74], and transcription factors (TFs) [75], [76].

#### 4.1.2 Sequence specific labeling strategies

For fixed cell applications, fluorescence in situ hybridization (FISH) can detect and locate sequence-specific DNA or RNA in fixed cells using probes complementary to the target sequence [77], [78]. Primarily due to the need for cell permeabilization and sensitive hybridization conditions, FISH is limited to fixed cell samples.

Locus-specific labeling in live cells remains highly sought after. This can be achieved by either inserting artificial DNA sequences next to target genes, such as the repressoroperator array system (Lac operator (LacO) and Tet operator (TetO) systems), or by using modified genome-editing tools with inactive nucleases like zinc finger proteins (ZFPs), transcription activator-like effectors (TALEs), and clustered regularly interspaced short palindromic repeats (CRISPRs). The LacO-Laci-FP and TetO-Teti-FP systems are derived from the lactose and tetracycline operons of *E. coli*, respectively. Lac and Tet repressor proteins, fused to FPs, serve as tracking foci by recognizing repressor tandem repeat sequences inserted next

to the position of interest [79], [80]. Multiple systems and repressor segments can be utilized concurrently within a single cell to increase system multiplicity and fluorescent amplification [81]–[83].

Point accumulation for imaging in nanoscale topography (PAINT) techniques are appealing for localization microscopy due to their lack of photon budget restrictions. DNA-based PAINT [84] has been explored and refined over the past decade. Variants like Quantitative PAINT (qPAINT), Förster resonance energy transfer PAINT (FRET-PAINT) [84], and Exchange PAINT have been developed to generalize the use of DNA origami for revealing cellular interactions. However, any intrusive DNA insertion can potentially disrupt function and alter chromatin locus position and mobility. Non-intrusive methods, such as ZFPs, TALEs, and CRISPR-dCas9, avoid these constraints by operating without artificial DNA insertion [85]–[87]. These systems rely on modular proteins with specific DNA recognition, with endonuclease-deficient proteins typically fused with FPs to serve as detectable signals. Among these strategies, CRISPR imaging systems are gaining considerable attention. Chen et al. re-engineered the type II system to visualize both repetitive elements in telomeres and the non-repetitive MUC4 [88]. For multicolor imaging within the CRISPR system, one strategy involves using fluorescent Cas9 orthologs from different bacterial species simultaneously, such as Streptococcus pyogenes (SpCas9), Neisseria meningitidis (NmCas9), and Streptococcus thermophilus (St1Cas9) [89]. Another strategy involves engineering sgRNA into a scaffold RNA (scRNA) to encode information about the gene of interest and multiple fluorescent reporters [90]. Recent modifications to CRISPR imaging systems, such as CRISPR-display [91] and CRISPR-rainbow [92], indicate promising applications for investigating chromatin organization and visualizing genome instability and rearrangement [85].

#### 4.1.3 Instrumentation for chromatin imaging

Spatial and temporal resolution of nuclear imaging strategies are critical experimental conditions which dominate the reliability of downstream biophysical analysis [93]. Therefore, for most reported work in intranucleus chromatin imaging, objectives with high numerical aperture are employed. For many imaging experiments, an epi-illumination fluorescent mi-

croscope equipped with a modern camera (EMCCD or sCMOS) can provide time-course recording of live cells. Additionally, emerging LED light sources are replacing laser excitation in these microscopes, which significantly reduces the cost of the microscope [94]–[96]. Confocal microscopy is another widely applicable imaging system for chromatin imaging is the confocal microscope, which offers good z-sectioning capability to reduce out-of-focus background. However, the applicability of confocal microscopy for the study of chromatin structure can be limited do to the reduced frame rate [60]. Confocal microscopy suffers from intrinsic limitations such as photo-bleaching/photo-toxicity and poor temporal resolution, which restrict their applications for sensitive chromatin imaging at the single-molecule level.

Light sheet illumination offers solutions to the aforementioned challenges and achieves a balance among spatiotemporal resolution, photo-bleaching effects, and background reduction. The technique has garnered tremendous attention for its advantages in reducing phototoxicity, enhancing sectioning capability, and enabling live-cell three-dimensional (3D) imaging. Early iterations of light sheet microscopy has shown great performance for 3D imaging of tissues, embryos, and organs [97]–[100]. However, its application has been limited by the geometric hindrance of using two objectives. Single objective live sheet methods such as the oblique plane microscope [**Sopoznik2020**], as well as light-sheet analogues which generate a highly inclined and laminated optical sheet (HILO) for single-molecule imaging [101]. An AFM cantilever was initially used to reflect the illumination light sheet by 90 degrees to bypass geometric hindrance [76]. A similar idea was proposed using a microfabricated reflecting chip next to the sample reservoir [102]. Furthermore, the lattice light sheet (LLS) microscope, which generates the light sheet with a Bessel beam, significantly reduces the thickness of the light sheet to 300 nm [103]. The LLS has demonstrated superior performance in terms of spatial resolution, temporal resolution, phototoxicity, and sensitivity [104].

It is worth noting that a significant portion of studies address chromatin structure and dynamics in only two dimensions. While two-dimensional measurements (i.e., positions or trajectories projected in a single plane) are practical and generally well-suited for flat nuclei in monolayer cell cultures, 3D measurements are necessary to improve accuracy, particularly for round nuclei where the relationship between 2D and 3D distances deteriorates, and for

short distances (<5 um) where the average 2D/3D discrepancy is 30 percent [105]. Moreover, nuclear inhomogeneity in all 3 dimensions must be considered. For motion measurements, the 2D/3D discrepancy of 30 percent might not be very significant, but considering local fluctuations of 50 nm, the 3D nature cannot be ignored.

Advances in super-resolution imaging will also benefit intranuclear chromatin imaging. For example, aspherical optics were initially utilized in super-resolution imaging to convert the z-axis position of a single molecule into a distorted point spread function (PSF) on the x-y plane using a cylindrical lens [106]. This method was further developed in single-molecule imaging/tracking to register the 3D position of a moving molecule through a rotational PSF [107]–[110]. Additionally, applying super-resolution imaging to live-cell single-molecule imaging produces high-density trajectories of molecules, enabling the integration of biophysical analysis such as stochastic models of nonequilibrium motions to recover forces, subcellular organizations, diffusion kinetics, and other biophysical features at unprecedented spatiotemporal resolution [111]–[113].

## 4.2 The structure of chromatin nanodomains

Super-resolved nucleosome organization has been studied extensively in fixed cells to reveal segregated nanodomains hundreds of nanometers in size, including dispersed nanodomains and compact large aggregates. Nucleosomes are now known to assemble into heterogeneous clusters of variable sizes, interspersed with nucleosome-depleted regions [9]. However, our current understanding of nucleosome patterning in the nucleus is limited by the need for fixation. Chemical fixation with paraformaldehyde, glutaraldehyde, methanol, or other chemical fixatives may alter the structure of chromatin, introducing error in our measurements [114]. Live cell imaging carries its own issues, particularly due to local and long-range chromatin motions in the nucleus. At the nanoscale, local chromatin motion appears to be isotropic and driven by thermal fluctuation [114]. Therefore, we presume that for sufficiently brief imaging duration (tens of seconds) nanodomain structure is approximately static. As a consequence, vibrations of single nucleosomes are, in effect, an addition of low amplitude noise to the localization dataset.

To perform live cell super-resolution imaging of chromatin nanodomains, we adopt the HaloTag system, a modified haloalkane dehalogenase designed to covalently bind to synthetic ligands (Los 2008). The HaloTag protein is fused to nucleosome H2B and is then bound by a rhodamine-derived fluorescent ligand, JF646 (Grimm 2015). JF646 undergoes fluorescence intermittency (blinking) in the presence of a cysteamine (MEA) containing buffer (Figure 4.1). Once precise positions of the fluorophores are obtained, Besags L-function  $L(r)$  is used to analyze the clustering. The L-function  $L(r) = \sqrt{\frac{K(r)}{\pi}}$  is a transformation of Ripley's K-function  $K(r)$ . The function  $K(r)$  is designed such that  $K(r)$  is the number of localizations within a radius  $r$  of a randomly chosen localization. Importantly, in the case of complete spatial randomness,  $L(r) = r$ . Thus, in general, to quantify the degree of clustering, one uses  $L(r) - r$ , which measures the deviation of a point pattern from CSR. To demonstrate this, example point patterns have been generated under CSR (Figure 4.2) and a Thomas point process (Figure 4.3).

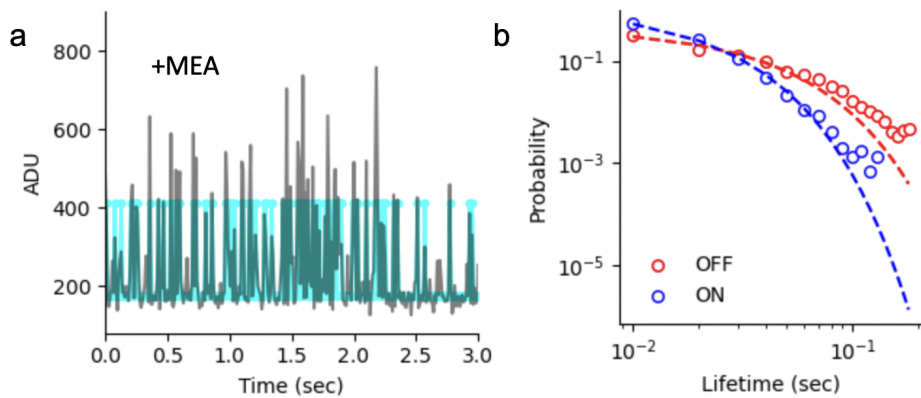


**Figure 4.1. Photoswitching of JF646 bound to H2B-HaloTag.** (a) Peak intensity fluctuations of a putatively isolated JF646 molecule excited at 640nm and imaged with 10ms exposure time in the presence of 100mM MEA buffer. Fit of a Poisson HMM is shown in cyan (b) ON and OFF state lifetime distributions found by pooling data from 16 JF646 spots in a single HeLa cell nucleus. Single component exponential fits shown as solid lines.

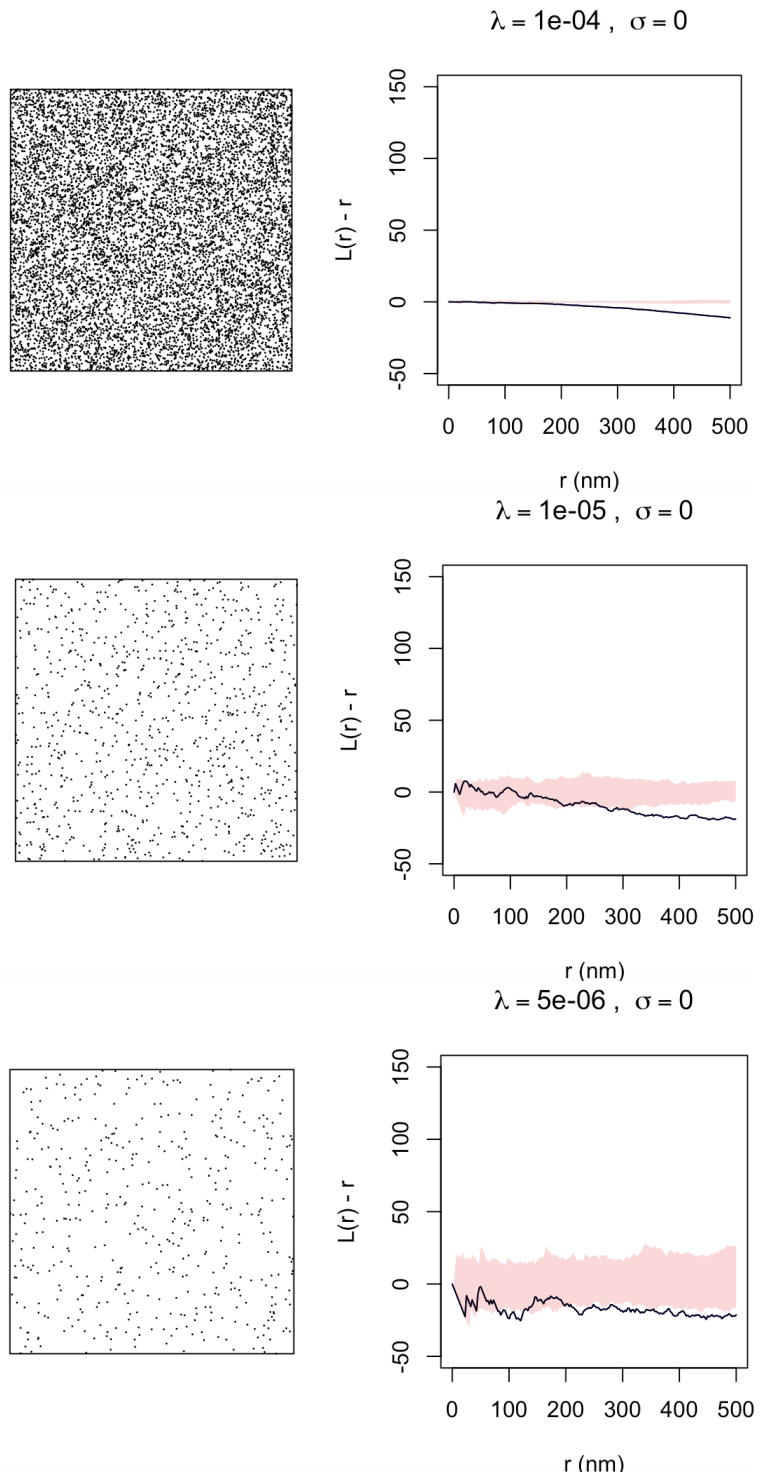


**Figure 4.2. Besag's L-function under complete spatial randomness.**  
 Point pattern simulations for complete spatial randomness ( $\sigma = 0$ ) for various intensities of the point process. Simulation envelopes are shown in pink, which represent the significance band of the estimated  $L(r) - r$

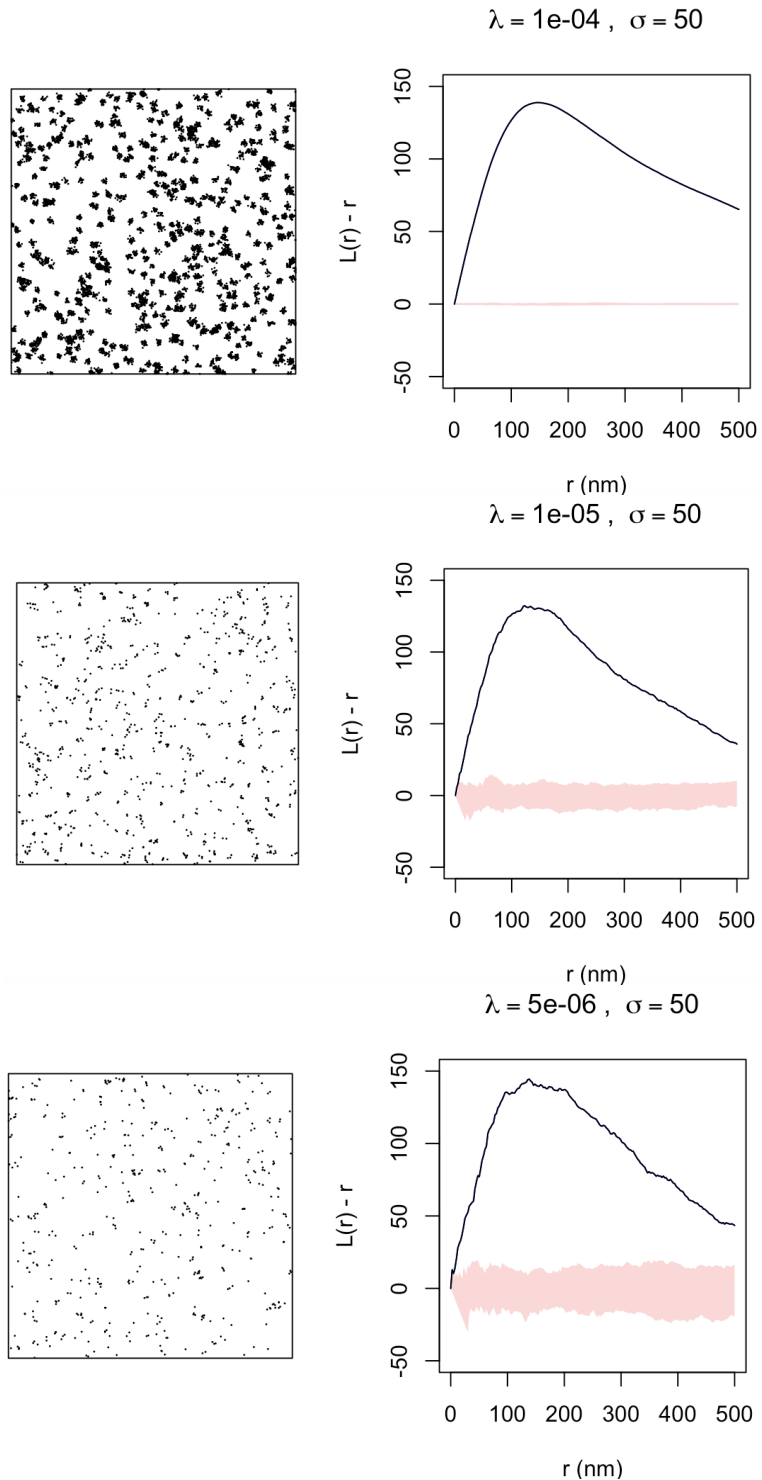


**Figure 4.3. Besag's L-function for a Thomas process.** Point pattern simulations for the Thomas process ( $\sigma = 50\text{nm}$ ) for various intensities of the point process. Simulation envelopes are shown in pink, which represent the significance band of the estimated  $L(r) - r$

### 4.3 Polymer models and chromatin dynamics

By accumulating single molecule localizations over a time series of frames, quantitative information regarding the motion of the particle can be extracted and related to experimental conditions. It is important to note that the chromatin structure is highly complex and cannot be exactly represented by the diffusion of individual particles. However, by treating each fluorescent spot as a point mapped in space and time, we can extract parameters of the diffusion and classify tracks as sub-diffusive, Brownian, or super diffusive.

The well-known diffusion equation is a special case of the more general Kramers-Moyal expansion, which describes the dynamics of the probability density of a stochastic process  $P(x, t)$ . Pure diffusion is the case where transitions in the process are drawn from a distribution with zero mean (zero drift) and constant variance.

$$\frac{\partial P(x, t)}{\partial t} = D \frac{\partial^2 P(x, t)}{\partial x^2} \quad (4.1)$$

The diffusion coefficient  $D$  is in fact just half of the variance of the transition distribution  $D = \sigma^2/2$ . We would like to solve the above equation, but it is a PDE which usually require some tricks to solve e.g., integral transforms. This particular PDE can be solved by Fourier transformation. For brevity, I simply state the result

$$P(x, t) = \frac{1}{\sqrt{2Dt}} \exp\left(-\frac{(x - x_0)^2}{4Dt}\right)$$

which is a Gaussian distribution with time-dependent variance  $\sigma = \sqrt{4Dt}$ , given originally by Einstein in his famous paper on Brownian motion in 1905. The most common method to analyze single particle trajectories is to calculate the mean square displacement (MSD), which can be used to determine the diffusion coefficient  $D$ .

$$\text{MSD} = \frac{1}{N} \sum_{i=1}^N [\mathbf{r}(t + \tau) - \mathbf{r}(t)]^2 \quad (4.2)$$

The sampling time given by  $\tau$  is interpreted as the frame rate of the camera. Certain studies have shown that the observed motion varies with different values of  $\tau$  [Shukron2017a, 115]. It is not difficult to see that the solution to the diffusion equation has a linear MSD:  $MSD(\tau) = 4Dt$ . A linear MSD is therefore a defining characteristic of Brownian motion. Sub-diffusive and super-diffusive diffusion can be classified by use of the more general anomalous diffusion model:

$$MSD(\tau) = 2mD\tau^\alpha \quad (4.3)$$

where  $m$  is the number of dimensions. For trajectories with  $\alpha = 1$ , the motion is considered to be Brownian motion; when  $\alpha > 1$ , it is said to be directed motion; and  $\alpha < 1$  is classified as confined (or immobilized) diffusion. Importantly, different parameter values allow for further interpretation and classification of different diffusion modes of particles [116], [117].

By comparing the  $D$  values of all particles within the nucleus, spatial heterogeneity can be clarified. While the calculation of  $D$  and  $\alpha$  is particularly reliant on the length of the trajectory and the number of data points, recent investigations have built diffusion color maps of fluorescently labeled histones by computing vast amounts of super-resolution trajectories [10], [115], [118].

#### 4.3.1 Trajectory linking

A diverse set of particle tracking algorithms utilize probabilistic models of particle motion in order to add detected particles to existing tracks. Perhaps the most fundamental particle tracking method in this category is the nearest neighbor (NN) linking algorithm first introduced by Crocker and Grier. The algorithm constructs particle trajectories by assuming that the ensemble consists of non-interacting indistinguishable particles undergoing Brownian motion. As a result, the displacement of each particle follows a Gaussian distribution, parameterized by the diffusion coefficient and the time-resolution of the sequence. The most probable assignment of detected particles to existing tracks can then be found by maximizing the product of several Gaussian distributions [119]. An attractive feature of this

algorithm is that it is relatively simple to implement; however, assumptions that underlie the method impose limitations. In particular, if a typical displacement  $\delta$  in one time step is comparable to the typical inter-particle spacing, tracking becomes highly error-prone [119]. In other words, when particles are simultaneously densely distributed and undergoing fast diffusion, the algorithm can fail to build accurate trajectories due to the ambiguity introduced by overlapping trajectories. This also applies to the limit of low frame rates when small displacements are not recorded by the sensor. Importantly, the method alone cannot handle cases where particles disappear permanently, temporarily disappear due to blinking, photo-bleaching, or missed localization [120].

#### 4.3.2 Chromatin polymer models

It is well-known that the DNA double helix structure consists of millions of base pairs chained together by the sugar-phosphate backbone. DNA, being a molecule built from many similar monomers bonded together, is naturally analyzed using a polymer model. The simplest polymer model for chromatin is the Rouse polymer model, which discretizes it into monomers connected by springs, resembling the string-of-beads structure observed under the electron microscope. Various forces acting on chromatin result in constrained dynamics, leading to significant variability in the anomalous exponent  $\alpha$  for the dynamics of a chromatin locus.

To refine the modeling of chromatin properties according to the exponent  $\alpha$ , the  $\beta$ -polymer model was introduced. This model accounts for mid-range and long-range interactions between monomers, not just those between the nearest neighbors as in the Rouse polymer model. In this model,  $\alpha$  shows a decay curve with distance along the chain. While  $\alpha \sim 0.5$  in the traditional Rouse polymer model (Figure 4.4, 4.5, 4.6), the  $\beta$ -polymer model can be selected to address cases where  $\alpha$  is in the range of 0 to 0.5 [115], [121], [122]. Thus, local interactions between monomers can be inferred from the anomalous diffusion exponent using this construction.

Furthermore, as the polymer model usually folds at different spatial scales and generates various sizes of loops, a simulation model adding connectors between randomly chosen non-

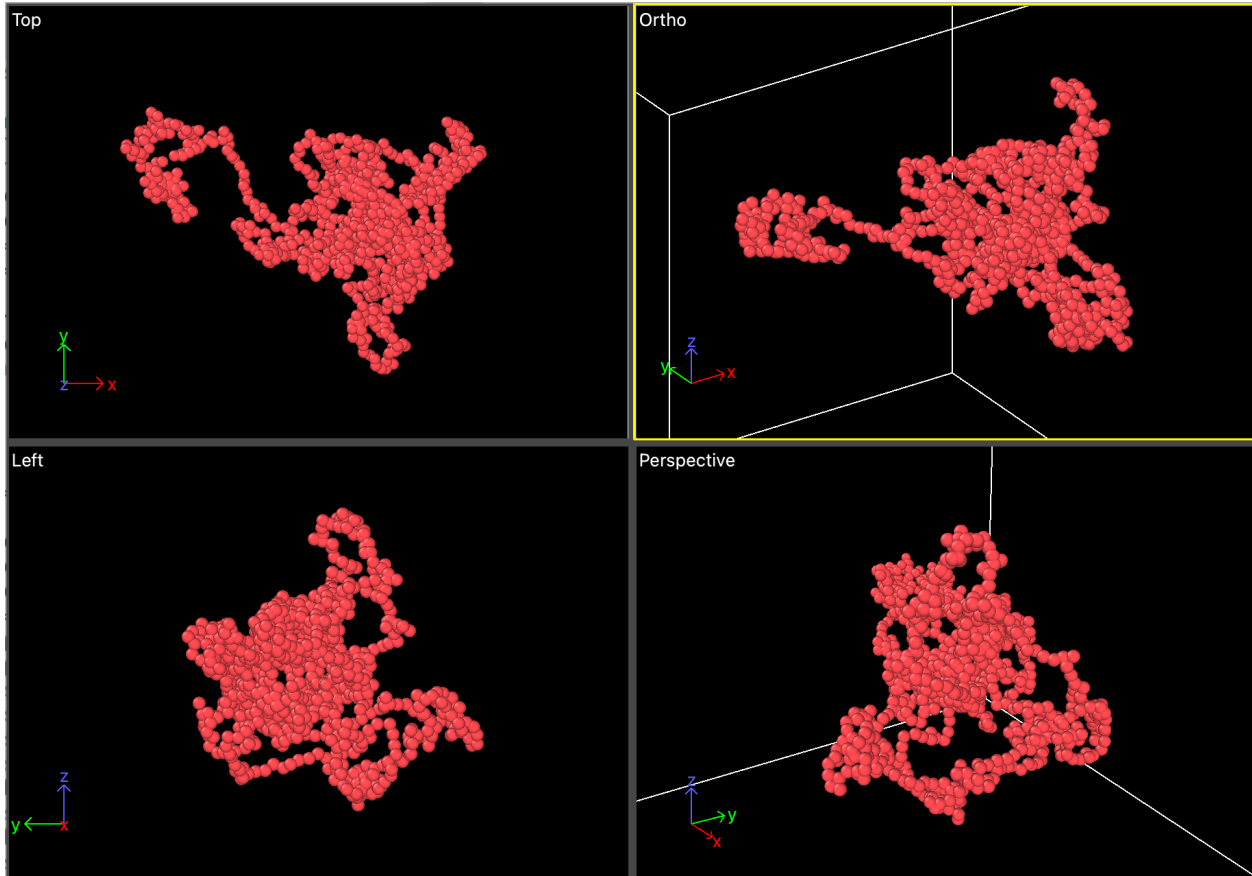


**Figure 4.4.** Snapshots of the Rouse polymer. Four perspectives of the Rouse polymer generated with  $N = 2000$  beads connected with harmonic bonds with equilibrium length 200nm. Polymer is initialized with all harmonic bonds at equilibrium

Parameter	Value
Temperature ( $T$ )	310 K
Bond Length ( $\sigma$ )	$200 \times 10^{-9}$ m
Cutoff Distance	$500 \times 10^{-9}$ m
Spring Constant ( $\kappa$ )	$90.0 k_B T / \sigma^2$
Neighbor Distance	$500 \times 10^{-9}$ m
Damping Coefficient ( $\gamma$ )	$10^{-4}$
Time Step	1s
Number of Time Steps	$10^4$
Number of Atoms	2000

**Table 4.1.** Rouse polymer parameters

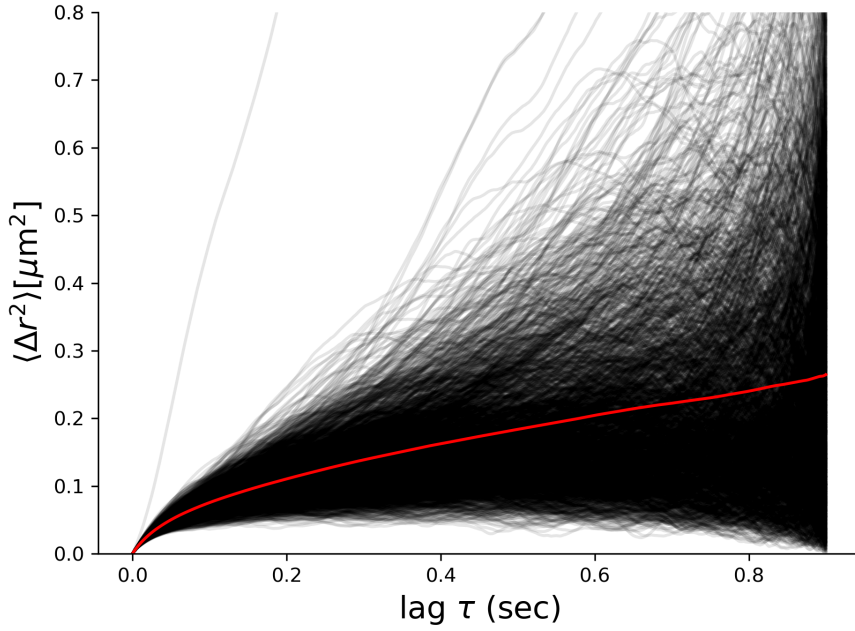


**Figure 4.5. Subdiffusive dynamics of a Rouse polymer.** Mean squared displacement (MSD) of 2k beads shown in black, average MSD shown in red.

nearest neighbor monomer pairs, known as the randomly cross-linked (RCL) polymer model, was presented. In this model,  $\alpha$  is reduced to below 0.5 by adding connectors. Recent evidence suggests that the number and distribution of connectors impact physical parameters in various ways, but this domain remains underexplored. Notably, the RCL polymer model may be crucial for studying dynamics in processes such as CTCF and cohesion regulating chromatin loop stability [123]. Additionally, sub-diffusion with an exponent  $\alpha > 0.5$  can occur in some polymer models, potentially involving different types of forces such as deterministic forces, directed motion, or other monomer interactions (self-avoiding and bending interactions).

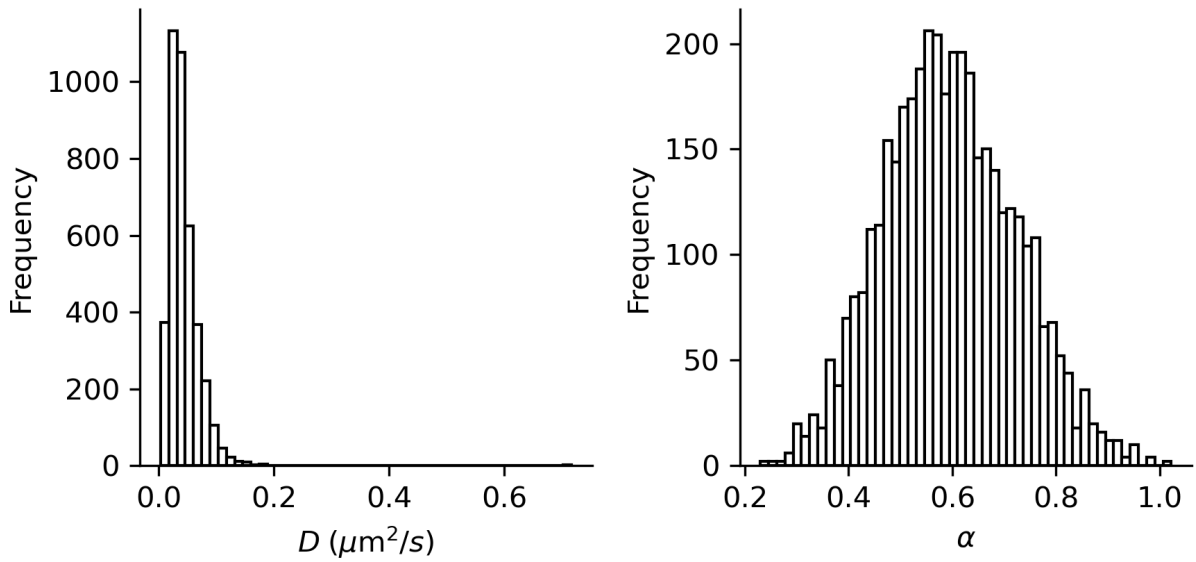


**Figure 4.6. Subdiffusive dynamics of the Rouse polymer.** (left) Histogram of the diffusion coefficient of individual beads. (right) Histogram of the anomalous exponent. Fitting of individual bead MSDs performed by linear regression in log-space using the first 5000 time points

#### 4.4 BRD4 regulates the structure of chromatin nanodomains

The cell nucleus is a densely packed environment with chromatin comprising a dominant component. The compartmentalization of chromatin with other intranuclear components by phase separation is therefore an efficient strategy to ensure precise spatial and temporal coordination of complex dynamics. A growing number of phase separated nuclear bodies have been identified, including transcriptional condensates [124], [125], nuclear speckles [126], and DNA damage repair foci [8]; however, the interplay of phase separated condensates with the underlying chromatin structure remains poorly understood. Transcriptional condensates have been identified as an ideal model to study the kinetic and thermodynamic contributions of chromatin substrate binding, as the ability of transcriptional activators to both condense and bind chromatin is well established [124], [127]–[130]. Here, we extend this effort by investigating the regulation of chromatin structure by phase separated transcriptional condensates. We focus on the BRD4 protein - a well-studied transcriptional activator that localizes to acetylated chromatin sites [131], recruits pTEF-b, and initiates transcription of key genes involved in signal response, immunity, and oncogenesis [132].

The BRD4 long isoform is characterized by structured N-terminal tandem acetyl-lysine binding bromodomains and an extra-terminal domain, connected by intrinsically disordered regions [133]. Perhaps the most fundamental of BRD4 functions is the ability to bind to acetylated chromatin through bromodomain 1 (BD1) and bromodomain 2 (BD2) that are in tandem within the N-terminal part of the protein (Figure 4.7). BRD4 inhibitors such as (+)-JQ1 competitively bind to the acetyl-binding pocket of BRD4, displacing BRD4 from chromatin [134]. It is also well known that BRD4 association with acetylated chromatin is enhanced by casein kinase II (CK2)-mediated phosphorylation of seven N-terminus phosphorylation sites (NPS), followed by intramolecular rearrangement of BRD4 protein and/or BRD4 dimerization [135], [136].

Recent studies have demonstrated that BRD4 is present in discrete nuclear bodies that occur at super-enhancers, which exhibit properties of other well-studied biomolecular condensates, including rapid recovery of fluorescence after photobleaching and sensitivity to 1,6-hexanediol, which disrupts liquid-like condensates [124]. Both BRD4 long and short iso-

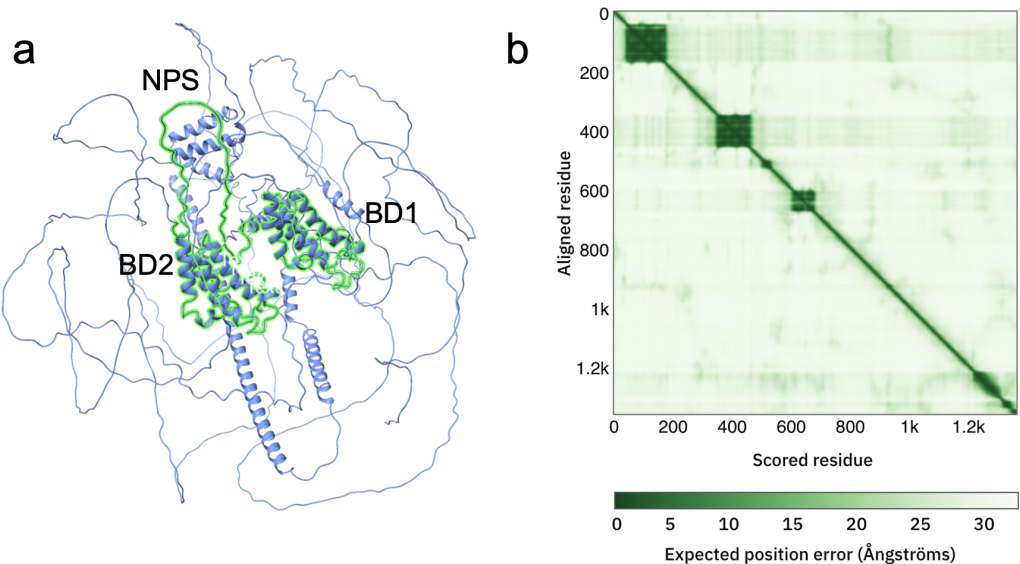


**Figure 4.7. Bromodomain protein 4 (BRD4) structure prediction.**  
 (a) AlphaFold predicted structure of BRD4 long isoform (blue) with bromodomain 1 (BD1) aa58-163, bromodomain 2 (BD2) aa349-456, and N-terminus phosphorylation sites (NPS) aa462-506 highlighted in green. (b) Heat map of expected position error in AlphaFold prediction

form are found in phase separated condensates in the nucleus and are associated with active gene transcription<sup>1</sup>. Importantly, CK2-mediated NPS phosphorylation state regulates chromatin binding activity of BRD4<sup>13</sup> as well as BRD4 phase separation [133]. This has led to the conclusion that phosphorylation of BRD4 inhibits interaction with chromatin and reduces phase separation, while remaining necessary for active gene transcription. Moreover, phosphorylated and unphosphorylated BRD4 form different molecular associations transient polyvalent associations of unphosphorylated BRD4 contrast with the stable dimeric interaction and chromatin binding of phosphorylated BRD4 [136]. We therefore speculated that BRD4 chromatin binding may be necessary for maintaining NN structure and single nucleosome dynamics.

#### 4.4.1 Results

##### Colocalization of BRD4 mutants with nucleosome nanodomains

To address the role of BRD4 binding and phase separation on chromatin structure, we express FLAG-tagged BRD4 mutants with NPS or bromodomain mutations in HeLa cells and measure their effects on chromatin organization. In particular, we express a constitutively phosphorylated (7D mutant), constitutively unphosphorylated (7A mutant), and bromodomain-deactivated (BD mutant) protein (Figure 4.8 a,b,c). Colocalization analysis of BRD4 mutants with NNs using nearest neighbor distance distribution showed an obvious colocalization of these mutants with NNs. The 7D mutant showed the closest proximity to NNs relative to wild type, followed by BD and 7A mutants (Figure 4.8 d). This result is consistent with known dependence of BRD4 chromatin binding on phosphorylation state.

##### Chromatin structure and dynamics

To assess the functional role of BRD4 in maintaining the NN environment, we interrogated the dynamics of NNs, as well as their structure, in the presence of BRD4 mutants. Histone H2B was tagged with HaloTag [137] (H2B-Halo), to which a fluorescent ligand JaneliaFluor646 (JF646) can bind specifically in a living cell. Low concentrations of JF646 were used to obtain sparse labeling of nucleosomes for single-nucleosome imaging (Figure 4.11 a,b). JF646-labeled nucleosomes in HeLa cells were recorded at 10fps (200 frames, 20 s total) and a reduced diffusion coefficient was measured in cells expressing 7A, 7D, and BD mutants, with respect to cells expressing the wild-type BRD4 protein (Figure 4.11 c). HeLa cells exposed to (+)-JQ1 in DMSO for 8h showed an increase in nucleosome dynamics with respect to DMSO alone (Figure 4.11 d). We then conducted super resolution imaging of nucleosome nanodomains using direct stochastic optical reconstruction microscopy (dSTORM) by promoting JF646 fluorescence intermittency with a cysteamine buffer (Figure 4.10 a,b). JF646 is known to exhibit a transient fluorescent state lasting tens to hundreds of milliseconds and stable dark state lasting hundreds of milliseconds to seconds [138]. Two color imaging of H2B-Halo-JF646 and GFP-tagged BRD4 shows that BRD4 and NNs form complementary

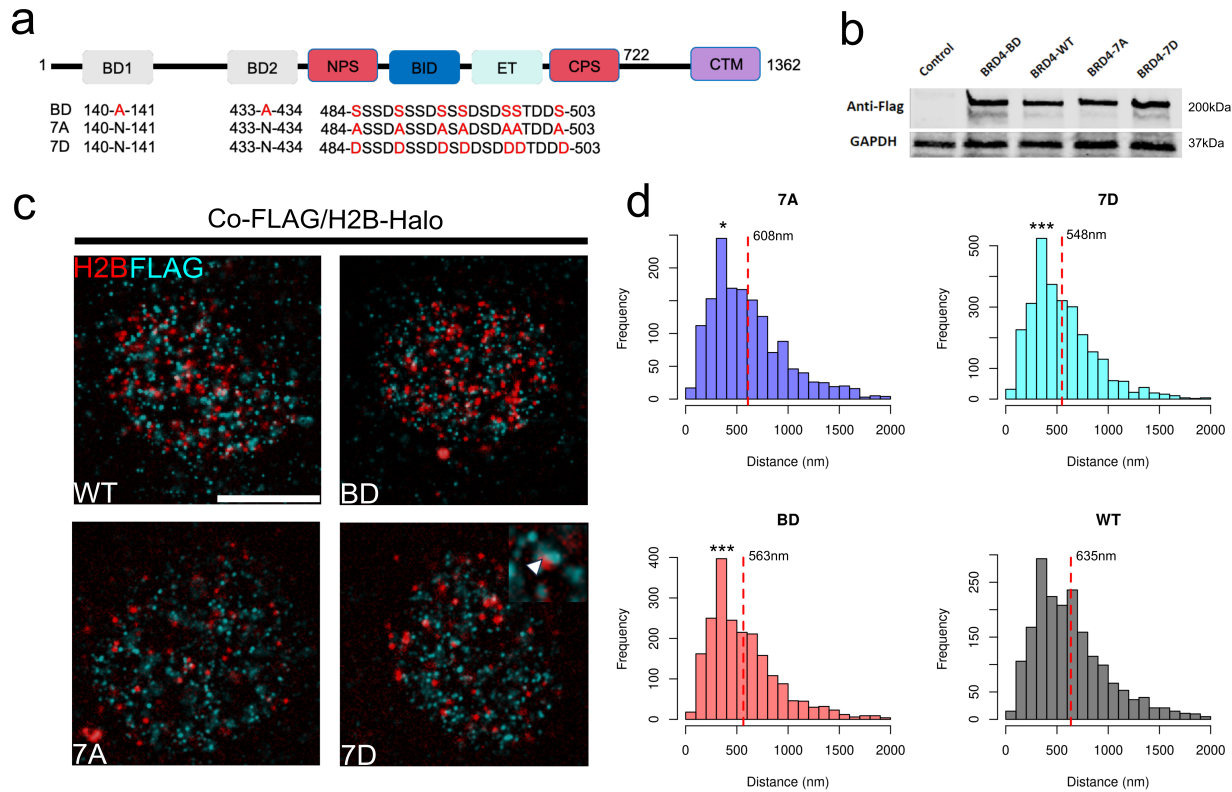


**Figure 4.8. BRD4 mutants colocalize with nucleosome nanodomains.**  
 (a) Schematic of the BRD4 protein sequence and mutations shown in red. (b) Anti-FLAG western blot of bulk expression of BRD4 mutants. (c) Combined immunofluorescence of FLAG-tagged BRD4 mutants with JF646-tagged H2B-Halo. (d) Histograms of nearest neighbor distances of H2B puncta to FLAG puncta over N=10 cells for each mutant. Red dashed lines are drawn at the mean, statistical significance determined by Welch t-test for each mutant relative to wild-type (\* p<0.05, \*\*\* p<0.001)

biomolecular condensates in the nucleus, consistent with current models of BRD4 chromatin reading mechanism (Figure 4.10 c). Ensemble averages of Besags L-function showed an increase in nucleosome clustering in cells expressing the 7D BRD4 mutants, while all other groups were consistently indistinguishable from WT cells (Figure 4.10 e). HeLa cells exposed to (+)-JQ1 in DMSO for 8h showed a reduction in nucleosome clustering with respect to DMSO alone (Figure 4.10 f).

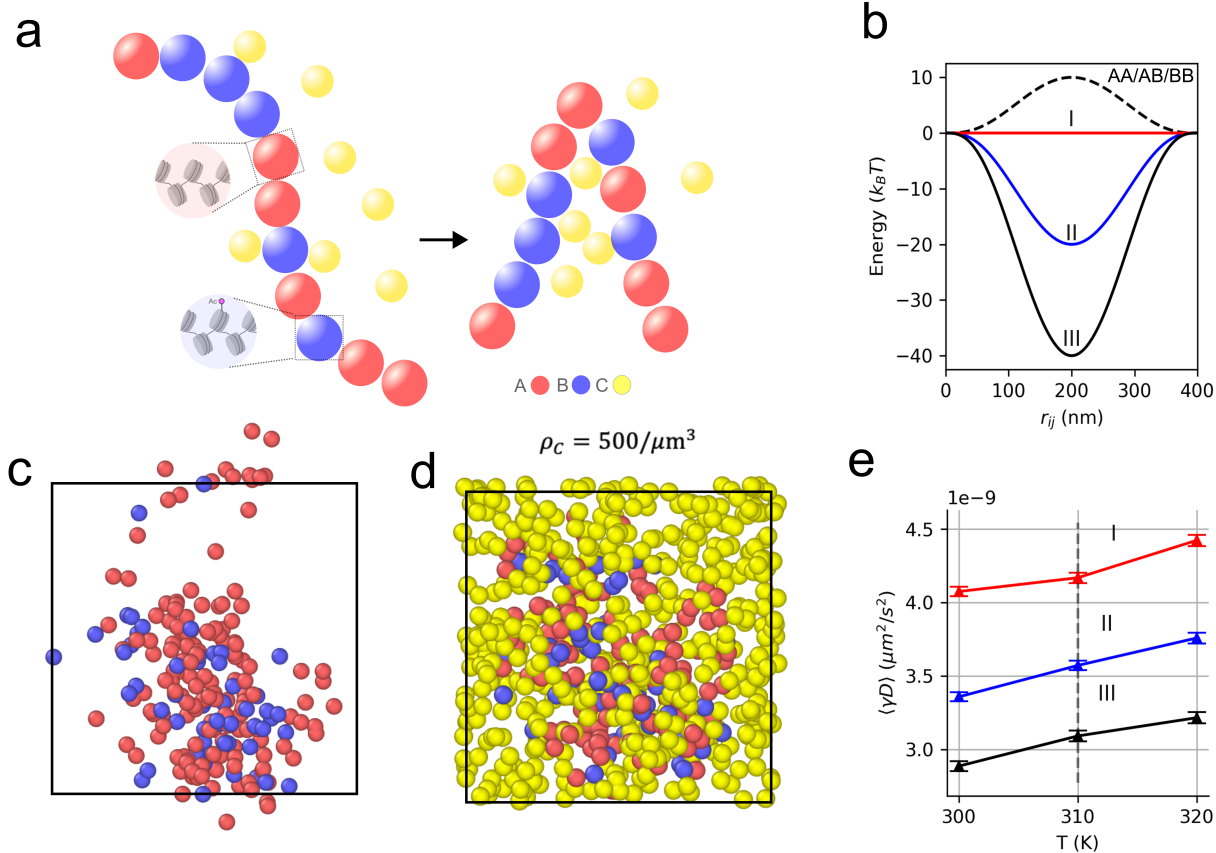


**Figure 4.9. Strong multivalent chromatin binders reduce diffusion of nucleosome nanodomains.** (a) Heteropolymer model of chromatin consisting of A-type, B-type, and C-type particles. (b) Interaction potentials  $U_{BC}(r_{ij})$  of multivalent chromatin binders with B-type chromatin beads. (c,d) Example free heteropolymer and heteropolymer with a number density of C-type particles of  $\rho = 500/\mu\text{m}^3$  in a 10um periodic box. (e) Scaled diffusion coefficient  $D$  for various chromatin binding energies of C-type particles, averaged over ten independent simulations, with burn-in discarded.

### Heteropolymer model

To interpret our experimental findings, we adopt a heteropolymer chromatin model to capture the interaction of chromatin with multivalent BRD4-like binders (Figure 4.9 a). The heteropolymer consists of a coarse-grained bead-and-spring chain composed of  $N_b = 200$  beads, connected by harmonic bonds with equilibrium length  $r_0$  whose energy is dened as

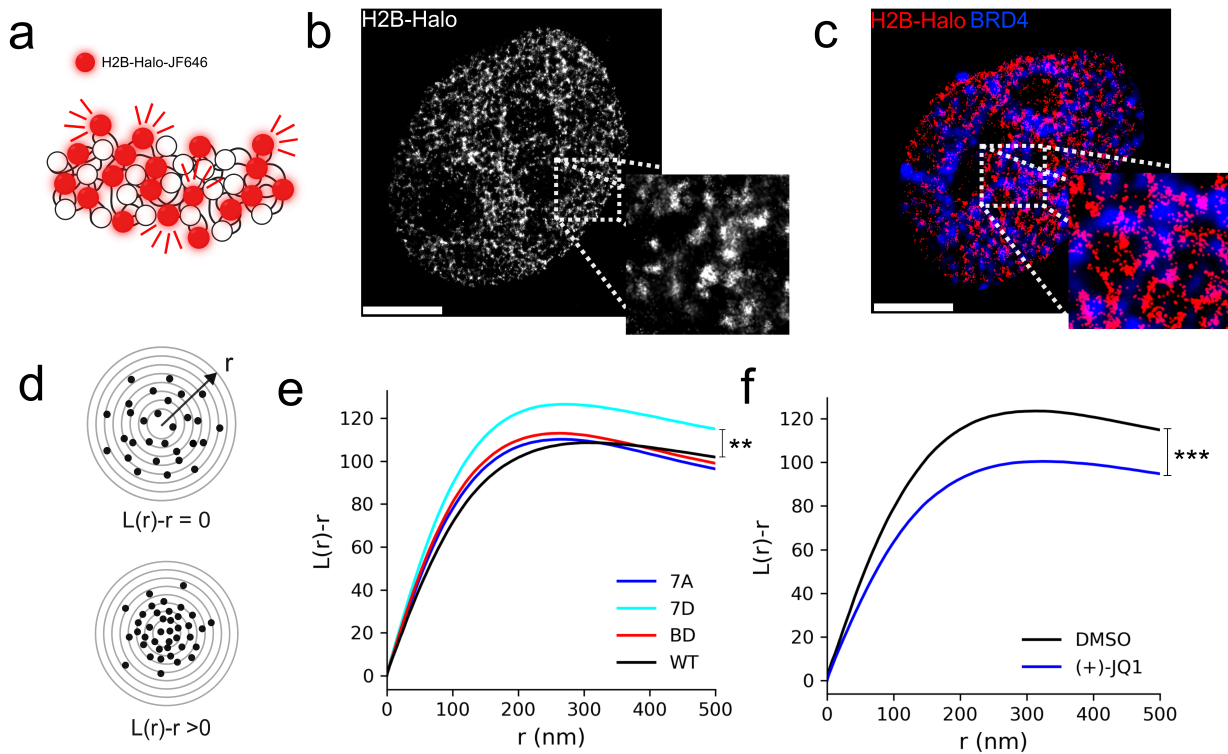


**Figure 4.10. Expression of constitutively phosphorylated BRD4 compacts nucleosome nanodomains.** (a,b) Direct stochastic optical reconstruction microscopy (dSTORM) imaging strategy of single nucleosomes and an example super-resolution image. (c) Two-color image of super-resolved H2B-JF646 with diffraction-limited GFP-tagged BRD4. (d) Quantification of degree of clustering using the L-function (e) L-function for BRD4 mutants. (f) L-function after 8h exposure to 1uM (+)-JQ1 in DMSO and DMSO only. All scalebars 3um. \*\* p<0.01, \*\*\* p<0.001

$$U_{AB}(r_{ij}) = \frac{\kappa}{2}(|r_{ij}| - r_0)^2$$

where  $r_{ij}$  is a vector connecting the center of a bead of type i to a bead of type j and  $i, j \in (A, B)$ . In all simulations, we assume  $\kappa = 90k_B T r_0^2$  where  $k_B$  is Boltzmanns constant and  $r_0 = 200\text{nm}$ . Random beads in the chain are selected to represent locally unacetylated (A-type particles) and acetylated chromatin (B-type particles). B-type particles undergo multivalent interactions with a third group of C-type particles, which can promote cross-linking of the polymer. We presume a Bernoulli probably of  $p = 0.3$  for any given bead to

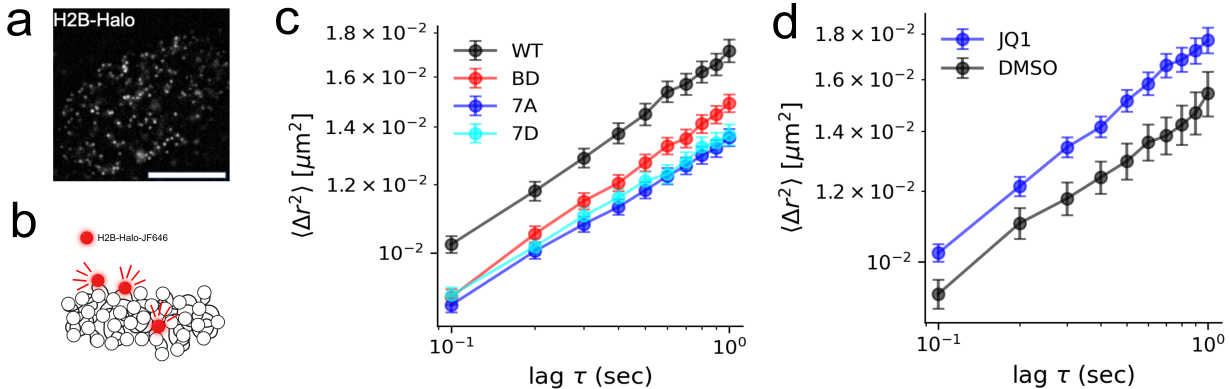


**Figure 4.11. BRD4 mutants reduce single nucleosome dynamics in living cells.**(a,b) Sparse labeling of single nucleosomes in a living HeLa cell (scalebar 5um). (c) Average mean squared displacement (MSD) of single nucleosomes for wild-type and mutated BRD4, error bars represent the standard error of the mean. (d) Average MSD of single nucleosomes after 8h exposure to 1uM (+)-JQ1 in DMSO and DMSO only, error bars represent the standard error of the mean

be in an acetylated-like state. Interaction of multivalent chromatin binders with chromatin beads are then mediated by the following potential:

$$U_{BC}(r_{ij}) = \epsilon \left( 1 - \left( \frac{|r_{ij}|}{R_0} \right)^2 \right)^3$$

where  $R_0 = 200\text{nm}$ . The potential  $U_{BC}$  is considered over a domain  $0 \leq |r_{ij}| \leq 2R_0$ . In all simulations, ten replicates were run for each condition tested. A and B type particles within the chromatin polymer have repulsive interactions with  $\epsilon = +10k_BT$ . Binding energy of the acetylated beads with binders was varied with  $\epsilon_I = 0k_BT, \epsilon_{II} = -20k_BT, \epsilon_{III} = -40k_BT$  (Figure 4.9 a). The dynamics of chromatin chains are approximated by Brownian dynamics within a cubic box with side length of 10um and periodic boundary conditions. Brownian dynamics follows the stochastic differential equation.

$$\dot{\mathbf{r}} = \gamma^{-1} \nabla U(\mathbf{r}) + \sqrt{2k_BT} \gamma^{-1/2} \xi(t)$$

Parameter	Value
Bond Length ( $\sigma$ )	$200 \times 10^{-9}$ m
Cutoff Distance	$500 \times 10^{-9}$ m
Spring Constant ( $\kappa$ )	$90.0 k_B T / \sigma^2$
Neighbor Distance	$500 \times 10^{-9}$ m
Damping Coefficient ( $\gamma$ )	$10^{-7}$
Time Step	$10^{-4}$ s
Number of Time Steps	$10^4$
Number of Atoms	200

**Table 4.2. Multivalent binder model parameters**

where  $\gamma$  is a diagonal friction tensor and  $\xi(t)$  is a three-dimensional delta-correlated white noise  $\langle \xi(t) \xi(t + \tau) \rangle = \delta(t, t + \tau)$ . Integrating the Brownian dynamics showed an overall reduction of the variance of the diffusion coefficient  $D$  of single beads, and linear scaling of the diffusion coefficient with respect to temperature (Figure 4.9 e).

#### 4.4.2 Discussion

Our data support the model that phosphorylated and unphosphorylated BRD4 form different molecular associations in the nucleus. BRD4 nuclear localization is only weakly affected by bromodomain inhibition with monovalent BET inhibitors, while exposure to phase separation inhibitors such as 1,6 Hexanediol have a significant effect on BRD4 localization in the nucleus<sup>11</sup>. Colocalization activity of 7A/7D mutants relative to wild type measured here is consistent with this model of BRD4 localization to nucleosome nanodomains. Strong colocalization of the BD mutant relative to the wild type suggests a possible link between bromodomain structure with localization of BRD4.

Concurrently, reduced diffusivity of single nucleosomes with all mutants tested suggests a relationship between elevated colocalization and the degree of confinement of nanodomain diffusion. At the same time, increased nucleosome diffusivity and reduced nucleosome clustering after (+)-JQ1 exposure indicate BRD4 condensate formation is necessary in maintaining the nanodomain architecture. We further hypothesize effects of BRD4 localization on the viscosity of the nanodomain environment and potentially increased cross-linking of nan-

odomains. Indeed, we find this to be a natural result of molecular crowding resulting from overexpression of a constitutively phase separating protein, capable of multivalent interactions. Substantial colocalization of the 7D mutant with nanodomains along with increased chromatin compaction points towards a BRD4-mediated cross-linking mechanism of nucleosomes within the nanodomain. This result of increased affinity can also be seen in coarse grained simulations of chromatin interactions with multivalent binders.

We conclude that nascent BRD4 condensates are likely seeded by promiscuous interactions of BRD4 with cofactors, followed by phosphorylation followed by chromatin interactions mediated by the phosphorylated form. The stable dimeric interaction and binding of phosphorylated BRD4 to acetylated chromatin would then mediate control of the chromatin architecture by promoting cross-linking of the chromatin fiber and acting a molecular bridge between transcriptional condensates with chromatin.

#### 4.4.3 Materials and Methods

##### Cell lines, cell culture conditions, and transfection

HeLa cells were cultured in DMEM supplemented with 10 percent fetal bovine serum (Gibco) at 37C 5 percent CO<sub>2</sub> in a humidified incubator. Cultures were tested routinely for mycoplasma contamination; all tests were negative. For super-resolution experiments, cells were seeded in a 35mm FluoroDish (WPI), and transiently transfected using Lipofectamine 3000 with pBREBACK-H2BHalo plasmid (Addgene plasmid 91564) (ThermoFisher), pcDNA5-Flag-BRD4-7A (Addgene Plasmid 90006), pcDNA5-Flag-BRD4-7D (Addgene Plasmid 90007), pCDNA5-Flag-BRD4-BD (Addgene Plasmid 90005), pcDNA5-Flag-BRD4-WT (Addgene Plasmid 90331)

##### Super-resolution imaging of nucleosome nanodomains in living cells

After transient transfection, H2B-Halotag HeLa cells were incubated with 3pM JF646 HaloTag ligand overnight. Cells were imaged in a dSTORM photoswitching buffer containing 100mM MEA, 50 ug/ml Glucose Oxidase, and 3.4 mg/ml Catalase (Sigma). Buffer pH was adjusted to 8 using HCl. Movies were collected using a custom Olympus IX83 microscope

body equipped with an Olympus 60X 1.25NA oil-immersion objective. During imaging cells were maintained at 37C and 5 percent CO<sub>2</sub> in a stage top incubator (Tokai Hit). Images were projected onto an ORCA-Fusion sCMOS camera (Hamamatsu) and 2000 frames were captured at 100fps. The microscope was controlled using Micromanager software. HaloTag-JF646 molecules were imaged using oblique illumination with a 640nm laser (Excelitas) held at 20mW, as measured at the back focal plane of the objective. Super resolution reconstructions were obtained using the ThunderSTORM ImageJ plugin. Background signal was subtracted using a rolling ball filter with radius of 10 pixels. Spots were fit using an integrated Gaussian point spread function model with maximum likelihood estimation [15], [17]. Experimental conditions for single molecule tracking are nearly identical. However, H2B-Halotag HeLa cells were incubated with 3pM JF646 HaloTag ligand. HaloTag-JF646 molecules were illuminated at 10mW, 100 frames were captured at 10fps.

### Colocalization of BRD4 mutants with nucleosome nanodomains

We colocalize FLAG-tagged BRD4 mutants with nucleosome nanodomains by simultaneous FLAG immunofluorescence with imaging of sparsely labeled of H2B-JF646. Puncta were detected in both channels using the Laplacian of Gaussian (LoG) detection algorithm to generate a multi-type point pattern. We then computed the nearest neighbor distance distribution as the distance from a random H2B-JF646 puncta to the nearest BRD4-FLAG puncta. Nearest distances values were pooled over N=10 cells for each mutant.

### Single molecule tracking

Nucleosomes were localized using an integrated Gaussian point spread function model with maximum likelihood estimation [15], [17] and tracked using TrackPy Python software. Trajectories lasting less than 80 frames were removed from further analysis. The individual mean squared displacement (MSD) is computed as  $\langle \Delta r^2 \rangle = \frac{1}{|S_\tau|} \sum_{\Delta r \in S_\tau} (\Delta r)^2$  where  $S_\tau$  is the set of all displacements in a time interval  $\tau$ . The diffusion coefficient for both simulations as well as experimental data was computed by linear regression of the formula  $\log \langle \Delta r^2 \rangle = \log 4D + \alpha \log \tau$

## **Immunofluorescence**

Cells grown in 35mm dishes were fixed with Formaldehyde in 1xPBS at 37C incubator for 20 minutes, and then permeabilized with 0.3 percent (v/v) Triton-X100 (Sigma-Aldrich) in PBS and blocked for 1h in 5 percent (w/v) nonfat dry milk at 4C. Cells were incubated overnight at 4C using primary antibodies anti-FLAG (Cell Signaling, clone XXX; 1:1000), and anti-BRD4 (Cell Signaling, clone E2A7X; 1:1000) in blocker. Secondary antibodies for BRD4 (Cell Signaling Anti-Mouse IgG-Alexa488, 1:1000) were used.

## **Immunoblotting**

Cells were washed and lysis buffer added (RIPA buffer: PMSF: protease inhibitor cocktail: orthovanadate=100:1:2:1). Cells were then scraped and sonicated for 15 seconds using an ultrasonic homogenizer. Lysate was centrifuged at high speed (13200r/min) for 15 minutes at 4C to pellet the cellular debris. Total protein concentration was determined by a BCA Protein Assay Kit (Pierce). For electrophoresis, protein samples were prepared according to a protein-4x loading buffer (containing DTT) ratio of 3:1, 4x loading buffer containing DTT was diluted with 3 aliquots of protein sample. The sample was mixed and heated at 95C for 5 min, followed by vortex and centrifuge. After running the gel, it was removed from the cassette and assembled inside the Trans-Blot Turbo Transfer System cassette. Transfer was run at 2.5A and 25V for 7mins. The sample was then blocked for at least 1 hour using 5 percent skim milk blocking solution prepared with PBS in RT. Primary FLAG antibody was diluted in PBST with 3 percent skim milk (1:500) and incubated at 4C overnight. The secondary antibody (Licor Anti-Mouse IgG- IRDye 800CW) was diluted in PBST with 3 percent skim milk (1:5000) and placed on a rocker and incubated at RT for 45min. Western blots on Nitrocellulose membranes were scanned using the Odyssey fluorescence scanning system software.

## REFERENCES

- [1] C. Seitz and J. Liu, “Quantum enhanced localization microscopy with a single photon avalanche diode array,” *In Review*, 2024.
- [2] C. Seitz and J. Liu, “Uncertainty-aware localization microscopy by variational diffusion,” *In Review*, 2024.
- [3] C. Seitz, D. Fu, M. Liu, H. Ma, and J. Liu, “Brd4 phosphorylation regulates the structure of chromatin nanodomains,” *In Review*, 2024.
- [4] H. Kong *et al.*, “A generalized laplacian of gaussian filter for blob detection and its applications,” *IEEE Transactions on Cybernetics*, vol. 43, pp. 1719–1733, 2013.
- [5] B. F. Lillemeier, M. A. Mörtelmaier, M. B. Forstner, J. B. Huppa, J. T. Groves, and M. M. Davis, “Tcr and lat are expressed on separate protein islands on t cell membranes and concatenate during activation,” *Nature Immunology*, vol. 11, pp. 90–96, 1 Jan. 2010, ISSN: 15292908. DOI: [10.1038/ni.1832](https://doi.org/10.1038/ni.1832).
- [6] J. Rossy, D. M. Owen, D. J. Williamson, Z. Yang, and K. Gaus, “Conformational states of the kinase lck regulate clustering in early t cell signaling,” *Nature Immunology*, vol. 14, pp. 82–89, 1 Jan. 2013, ISSN: 15292908. DOI: [10.1038/ni.2488](https://doi.org/10.1038/ni.2488).
- [7] C. Floderer, J. B. Masson, E. Boilley, *et al.*, “Single molecule localisation microscopy reveals how hiv-1 gag proteins sense membrane virus assembly sites in living host cd4 t cells,” *Scientific Reports*, vol. 8, 1 Dec. 2018, ISSN: 20452322. DOI: [10.1038/s41598-018-34536-y](https://doi.org/10.1038/s41598-018-34536-y).
- [8] Y. L. Wang, W. W. Zhao, J. Shi, X. B. Wan, J. Zheng, and X. J. Fan, *Liquid-liquid phase separation in dna double-strand breaks repair*, Jul. 2023. DOI: [10.1038/s41419-023-06267-0](https://doi.org/10.1038/s41419-023-06267-0).
- [9] M. A. Ricci, C. Manzo, M. F. García-Parajo, M. Lakadamyali, and M. P. Cosma, “Chromatin fibers are formed by heterogeneous groups of nucleosomes in vivo,” *Cell*, vol. 160, pp. 1145–1158, 6 Jul. 2015, ISSN: 10974172. DOI: [10.1016/j.cell.2015.01.054](https://doi.org/10.1016/j.cell.2015.01.054).
- [10] T. Nozaki, R. Imai, M. Tanbo, *et al.*, “Dynamic organization of chromatin domains revealed by super-resolution live-cell imaging,” *Molecular Cell*, vol. 67, 282–293.e7, 2 2017, ISSN: 10974164. DOI: [10.1016/j.molcel.2017.06.018](https://doi.org/10.1016/j.molcel.2017.06.018).

- [11] A. N. Boettiger, B. Bintu, J. R. Moffitt, *et al.*, “Super-resolution imaging reveals distinct chromatin folding for different epigenetic states,” *Nature*, vol. 529, pp. 418–422, 7586 Jan. 2016, ISSN: 14764687. DOI: [10.1038/nature16496](https://doi.org/10.1038/nature16496).
- [12] B. Zhang, J. Zerubia, and J.-C. Olivo-Marin, “Gaussian approximations of fluorescence microscope point-spread function models,” *Appl. Opt.*, vol. 46, pp. 1819–1829, 10 Apr. 2007. DOI: [10.1364/AO.46.001819](https://doi.org/10.1364/AO.46.001819). [Online]. Available: <https://opg.optica.org/ao/abstract.cfm?URI=ao-46-10-1819>.
- [13] Richards and Wolf, “Electromagnetic diffraction in optical systems,” *Proceedings of the Royal Society A*, vol. 253, pp. 1358–1379, 1959.
- [14] S. F. Gibson and F. Lanni, “Diffraction by a circular aperture as a model for three-dimensional optical microscopy,” *J. Opt. Soc. Am. A*, vol. 6, pp. 1357–1367, 1989.
- [15] F. Huang *et al.*, “Video-rate nanoscopy using scmos camera-specific single-molecule localization algorithms,” *Nature Methods*, vol. 10, pp. 653–658, 2013.
- [16] J. Chao *et al.*, “Fisher information theory for parameter estimation in single molecule microscopy: Tutorial,” *Journal of the Optical Society of America A*, 2016.
- [17] C. S. Smith, N. Joseph, B. Rieger, and K. A. Lidke, “Fast, single-molecule localization that achieves theoretically minimum uncertainty,” *Nature Methods*, vol. 7, pp. 373–375, 5 May 2010, ISSN: 15487091. DOI: [10.1038/nmeth.1449](https://doi.org/10.1038/nmeth.1449).
- [18] R. Nieuwenhuizen *et al.*, “Measuring image resolution in optical nanoscopy,” *Nature Methods*, vol. 10, pp. 557–562, 2013.
- [19] T. Dertinger, R. Colyer, G. Iyer, S. Weiss, and J. Enderlein, “Fast, background-free, 3d super-resolution optical fluctuation imaging (sofi),” *Proceedings of the National Academy of Sciences*, vol. 106, pp. 22 287–22 292, 52 2009. DOI: [10.1073/pnas.0907866106](https://doi.org/10.1073/pnas.0907866106). [Online]. Available: <https://www.pnas.org/doi/abs/10.1073/pnas.0907866106>.
- [20] D. Stoler, B. E. A. Saleh, and M. C. Teich, *Binomial states of the quantized radiation field*, 1985.
- [21] M. Rust *et al.*, “Sub-diffraction-limit imaging by stochastic optical reconstruction microscopy (storm),” *Nature Methods*, vol. 3, pp. 793–796, 2006.

- [22] E. Betzig *et al.*, “Imaging intracellular fluorescent proteins at nanometer resolution,” *Science*, vol. 313, pp. 1642–1645, 2006.
- [23] H. Ta, J. Wolfrum, and D.-P. Herten, “An extended scheme for counting fluorescent molecules by photon-antibunching,” *Laser Physics*, 2010, ISSN: 1054-660X. DOI: [10.1134/S1054660X09170204](https://doi.org/10.1134/S1054660X09170204).
- [24] Y. Israel *et al.*, “Quantum correlation enhanced super-resolution localization microscopy enabled by a fibre bundle camera,” *Nature Communications*, vol. 8, p. 14 786, 2017. DOI: [10.1038/ncomms14786](https://doi.org/10.1038/ncomms14786).
- [25] J. Goodman and J. Weare, “Ensemble samplers with affine invariance,” *Communications in Applied Mathematics and Computational Science*, vol. 5, pp. 65–80, 1 2010. DOI: [10.2140/camcos.2010.5.65](https://doi.org/10.2140/camcos.2010.5.65). [Online]. Available: <https://doi.org/10.2140/camcos.2010.5.65>.
- [26] D. Kingma *et al.*, “Auto encoding variational bayes,” 2013.
- [27] S. Geman and D. Geman, “Stochastic relaxation, gibbs distributions, and the bayesian restoration of images,” *IEEE Transactions on Pattern Analysis and Machine Intelligence*, vol. PAMI-6, pp. 721–741, 6 1984, ISSN: 01628828. DOI: [10.1109/TPAMI.1984.4767596](https://doi.org/10.1109/TPAMI.1984.4767596).
- [28] M. Weigert *et al.*, “Content-aware image restoration: Pushing the limits of fluorescence microscopy,” *Nature Methods*, vol. 15, p. 1090, 2018.
- [29] T. Falk *et al.*, “U-net: Deep learning for cell counting, detection, and morphometry,” *Nature Methods*, vol. 16, pp. 67–70, 2019.
- [30] W. Ouyang *et al.*, “Deep learning massively accelerates super-resolution localization microscopy,” *Nature Biotechnology*, vol. 36, pp. 460–468, 2018.
- [31] E. Nehme *et al.*, “Deepstorm3d: Dense 3d localization microscopy and psf design by deep learning,” *Nature Methods*, vol. 17, pp. 734–740, 2020.
- [32] A. Speiser *et al.*, “Deep learning enables fast and dense single-molecule localization with high accuracy,” *Nature Methods*, vol. 18, pp. 1082–1090, 2021.
- [33] Y. Song *et al.*, “Score-based generative model through stochastic differential equations,” 2021.

- [34] J. Ho *et al.*, “Denoising diffusion probabilistic models,” 2020.
- [35] B. Lakshminarayanan *et al.*, *Simple and scalable predictive uncertainty estimation using deep ensembles*, 2017.
- [36] Y. Gal *et al.*, “Bayesian uncertainty quantification for machine-learned models in physics,” *Nature Physics*, 2022.
- [37] S. Dirmeier *et al.*, “Diffusion models for probabilistic programming,” 2023.
- [38] F. Ribeiro *et al.*, “Demystifying variational diffusion models,” 2024.
- [39] D. Kingma *et al.*, “Variational diffusion models,” 2021.
- [40] D. Kingma *et al.*, “Understanding diffusion objectives as the elbo with simple data augmentation,” 2023.
- [41] P. Zhang *et al.*, “Analyzing complex single-molecule emission patterns with deep learning,” *Nature Methods*, vol. 15, p. 913, 2018.
- [42] T. H. Kim *et al.*, “Information-rich localization microscopy through machine learning,” *Nature Communications*, vol. 10, p. 1996, 2019.
- [43] P. Zelger *et al.*, “Three-dimensional localization microscopy using deep learning,” *Opt. Express*, vol. 26, pp. 33 166–33 179, 2018.
- [44] C. Saharia *et al.*, “Image super-resolution via iterative refinement,” 2021.
- [45] A. Vahdat *et al.*, “Score-based generative modeling in latent space,” 2021.
- [46] Y. Song *et al.*, “Generative modeling by estimating gradients of the data distribution,” 2019.
- [47] R. K. Auerbach, G. Euskirchen, J. Rozowsky, N. Lamarre-Vincent, Z. Moqtaderi, P. Lefrancois, *et al.*, “Mapping accessible chromatin regions using sono-seq,” *Proc Natl Acad Sci U S A*, vol. 106, pp. 14 926–14 931, 2009.
- [48] F. T. Chien and J. van Noort, “10 years of tension on chromatin: Results from single molecule force spectroscopy,” *Curr Pharm Biotechnol*, vol. 10, pp. 474–485, 2009.

- [49] C. R. Clapier and B. R. Cairns, “The biology of chromatin remodeling complexes,” *Annu Rev Biochem*, vol. 78, pp. 273–304, 2009.
- [50] T. Misteli, “Beyond the sequence: Cellular organization of genome function,” *Cell*, vol. 128, pp. 787–800, 2007.
- [51] P. A. Vidi, J. Liu, D. Salles, S. Jayaraman, G. Dorfman, M. Gray, *et al.*, “Numa promotes homologous recombination repair by regulating the accumulation of the iswi atpase snf2h at dna breaks,” *Nucleic Acids Research*, vol. 42, pp. 6365–6379, 2014.
- [52] O. Cuvier and B. Fierz, “Dynamic chromatin technologies: From individual molecules to epigenomic regulation in cells,” *Nature Reviews Genetics*, vol. 18, pp. 457–472, 2017.
- [53] V. Dion and S. M. Gasser, “Chromatin movement in the maintenance of genome stability,” *Cell*, vol. 152, pp. 1355–1364, 2013.
- [54] J. S. Choy and T. H. Lee, “Structural dynamics of nucleosomes at single-molecule resolution,” *Trends Biochem Sci*, vol. 37, pp. 425–435, 2012.
- [55] W. Li, P. Chen, J. Yu, L. Dong, D. Liang, J. Feng, *et al.*, “Fact remodels the tetranucleosomal unit of chromatin fibers for gene transcription,” *Mol Cell*, vol. 64, pp. 120–133, 2016.
- [56] B. Bintu, L. J. Mateo, J. H. Su, N. A. Sinnott-Armstrong, M. Parker, S. Kinrot, *et al.*, “Super-resolution chromatin tracing reveals domains and cooperative interactions in single cells,” *Science*, vol. 362, eaau1783, 2018.
- [57] M. J. Grant, M. S. Loftus, A. P. Stoja, D. H. Kedes, and M. M. Smith, “Superresolution microscopy reveals structural mechanisms driving the nanoarchitecture of a viral chromatin tether,” *Proceedings of the National Academy of Sciences of the United States of America*, vol. 115, pp. 4992–4997, 2018.
- [58] J. Xu, H. Ma, J. Jin, *et al.*, “Super-resolution imaging of higher-order chromatin structures at different epigenomic states in single mammalian cells,” *Cell Reports*, vol. 24, pp. 873–882, 4 Jul. 2018, ISSN: 22111247. DOI: [10.1016/j.celrep.2018.06.085](https://doi.org/10.1016/j.celrep.2018.06.085).
- [59] B. Fierz and M. G. Poirier, “Biophysics of chromatin dynamics,” *Annual Review of Biophysics*, vol. 48, pp. 321–345, 2019.

- [60] O. Shukron, A. Seeber, A. Amitai, and D. Holcman, *Advances using single-particle trajectories to reconstruct chromatin organization and dynamics*, 2019. DOI: [10.1016/j.tig.2019.06.007](https://doi.org/10.1016/j.tig.2019.06.007).
- [61] S. Conic, D. Desplancq, A. Ferrand, V. Fischer, V. Heyer, B. R. S. Martin, *et al.*, “Imaging of native transcription factors and histone phosphorylation at high resolution in live cells,” *Journal of Cell Biology*, vol. 217, pp. 1537–1552, 2018.
- [62] A. S. Belmont, “Visualizing chromosome dynamics with gfp,” *Trends Cell Biol*, vol. 11, pp. 250–257, 2001.
- [63] T. Das, B. Payer, M. Cayouette, and W. A. Harris, “In vivo time-lapse imaging of cell divisions during neurogenesis in the developing zebrafish retina,” *Neuron*, vol. 37, pp. 597–609, 2003.
- [64] T. Kanda, K. F. Sullivan, and G. M. Wahl, “Histone-gfp fusion protein enables sensitive analysis of chromosome dynamics in living mammalian cells,” *Curr Biol*, vol. 8, pp. 377–385, 1998.
- [65] I. I. Cisse, I. Izeddin, S. Z. Causse, L. Boudarene, A. Senecal, L. Muresan, *et al.*, “Real-time dynamics of rna polymerase ii clustering in live human cells,” *Science*, vol. 341, pp. 664–667, 2013.
- [66] S. Manley, J. M. Gillette, G. H. Patterson, H. Shroff, H. F. Hess, E. Betzig, *et al.*, “High-density mapping of single-molecule trajectories with photoactivated localization microscopy,” *Nat Methods*, vol. 5, pp. 155–157, 2008.
- [67] V. Liss, B. Barlag, M. Nietschke, and M. Hensel, “Self-labelling enzymes as universal tags for fluorescence microscopy, super-resolution microscopy and electron microscopy,” *Sci Rep*, vol. 5, p. 17740, 2015.
- [68] F. Stagge, G. Y. Mitronova, V. N. Belov, C. A. Wurm, and S. Jakobs, “Snap-, clip- and halo-tag labelling of budding yeast cells,” *PLoS One*, vol. 8, e78745, 2013.
- [69] J. B. Grimm, A. K. Muthusamy, Y. Liang, T. A. Brown, W. C. Lemon, R. Patel, *et al.*, “A general method to fine-tune fluorophores for live-cell and in vivo imaging,” *Nature Methods*, vol. 14, pp. 987–994, 2017.
- [70] R. Nagashima, K. Hibino, S. S. Ashwin, *et al.*, “Single nucleosome imaging reveals loose genome chromatin networks via active rna polymerase ii,” *Journal of Cell Biology*, vol. 218, pp. 1511–1530, 5 Jul. 2019, ISSN: 15408140. DOI: [10.1083/jcb.201811090](https://doi.org/10.1083/jcb.201811090).

- [71] L. Avogaro, E. Querido, M. Dalachi, M. F. Jantsch, P. Chartrand, and E. Cusanelli, “Live-cell imaging reveals the dynamics and function of single-telomere terra molecules in cancer cells,” *RNA Biol*, vol. 15, pp. 787–796, 2018.
- [72] S. M. Gasser, “Visualizing chromatin dynamics in interphase nuclei,” *Science*, vol. 296, pp. 1412–1416, 2002.
- [73] W. Wang, G. W. Li, C. Chen, X. S. Xie, and X. Zhuang, “Chromosome organization by a nucleoid-associated protein in live bacteria,” *Science*, vol. 333, pp. 1445–1449, 2011.
- [74] Y. S. Hu, Q. Zhu, K. Elkins, K. Tse, Y. Li, J. A. Fitzpatrick, *et al.*, “Light-sheet bayesian microscopy enables deep-cell super-resolution imaging of heterochromatin in live human embryonic stem cells,” *Opt Nanoscopy*, vol. 2, 2013.
- [75] J. Elf, G. W. Li, and X. S. Xie, “Probing transcription factor dynamics at the single-molecule level in a living cell,” *Science*, vol. 316, pp. 1191–1194, 2007.
- [76] J. C. Gebhardt, D. M. Suter, R. Roy, Z. W. Zhao, A. R. Chapman, S. Basu, *et al.*, “Single-molecule imaging of transcription factor binding to dna in live mammalian cells,” *Nature Methods*, vol. 10, pp. 421–426, 2013.
- [77] J. Bayani and J. A. Squire, “Fluorescence in situ hybridization (fish),” *Curr Protoc Cell Biol*, vol. Chapter 22, Unit 22 4, 2004.
- [78] B. J. Beliveau, A. N. Boettiger, M. S. Avendaño, *et al.*, “Single-molecule super-resolution imaging of chromosomes and in situ haplotype visualization using oligopaint fish probes,” *Nature Communications*, vol. 6, May 2015, ISSN: 20411723. DOI: [10.1038/ncomms8147](https://doi.org/10.1038/ncomms8147).
- [79] D. Q. Ding and Y. Hiraoka, “Visualization of a specific genome locus by the laco/laci-gfp system,” *Cold Spring Harbor Protocols*, vol. 2017, pdb prot091934, 2017.
- [80] I. Loiodice, M. Dubarry, and A. Taddei, “Scoring and manipulating gene position and dynamics using fros in budding yeast,” *Curr Protoc Cell Biol*, vol. 62, Unit 22 17 1–4, 2014.
- [81] M. P. Backlund, R. Joyner, K. Weis, and W. E. Moerner, “Correlations of three-dimensional motion of chromosomal loci in yeast revealed by the double-helix point spread function microscope,” *Mol Biol Cell*, vol. 25, pp. 3619–3629, 2014.

- [82] V. Roukos, T. C. Voss, C. K. Schmidt, S. Lee, D. Wangsa, and T. Misteli, “Spatial dynamics of chromosome translocations in living cells,” *Science*, vol. 341, pp. 660–664, 2013.
- [83] I. Tasan, G. Sustackova, L. Zhang, J. Kim, M. Sivaguru, M. HamediRad, *et al.*, “Crispr/cas9-mediated knock-in of an optimized teto repeat for live cell imaging of endogenous loci,” *Nucleic Acids Res*, vol. 46, e100, 2018.
- [84] R. Jungmann, M. S. Avendano, M. Dai, J. B. Woehrstein, S. S. Agasti, Z. Feiger, *et al.*, “Quantitative super-resolution imaging with qpaint,” *Nat Methods*, vol. 13, pp. 439–442, 2016.
- [85] B. Chen, J. Guan, and B. Huang, “Imaging specific genomic dna in living cells,” *Annu Rev Biophys*, vol. 45, pp. 1–23, 2016.
- [86] B. I. Lindhout, P. Fransz, F. Tessadori, T. Meckel, P. J. Hooykaas, and B. J. van der Zaal, “Live cell imaging of repetitive dna sequences via gfp-tagged polydactyl zinc finger proteins,” *Nucleic Acids Res*, vol. 35, e107, 2007.
- [87] H. Ma, P. Reyes-Gutierrez, and T. Pederson, “Visualization of repetitive dna sequences in human chromosomes with transcription activator-like effectors,” *Proc Natl Acad Sci U S A*, vol. 110, pp. 21 048–21 053, 2013.
- [88] B. Chen, L. A. Gilbert, B. A. Cimini, J. Schnitzbauer, W. Zhang, G. W. Li, *et al.*, “Dynamic imaging of genomic loci in living human cells by an optimized crispr/cas system,” *Cell*, vol. 155, pp. 1479–1491, 2013.
- [89] H. Ma, A. Naseri, P. Reyes-Gutierrez, S. A. Wolfe, S. Zhang, and T. Pederson, “Multicolor crispr labeling of chromosomal loci in human cells,” *Proc Natl Acad Sci U S A*, vol. 112, pp. 3002–3007, 2015.
- [90] J. G. Zalatan, M. E. Lee, R. Almeida, L. A. Gilbert, E. H. Whitehead, M. L. Russa, *et al.*, “Engineering complex synthetic transcriptional programs with crispr rna scaffolds,” *Cell*, vol. 160, pp. 339–350, 2015.
- [91] D. M. Shechner, E. Hacisuleyman, S. T. Younger, and J. L. Rinn, “Multiplexable, locus-specific targeting of long rnas with crispr-display,” *Nat Methods*, vol. 12, pp. 664–670, 2015.

- [92] H. Ma, L. C. Tu, A. Naseri, M. Huisman, S. Zhang, D. Grunwald, *et al.*, “Multiplexed labeling of genomic loci with dCas9 and engineered sgRNAs using crisprainbow,” *Nat Biotechnol*, vol. 34, pp. 528–530, 2016.
- [93] S. Burov, S. M. Tabei, T. Huynh, M. P. Murrell, L. H. Philipson, S. A. Rice, *et al.*, “Distribution of directional change as a signature of complex dynamics,” *Proc Natl Acad Sci U S A*, vol. 110, pp. 19689–19694, 2013.
- [94] D. F. Albeanu, E. Soucy, T. F. Sato, M. Meister, and V. N. Murthy, “Led arrays as cost effective and efficient light sources for widefield microscopy,” *PLoS One*, vol. 3, e2146, 2008.
- [95] A. Hattori, S. Habuchi, and M. Vacha, “Single-molecule imaging with an inexpensive uv-led light source,” *Chemistry Letters*, vol. 38, pp. 234–235, 2009.
- [96] J. Zheng and K. Qian, “Designing single led illumination distribution for direct-type backlight,” *Appl Opt*, vol. 52, pp. 7022–7027, 2013.
- [97] P. J. Keller, M. B. Ahrens, and J. Freeman, “Light-sheet imaging for systems neuroscience,” *Nature methods*, vol. 12, pp. 27–29, 2015.
- [98] P. J. Keller, A. D. Schmidt, A. Santella, K. Khairy, Z. Bao, J. Wittbrodt, *et al.*, “Fast, high-contrast imaging of animal development with scanned light sheet-based structured-illumination microscopy,” *Nature methods*, vol. 7, pp. 637–642, 2010.
- [99] P. J. Keller, A. D. Schmidt, J. Wittbrodt, and E. H. Stelzer, “Reconstruction of zebrafish early embryonic development by scanned light sheet microscopy,” *Science*, vol. 322, pp. 1065–1069, 2008.
- [100] R. Tomer, K. Khairy, and P. J. Keller, “Shedding light on the system: Studying embryonic development with light sheet microscopy,” *Curr Opin Genet Dev*, vol. 21, pp. 558–565, 2011.
- [101] M. Tokunaga, N. Imamoto, and K. Sakata-Sogawa, “Highly inclined thin illumination enables clear single-molecule imaging in cells,” *Nat Methods*, vol. 5, pp. 159–161, 2008.
- [102] R. Galland, G. Grenci, A. Aravind, V. Viasnoff, V. Studer, and J. B. Sibarita, “3d high- and super-resolution imaging using single-objective spim,” *Nature Methods*, vol. 12, pp. 641–644, 2015.

- [103] B. C. Chen, W. R. Legant, K. Wang, L. Shao, D. E. Milkie, M. W. Davidson, *et al.*, “Lattice lightsheet microscopy: Imaging molecules to embryos at high spatiotemporal resolution,” *Science*, vol. 346, p. 1257998, 2014.
- [104] R. Gao, S. M. Asano, S. Upadhyayula, I. Pisarev, D. E. Milkie, T. L. Liu, *et al.*, “Cortical column and whole-brain imaging with molecular contrast and nanoscale resolution,” *Science*, vol. 363, 2019.
- [105] E. H. Finn, G. Pegoraro, S. Shachar, and T. Misteli, “Comparative analysis of 2d and 3d distance measurements to study spatial genome organization,” *Methods*, vol. 123, pp. 47–55, 2017.
- [106] B. Huang, W. Wang, M. Bates, and X. Zhuang, “Three-dimensional super-resolution imaging by stochastic optical reconstruction microscopy,” *Science*, vol. 319, pp. 810–813, 5864 Feb. 2008, ISSN: 00368075. DOI: [10.1126/science.1153529](https://doi.org/10.1126/science.1153529).
- [107] A. Greengard, Y. Y. Schechner, and R. Piestun, “Depth from diffracted rotation,” *Optics Letters*, vol. 31, pp. 181–183, 2006.
- [108] S. R. Pavani, M. A. Thompson, J. S. Biteen, S. J. Lord, N. Liu, R. J. Twieg, *et al.*, “Three-dimensional, single-molecule fluorescence imaging beyond the diffraction limit by using a double-helix point spread function,” *Proc Natl Acad Sci U S A*, vol. 106, pp. 2995–2999, 2009.
- [109] M. Badieirostami, M. D. Lew, M. A. Thompson, and W. E. Moerner, “Three-dimensional localization precision of the double-helix point spread function versus astigmatism and biplane,” *Appl Phys Lett*, vol. 97, p. 161103, 2010.
- [110] M. A. Thompson, M. D. Lew, M. Badieirostami, and W. E. Moerner, “Localizing and tracking single nanoscale emitters in three dimensions with high spatiotemporal resolution using a double-helix point spread function,” *Nano Lett*, vol. 10, pp. 211–218, 2010.
- [111] N. Hoze, D. Nair, E. Hosy, C. Sieben, S. Manley, A. Herrmann, *et al.*, “Heterogeneity of ampa receptor trafficking and molecular interactions revealed by superresolution analysis of live cell imaging,” *Proc Natl Acad Sci U S A*, vol. 109, pp. 17052–17057, 2012.
- [112] D. Holcman, N. Hoze, and Z. Schuss, “Analysis and interpretation of superresolution single-particle trajectories,” *Biophys J*, vol. 109, pp. 1761–1771, 2015.

- [113] N. Hoze and D. Holcman, “Recovering a stochastic process from super-resolution noisy ensembles of single-particle trajectories,” *Phys Rev E Stat Nonlin Soft Matter Phys*, vol. 92, p. 52 109, 2015.
- [114] K. Maeshima, S. Tamura, J. C. Hansen, and Y. Itoh, *Fluid-like chromatin: Toward understanding the real chromatin organization present in the cell*, Jun. 2020. doi: [10.1016/j.ceb.2020.02.016](https://doi.org/10.1016/j.ceb.2020.02.016).
- [115] A. Amitai, A. Seeber, S. M. Gasser, and D. Holcman, “Visualization of chromatin decompaction and break site extrusion as predicted by statistical polymer modeling of single-locus trajectories,” *Cell Rep*, vol. 18, pp. 1200–1214, 2017.
- [116] L. Wasim and B. Treanor, “Single-particle tracking of cell surface proteins,” *Methods Mol Biol*, vol. 1707, pp. 183–192, 2018.
- [117] Y. Zhong and G. Wang, “Three-dimensional single particle tracking and its applications in confined environments,” *Annu Rev Anal Chem (Palo Alto Calif)*, vol. 13, pp. 381–403, 2020.
- [118] R. Barth, K. Bystricky, and H. A. Shaban, *Coupling chromatin structure and dynamics by live super-resolution imaging*, 2020. [Online]. Available: <https://www.science.org>.
- [119] J. C. Crocker and D. G. Grier, *Methods of digital video microscopy for colloidal studies*, 1996.
- [120] I. F. Sbalzarini and P. Koumoutsakos, “Feature point tracking and trajectory analysis for video imaging in cell biology,” *J Struct Biol*, vol. 151, pp. 182–195, 2005.
- [121] A. Amitai and D. Holcman, “Polymer model with long-range interactions: Analysis and applications to the chromatin structure,” *Phys Rev E Stat Nonlin Soft Matter Phys*, vol. 88, p. 52 604, 2013.
- [122] H. Hajjoul, J. Mathon, H. Ranchon, I. Goiffon, J. Mozziconacci, B. Albert, *et al.*, “High-throughput chromatin motion tracking in living yeast reveals the flexibility of the fiber throughout the genome,” *Genome Res*, vol. 23, pp. 1829–1838, 2013.
- [123] A. S. Hansen, I. Pustova, C. Cattoglio, R. Tjian, and X. Darzacq, “Ctcf and cohesin regulate chromatin loop stability with distinct dynamics,” *eLife*, vol. 6, 2017, ISSN: 2050084X. doi: [10.7554/eLife.25776.001](https://doi.org/10.7554/eLife.25776.001).

- [124] B. R. Sabari, A. DallAgnese, A. Boija, *et al.*, “Coactivator condensation at super-enhancers links phase separation and gene control,” *Science*, vol. 361, 6400 Jul. 2018, ISSN: 0036-8075. DOI: [10.1126/science.aar3958](https://doi.org/10.1126/science.aar3958).
- [125] D. Hnisz, K. Shrinivas, R. A. Young, A. K. Chakraborty, and P. A. Sharp, *A phase separation model for transcriptional control*, 2017. DOI: [10.1016/j.cell.2017.02.007](https://doi.org/10.1016/j.cell.2017.02.007).
- [126] J. M. Brown, J. Green, R. P. D. Neves, *et al.*, “Association between active genes occurs at nuclear speckles and is modulated by chromatin environment,” *Journal of Cell Biology*, vol. 182, pp. 1083–1097, 6 Jul. 2008, ISSN: 00219525. DOI: [10.1083/jcb.200803174](https://doi.org/10.1083/jcb.200803174).
- [127] K. Wagh, M. Ishikawa, D. A. Garcia, D. A. Stavreva, A. Upadhyaya, and G. L. Hager, *Mechanical regulation of transcription: Recent advances*, Jul. 2021. DOI: [10.1016/j.tcb.2021.02.008](https://doi.org/10.1016/j.tcb.2021.02.008).
- [128] A. J. Plys and R. E. Kingston, *Dynamic condensates activate transcription*, Jul. 2018. DOI: [10.1126/science.aau4795](https://doi.org/10.1126/science.aau4795).
- [129] A. R. Strom, J. M. Eeftens, Y. Polyachenko, *et al.*, “Interplay of condensation and chromatin binding underlies brd4 targeting,” *Molecular Biology of the Cell*, vol. 35, 6 Jul. 2024, ISSN: 19394586. DOI: [10.1091/mbe.E24-01-0046](https://doi.org/10.1091/mbe.E24-01-0046).
- [130] L. Ma, Z. Gao, J. Wu, *et al.*, “Co-condensation between transcription factor and coactivator p300 modulates transcriptional bursting kinetics,” *Molecular Cell*, vol. 81, 1682–1697.e7, 8 Jul. 2021, ISSN: 10974164. DOI: [10.1016/j.molcel.2021.01.031](https://doi.org/10.1016/j.molcel.2021.01.031).
- [131] T. Wu, Y. F. Kamikawa, and M. E. Donohoe, “Brd4s bromodomains mediate histone h3 acetylation and chromatin remodeling in pluripotent cells through p300 and brg1,” *Cell Reports*, vol. 25, pp. 1756–1771, 7 Jul. 2018, ISSN: 22111247. DOI: [10.1016/j.celrep.2018.10.003](https://doi.org/10.1016/j.celrep.2018.10.003).
- [132] F. Itzen, A. K. Greifenberg, C. A. Bösken, and M. Geyer, “Brd4 activates p-tefb for rna polymerase ii ctd phosphorylation,” *Nucleic Acids Research*, vol. 42, pp. 7577–7590, 12 Jul. 2014, ISSN: 13624962. DOI: [10.1093/nar/gku449](https://doi.org/10.1093/nar/gku449).
- [133] X. Han, D. Yu, R. Gu, *et al.*, “Roles of the brd4 short isoform in phase separation and active gene transcription,” *Nature Structural and Molecular Biology*, vol. 27, pp. 333–341, 4 Jul. 2020, ISSN: 15459985. DOI: [10.1038/s41594-020-0394-8](https://doi.org/10.1038/s41594-020-0394-8).

- [134] P. Filippakopoulos, J. Qi, S. Picaud, *et al.*, “Selective inhibition of bet bromodomains,” *Nature*, vol. 468, pp. 1067–1073, 7327 Jul. 2010, ISSN: 00280836. DOI: [10.1038/nature09504](https://doi.org/10.1038/nature09504).
- [135] S. Y. Wu, A. Y. Lee, H. T. Lai, H. Zhang, and C. M. Chiang, “Phospho switch triggers brd4 chromatin binding and activator recruitment for gene-specific targeting,” *Molecular Cell*, vol. 49, pp. 843–857, 5 Jul. 2013, ISSN: 10972765. DOI: [10.1016/j.molcel.2012.12.006](https://doi.org/10.1016/j.molcel.2012.12.006).
- [136] F. Malvezzi, C. J. Stubbs, T. A. Jowitt, *et al.*, “Phosphorylation-dependent brd4 dimerization and implications for therapeutic inhibition of bet family proteins,” *Communications Biology*, vol. 4, 1 Jul. 2021, ISSN: 23993642. DOI: [10.1038/s42003-021-02750-6](https://doi.org/10.1038/s42003-021-02750-6).
- [137] G. V. Los, L. P. Encell, M. G. McDougall, *et al.*, “Halotag: A novel protein labeling technology for cell imaging and protein analysis,” *ACS Chemical Biology*, vol. 3, pp. 373–382, 6 Jul. 2008, ISSN: 15548929. DOI: [10.1021/cb800025k](https://doi.org/10.1021/cb800025k).
- [138] J. B. Grimm, B. P. English, J. Chen, *et al.*, “A general method to improve fluorophores for live-cell and single-molecule microscopy,” *Nature Methods*, vol. 12, pp. 244–250, 3 2015, ISSN: 15487105. DOI: [10.1038/nmeth.3256](https://doi.org/10.1038/nmeth.3256).